Nano-Engineering Metamaterials and Metafilms

for High-Efficiency Solar Energy Harvesting and Conversion

by

Hao Wang

A Dissertation Presented in Partial Fulfillment
of the Requirements for the Degree
Doctor of Philosophy

Approved April 2016 by the
Graduate Supervisory Committee:

Liping Wang, Chair
Patrick Phelan
Robert Wang
Lenore Dai
Konrad Rykaczewski

ARIZONA STATE UNIVERSITY

May 2016

ABSTRACT

The energy crisis in the past decades has greatly boosted the search for alternatives to traditional fossil foils, and solar energy stands out as an important candidate due to its cleanness and abundance. However, the relatively low conversion efficiency and energy density strongly hinder the utilization of solar energy in wider applications. This thesis focuses on employing metamaterials and metafilms to enhance the conversion efficiency of solar thermal, solar thermophotovoltaic (STPV) and photovoltaic systems.

A selective metamaterial solar absorber is designed in this thesis to maximize the absorbed solar energy and minimize heat dissipation through thermal radiation. The theoretically designed metamaterial solar absorber exhibits absorptance higher than 95% in the solar spectrum but shows emittance less than 4% in the IR regime. This metamaterial solar absorber is further experimentally fabricated and optically characterized. Moreover, a metafilm selective absorber with stability up to 600^{o}C is introduced, which exhibits solar absorptance higher than 90% and IR emittance less than 10%.

Solar thermophotovoltaic energy conversion enhanced by metamaterial absorbers and emitters is theoretically investigated in this thesis. The STPV system employing selective metamaterial absorber and emitter is investigated in this work, showing its conversion efficiency between 8% and 10% with concentration factor varying between 20 and 200. This conversion efficiency is remarkably enhanced compared with the conversion efficiency for STPV system employing black surfaces (<2.5%).

Moreover, plasmonic light trapping in ultra-thin solar cells employing concave grating nanostructures is discussed in this thesis. The plasmonic light trapping inside an ultrathin GaAs layer in the film-coupled metamaterial structure is numerically demonstrated. By exciting plasmonic resonances inside this structure, the short-circuit current density for the film-coupled metamaterial solar cell is three times the short-circuit current for a free-standing GaAs layer.

The dissertation is concluded by discussing about the future work on selective solar thermal absorbers, STPV/TPV systems and light trapping structures. Possibilities to design and fabricate solar thermal absorber with better thermal stability will be discussed, the experimental work of TPV system will be conducted, and the light trapping in organic and perovskite solar cells will be looked into.

Dedicated to

my father Xiao’an Wang, my mother Xiaoyuan Guan

and my grandfather Wuliang Wang

ACKNOWLEDGMENTS

First and foremost, I am more than grateful to my Ph.D. advisor, Dr. Liping Wang, for giving me this opportunity to work in his research group. I have learned a lot from his mentorship in both academic and personality aspects, which would benefit me tremendously for the rest of my life. I would like to show my gratitude to Dr. Patrick Phelan, Dr. Robert Wang, Dr. Lenore Dai and Dr. Konrad Rykaczewski, who devoted their valuable time to serve as my committee member and provided me with valuable advice. I would also like to acknowledge the National Science Foundation and the Australian Renewable Energy Agency which supported our research work.

I would like to express my appreciation for all the collaborators in my research projects. I would like to thank Dr. Arnan Mitchell's group, who collaborated with us in the metamaterial solar absorber project. I cherish my experience together with Yue, who is a professional collaborator as well as a great friend. I would like to express my thankfulness to Jui-Yung, whose diligence inspired me constantly. I learned a lot from Sydney, whose creativity is something truly special. I also value the interactions with Hassan, Payam, Hang, XiaoYan, and Yanchao in this group. I am very grateful to the staff in CSSER: Todd, Clarence, Carrie, Kevin and Arthur, for their patient and kind help.

Last but not least, I cannot say how much I am indebted to my parents for their love and support to their little kid. I would like to present this work to my grandfather, who has been looking forward to my graduation but was not able to make it.

TABLE OF CONTENTS

Page

CHAPTER Page

LIST OF TABLES

Table Page

LIST OF FIGURES

Figure Page

Figure Page

Figure Page

Figure Page

Figure Page

CHAPTER 1

INTRODUCTION AND BACKGROUND

The energy crisis in the past decades has immensely boosted the search of alternatives to traditional fossil foils, among which solar energy stands out as an important candidate due to its cleanness and abundance. However, the relatively low conversion efficiency and energy density strongly hinder the utilization of solar energy in wider applications. Three solar energy harvesting techniques will be discussed in this thesis: solar thermal, solar TPV and solar PV systems. Figure 1.1 shows the schematics for these three solar energy conversion systems. Solar thermal systems convert solar radiation into thermal energy via a solar absorber, and then generate electricity through a heat engine. Solar PV systems directly convert solar radiation into electricity by solar cells. On the other hand, solar TPV systems employ an absorber/emitter module to absorb broadband solar radiation, and convert it into narrow band thermal emission towards the TPV cell to generate electricity.

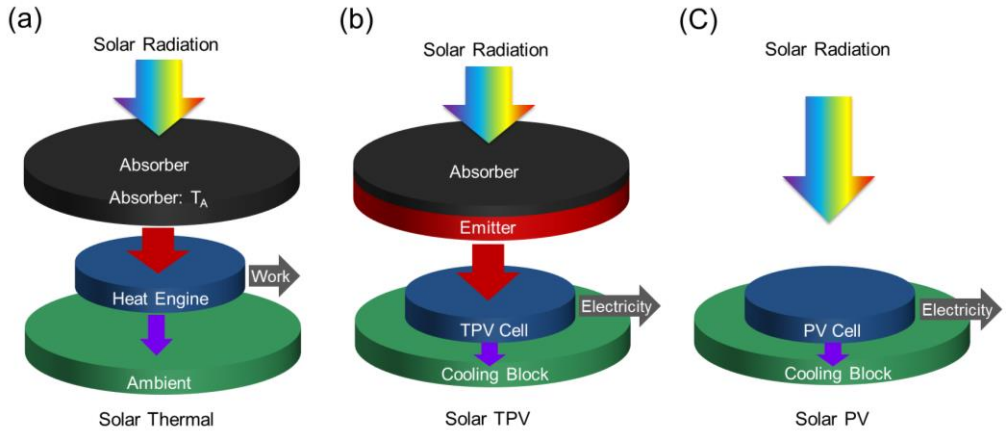

Figure 1.1 The schematics for (a) Solar thermal system; (b) Solar TPV system and (c) Solar PV system.

1.1 State-of-the-art Nanostructured Selective Absorbers

The solar absorber which converts solar radiation into thermal energy strongly affects the efficiency of solar energy collection and conversion in solar thermal, solar thermoelectric and solar thermophotovoltaic systems. Spectral selectivity is crucial for an effective solar absorber, which is highly desired to be strongly absorbing in the visible and near infrared (NIR) range and weakly emitting in the infrared (IR) spectral regime. In this way the collected solar energy can be maximized while the thermal emission loss from the absorber will be minimized. In addition, a consistent performance at elevated temperatures is also highly preferred for concentrating solar power (CSP) systems with a high energy density but strict requirements on the absorber's thermal stability.

Different approaches have been investigated to obtain selective absorbers, including both material and structure based approaches [1]. Material based selective absorbers consist of natural or treated materials such as black paint, black chrome [2-4], Pyromark [5] as well as composites and cermet [6-10], which exhibit intrinsic selective optical properties. However, the spectral selectivity for material based selective absorbers is usually not ideal, which either exhibit a high emittance in the IR or a slow transition between highly absorbing and weakly emitting. Meanwhile, the tunability of optical properties for the material based selective absorbers is low, making it harder to modify the optical properties to meet the requirements of different applications.

Apart from material based absorbers, spectral selectivity can be achieved in artificial materials or metamaterials constructed by nano-structures whose exotic properties cannot be found in natural occurring materials [11]. Selective absorption peaks can be attained in metamaterials by the excitation of plasmonic resonance at particular

wavelengths, which can be tuned by changing the geometric parameters of the nano-structures. Meanwhile, the cutoff between high absorptance and low emittance is usually sharp in metamaterials, as they usually contain metallic components which lead to highly reflective behavior beyond resonance. Various selective metamaterial selective absorbers have been proposed, based on gratings [12-15], nanoparticles [16-18], photonic crystals [19-21], as well as cross-bar and nano-disk arrays [22, 23]. Perfect metamaterial absorbers made of electric ring resonators coupled to metal wires were proposed by Landy et al. [24], which exhibited selective absorption in the terahertz region. By replacing the metal wires with a continuous film, Tao et al. [25] improved the design to achieve wide-angle absorption for both transverse electric (TE) and magnetic (TM) polarized waves. Different pattern designs such as chiral metamaterial [26], fishnet structure [27], and cut-wire array [28] were proposed to achieve omnidirectional and polarization-independent absorption in the THz regime.

By shrinking the sizes of the metamaterial absorbers, the near-perfect selective absorption can be obtained in the infrared and visible region for selective solar thermal absorbers. Liu et al. [29] experimentally demonstrated an absorption of 97% at the wavelength of 6 μm in a subwavelength perfect absorber made of a film-coupled crossbar structure. A plasmonic absorber made of a layer of gold patch array with the width less than 200 nm on a thin Al_2O_3 layer and a gold film showed an absorption peak of 88% at the wavelength of 1.58 μm [30]. By depositing a two dimensional (2D) Ag grating with a period of 300 nm on a 60-nm SiO_2 and a Ag film, Aydin et al. [31] demonstrated an ultra-thin plasmonic absorber in the visible spectrum. Strong visible light absorption has also been achieved by film-coupled colloidal nanoantennas [32], circular plasmonic resonators

[22], and nanoparticles [16, 33, 34], by exciting magnetic resonance inside the metamaterial absorbers. It is worth noting that, selective absorption can also be used for controlling thermal emission, indicated by Kirchhoff's law [35], and selective thermal emitters made of film-coupled micro/nanostructures [13, 36-39] have been studied. These structures with 2D symmetric patterns are proved to exhibit strong wavelength selectivity, angular independence, and polarization-independent behaviors.

Since the absorption behaviors such as the resonance wavelengths in the plasmonic metamaterial absorbers strongly depend on the shape and geometric sizes of the nanostructure patterns [40, 41], dual-, multi-, and broad-band absorption can be obtained by employing the multisize effect. Cui et al. [42] experimentally demonstrated a broadband absorber made of 1D metal strips with four different widths. Four resonances are excited at nearby wavelengths in the infrared such that the resonance peaks are coupled to form a broader absorption band from 9 μm to 11 μm. Wu and Shvets [43] theoretically showed a similar design with three different metallic strip widths to achieve broadband absorption in the near-infrared region. Based on the same concept, 2D film-coupled multi-sized disk arrays [44] and multi-sized patch arrays [45] were also shown as broadband plasmonic absorbers with polarization independence by exciting multiple resonances in the infrared. Dual- and broad-band absorption can also be achieved with asymmetric [23], double [46], or multi-sized cross-bar structures [36]. Moreover, by designing stacked metal-dielectric structures, plasmonic resonances can be excited inside distinct dielectric spacers at different wavelengths to achieve dual- [47] or multi-band [48] absorption, and an ultra-broadband light absorption can be achieved in the infrared region by combining the multisize and multilayer effect [49].

However, metamaterial structures usually require complicated fabrication techniques with low productivity, making them harder to fabricate in large scale. In addition, the high temperature stability for metamaterial solar absorbers could be a concern, as it will be harder to maintain the surface topography for the nano-structures due to thermal stress caused by the high temperature. Multilayer structures [50, 51] exploiting the anti-reflection effect or cavity resonance have been proposed as another approach to obtain selective solar absorbers. However, due to the possible instability induced by thermal stress, the high temperature stability needs to be further examined for the multilayer absorbers, as well as the temperature dependent optical properties.

1.2 State-of-the-art Solar Thermophotovoltaic Systems

Energy conversion by single-junction solar cells is constrained by the Shockley-Queisser limit [52], which strongly limits the utilization of clean and abundant solar energy. Two of the main factors leading to this limitation are: photons with energy below the bandgap of solar cells cannot generate electron-hole pairs; photons with energy higher than the bandgap can at most generate one electron-hole pair in single exciton cases, which results in the waste of excess energy above the bandgap. On the other hand, by converting broadband solar radiation into narrowband thermal emission with an intermediate absorber-emitter module, solar thermophotovoltaic (STPV) systems can potentially reach a much higher efficiency by better matching the emitted energy to the bandgap of TPV cells [53, 54]. In spite of the potentially high conversion efficiency, actual STPV devices exhibit much lower efficiency due to the non-idealities in absorber-emitter module and TPV cells.

STPV systems have been studied both theoretically and experimentally, seeking for approaches to enhance the conversion efficiency. By modifying the radiative properties of the absorber-emitter module, energy conversion of STPV systems can be remarkably enhanced with a better match between thermal radiation from the emitter and the bandgap of TPV cells. Nam et al. theoretically predicted a conversion efficiency up to 10% for STPV device with tantalum (Ta) photonic crystal as absorber and emitter [55], while Lenert et al. experimentally demonstrated an efficiency of 3.2% for STPV system with carbon nanotube as absorber and 1D photonic crystal as emitter [56]. The experimental conversion efficiency is further increased to 3.74% for STPV system with 2D Ta photonic crystal as absorber and emitter [57], while a STPV device with Ta photonic crystal as absorber and emitter whose efficiency exceeds 10% is recently reported [57].

Spectral selectivity is a key feature required for STPV absorber and emitter. Besides photonic crystals [19, 58-60], selective absorption/emission for the absorber-emitter module can also be obtained with multilayer cavities [61-64], nanowire [65-67] and nanoparticle based structures [17, 18]. Recently, film-coupled metamaterials with selective radiative properties have been investigated. These metamaterials are usually in metal-dielectric-metal configurations, with different nanostructures on the top including 1D [13, 38] and 2D convex gratings [12, 39], concave gratings [15, 68], trapezoid gratings [31], pyramid [69], disk [44, 70] and crossbar arrays [23, 46]. Through the excitation of plasmonic resonances such as surface plasmon polariton (SPP) [71-73] and magnetic polariton (MP) [13, 42, 45, 74], spectrally selective radiative properties can be obtained in these metamaterials. Note that, the radiative properties can easily be modified

by tuning the geometric parameters of the film-coupled structures, making it feasible to adjust the cutoff wavelengths of the absorber and emitter to fit with the applications in different STPV systems.

1.3 Plasmonic Light trapping in Ultrathin Solar Cells

Conventional solar cells are usually hundreds of microns in thickness due to the small absorption coefficient of semiconductor materials. Great efforts have been devoted to the investigation of thin-film solar cells with thickness of a few microns to reduce the cost for solar cells. However, effective light trapping is usually required to enhance light absorption in thin-film solar cells to achieve comparable or even better performance than conventional solar cells. Antireflection coatings [35, 75] can enhance light absorption in solar cells at particular wavelengths due to the destructive interference between incident and reflected light. Surface texturing [76-78] is another approach to increase light absorption with multiple reflection inside the textured structure. Moreover, by introducing a back reflector [79], light absorption could also be enhanced by increasing the optical path length of light but subjected to the $4n^2$ limit [80].

Plasmonic light trapping can achieve significant absorption enhancement in micro/nanostructured thin-film solar cells [80-82]. One dimensional (1D) back [83] and top [84, 85] metallic gratings have been utilized to enhance the light absorption by exciting surface waves. To overcome the limitation of the polarization state with 1D gratings, 2D patch arrays have also been proposed for enhancing light trapping with polarization and directional independences [86]. Broadband absorption enhancement has been studied in grating structures with a plasmonic fractal [87]. Besides, plasmonic

cavities in subwavelength hole arrays were also introduced for effective light trapping with 175% enhancement on power conversion efficiency [88]. In addition, scattering effect [89-92] and localized surface plasmon resonance [93, 94] with nanoparticles were other plasmonic light trapping approaches. However, it is still a daunting challenge to effectively trap lights in ultrathin solar cells with thickness below 100 nm for enhanced light absorption and thereby solar-to-electricity conversion efficiency.

1.4 Challenges in Solar Thermal, Solar TPV, and Light Trappig Systems

Although selective absorption in metamaterials has been intensively investigated, there are several challenges for metamaterial solar absorbers. Ideal solar absorbers need to exhibit a broad absorption band covering from UV to near IR spectral regime, which is hard for metamaterials which obtains selective absorption by exciting plasmonic resonances that usually leads to sharp and narrow absorption peaks. On the other hand, solid performance at various incidence angles, polarization states and high absorber temperatures is also highly preferred for solar thermal absorbers, which has not been much demonstrated.

By converting broadband solar radiation into narrowband thermal emission with an intermediate absorber-emitter module, solar thermophotovoltaic (STPV) systems can potentially reach a much higher efficiency of 85%. In spite of the potentially high conversion efficiency, actual STPV devices exhibit much lower efficiency due to the non-idealities in the system, such as absorber and emitter which is not ideally selective, non-unity view factor between TPV emitter and cell and charge recombination in TPV cells.

Thin-film solar cells have been investigated intensively in the past few years, for which light trapping becomes crucial to enhance the absorption of solar irradiation. However, current thin-film solar cells are still in micron or sub-micron scale in thickness. Next-generation solar cells with much thinner active layers are in urgent needs. New physical mechanism of light trapping is needed to enable high-efficiency and low cost ultra-thin solar cells. Other issues such as difficulties in fabricating the electric contacts on the nano-structured surface also exist.

CHAPTER 2

INSTRUMENTATION FOR OPTICAL AND RADIATIVE PROPERTIES CHARACTERIZATION

This chapter introduces the metrology equipment to characterize the optical and radiative properties of metamaterials/metafilms. Section 2.1 presents the FTIR spectrometer which can be employed to measure the specular reflectance of samples from visible to mid-IR range. A variable incidence angle reflectance accessory is coupled with the FTIR spectrometer to measure the reflectance at incidence angles from 5^o to 85^o. Section 2.2 describes a tunable light source integrated with an integrating sphere to measure both the hemispherical and diffuse reflectance of samples. Section 2.3 introduces an in-situ FTIR fiber optics setup that can measure the temperature dependent reflectance of sample up to 800^oC. Section 2.4 shows a high temperature emissometry setup that can directly measure the sample emittance at temperature up to 1000^oC.

2.1 FTIR Bench for Specular Reflectance Measurements at Normal and Oblique incidence

Figure 2.1(a) shows the experimental setup for specular reflectance measurement. An FTIR spectrometer (Thermo Scientific iS50) along with a variable-angle reflectance accessory (Harrick, Seagull) is employed to measure the specular reflectance of the sample at different wavelengths, incidence angles, and polarization states. The FTIR spectrometer covers a wide spectral range from 0.4 to 20 μm. A silicon detector is used for collecting spectra at wavelengths from 0.4 μm to 1 μm, while a DTGS detector is

utilized for wavelengths from 1 μm to 20 μm. A visible-NIR broadband polarizer (Thorlabs, WP25M-LIB) is employed to select either TM or TE waves at oblique angles. The reflectance from 0.4 to 1.1 μm in wavelength is measured by an internal Si detector, while a DTGS detector is employed for longer wavelengths beyond 1.1 μm. An Al mirror is used as the reference for reflectance measurement and the measured reflectance is normalized based on the theoretical reflectance of Al by: $R_{\text{corrected}} = R_{\text{measured}} \cdot R_{\text{Al}}$. Where R_{Al} is the theoretical reflectance of Al calculated with its optical constants obtained from Palik [95].

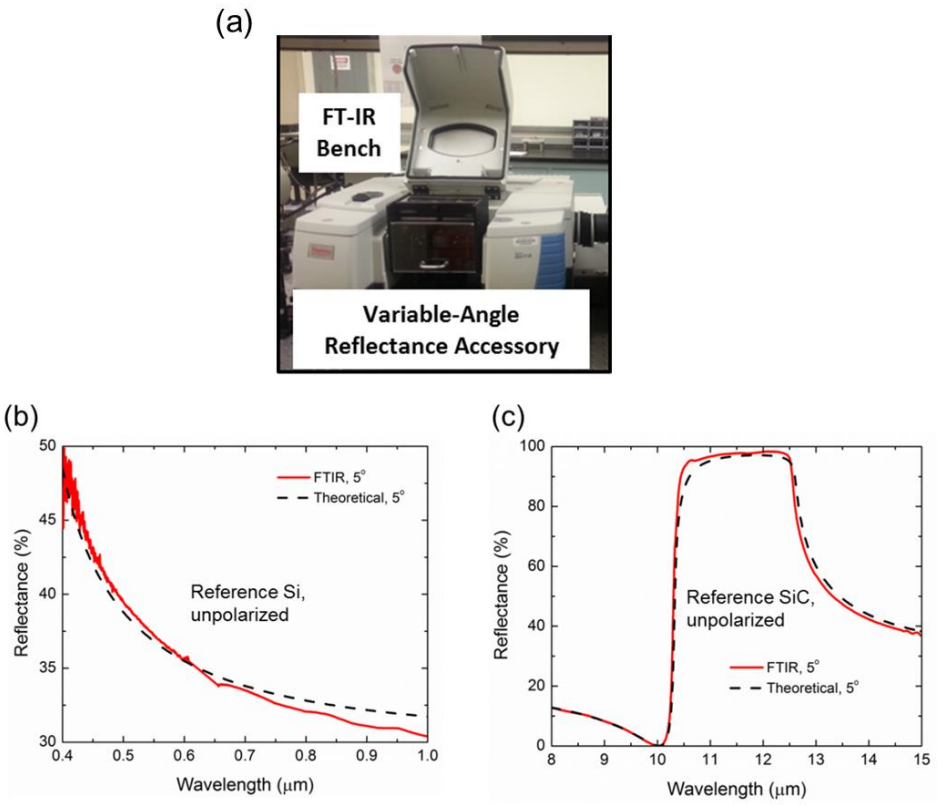

Figure 2.1 (a) A photo of the experimental setup for the FTIR spectrometer and microscope; (b) Measured specular reflectance for reference Si; (c) Measured specular reflectance for reference SiC.

Figure 2.1(b) shows the measured specular reflectance for reference Si (Virginia Semiconductor, Boron doped (110) Si sample, with resistivity of 60 ohms-cm) incident by unpolarized light at 5^o, the theoretical reflectance of Si is also plotted for comparison. The measured spectral range is from 0.4 to 1 μm, this is because Si wafer is not opaque at longer wavelength beyond its bandgap (1.1 μm), while the Seagull reflectance accessory can only measure opaque samples. It can be observed that the difference between FTIR measurement and theory is within 2%. Figure 2.1(c) plots the measured reflectance for SiC reference sample from 8 to 15 μm, where it is opaque due to the phonon absorption band of SiC. It is observed that the theoretical and measured reflectance matches well, except that there is a difference less than 5% from 10.5 to 11 μm. The difference between theory and measurement may come from the impurity/doping in reference sample, difference in actual and theoretical optical constants, systematic and occasional error during the FTIR measurement.

2.2 Tunable Light Source and Integrating Sphere for Hemispherical and Diffuse Reflectance Measurement

Figure 2.2(a) and (b) shows the tunable light source & integrating sphere setup for the hemispherical and diffuse reflectance measurement. A tunable light source (Oriel, TLS-250Q), which consists of a QTH light source and a monochromator, is employed along with a customized 8^o VIS-NIR integrating sphere (IS) (Labsphere Inc.) to measure the hemispherical reflectance in the visible and NIR region. An optical chopper (Newport, 75163) is used to modulate the light signals and a lock-in amplifier (Newport, 70100) is utilized to improve the signal-to-noise ratio. A silicon detector (Thorlabs, SM05PD1A,

from 0.4 μm to 1 μm) and an InGaAs detector (Thorlabs, SM05PD5A, from 1 μm to 1.6 μm) are used at respective operating wavelengths. The sample is mounted at the back-side sample holder of the IS, with an incidence angle of 8°. Besides hemispherical reflectance, the diffuse reflectance can also be measured independently by employing a light trap (position A) to absorb the specular component of reflected energy.

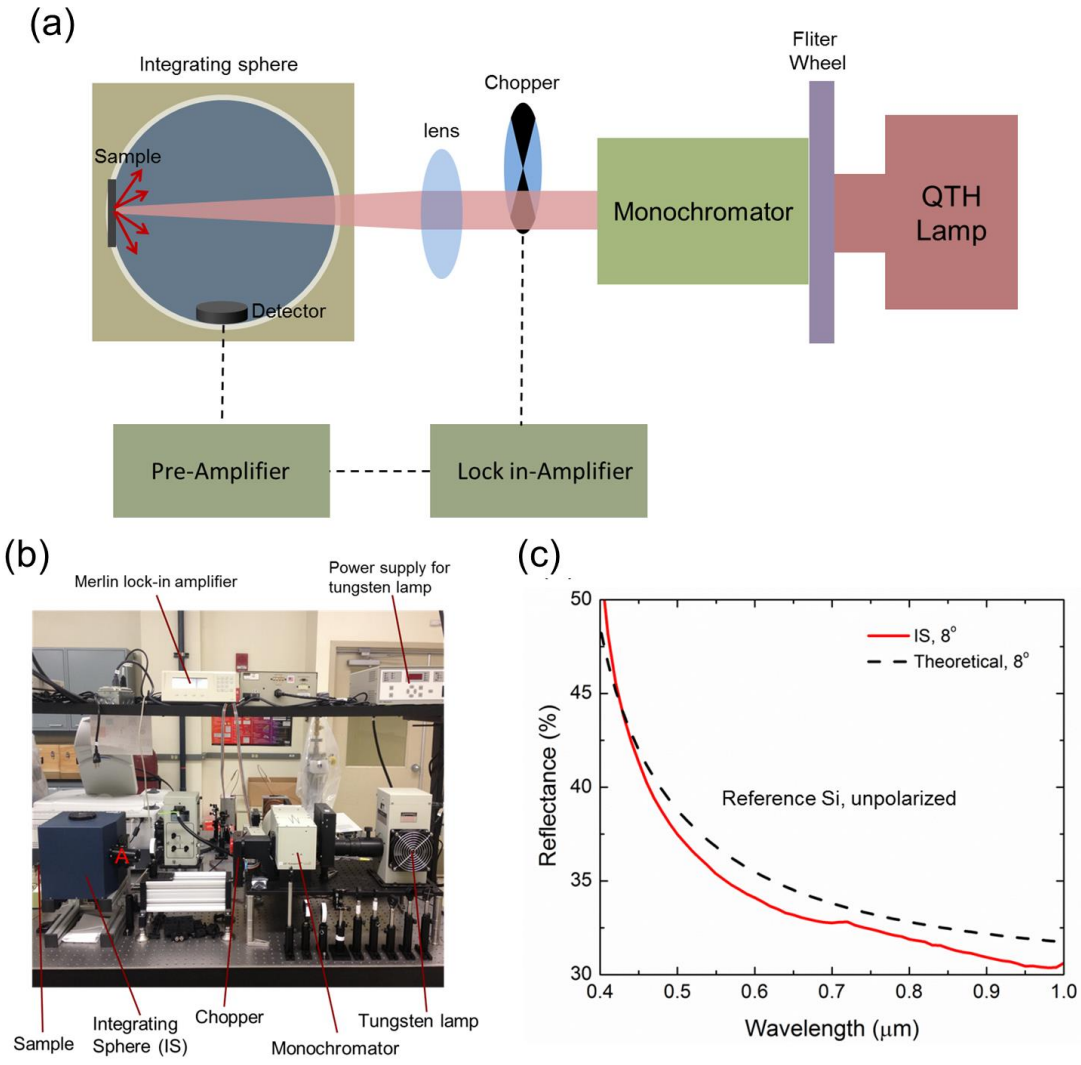

Figure 2.2 (a) The schematic and (b) A photo of the tunable light source coupled with the integrating sphere; (c) Hemispherical reflectance of undoped silicon measured in the integrating sphere compared with theoretical value.

An aluminum mirror is employed as the reference surface to obtain the background signal for reflectance measurement, and a mask is placed in front of the sample to shrink the beam size to measure samples with small area. Note that the mask will reflect part of the incident light, therefore the measured reflectance should be corrected considering the reflectance of the mask by:

$$R_{\text{corrected, total}} = \frac{S_{\text{sample \& mask,tot}} - S_{\text{mask,tot}}}{S_{\text{Al \& mask,tot}} - S_{\text{mask,tot}}} = \frac{R_{\text{sample \& mask,tot}} - R_{\text{mask,tot}}}{1 - R_{\text{mask,tot}}} \tag{2.1}$$

$$R_{\text{corrected, diffuse}} = \frac{S_{\text{sample \& mask,diffuse}} - S_{\text{mask,diffuse}}}{S_{\text{Al \& mask,tot}} - S_{\text{mask,tot}}} = \frac{R_{\text{sample \& mask,diffuse}} - R_{\text{mask,diffuse}}}{1 - R_{\text{mask,tot}}} \tag{2.2}$$

where $R_{\text{corrected, total}}$ is the corrected hemispherical reflectance, $R_{\text{corrected, diffuse}}$ is the corrected diffuse reflectance, $S_{\text{sample \& mask,tot}}$ is the total reflected energy from sample and mask, $S_{\text{mask,tot}}$ is the total reflected energy from mask only, $S_{\text{Al \& mask,tot}}$ is the total reflected energy from Al mirror and mask, $S_{\text{sample \& mask,diffuse}}$ is the diffuse reflected energy from sample and mask, $S_{\text{mask,diffuse}}$ is the diffuse reflected energy from mask only, $R_{\text{sample \& mask,tol}}$ is the measured hemispherical reflectance for the sample and mask, $R_{\text{mask,tol}}$ is the measured total reflectance for mask, $R_{\text{sample \& mask,diffuse}}$ is the measured diffuse reflectance for sample and mask, and $R_{\text{mask,diffuse}}$ is the measured diffuse reflectance for mask. The measured reflectance should also be corrected by the theoretical reflectance of Al mirror:

$$R_{\text{final}} = R_{\text{corrected}} \cdot R_{\text{Al}} \tag{2.3}$$

where R_{Al} is the theoretical reflectance of Al with its permittivity obtained from Palik.

Figure 2.2 (c) shows the measured hemispherical reflectance for reference Si sample compared with theory. The reflectance is measured from 0.4 to 1 μm with spectral resolution of 10 nm, note that the Si sample is specular, therefore the diffuse

reflectance is negligible. Comparing theory with IS measurement, it can be found that the difference is within 2%, indicating high accuracy for IS measurement.

2.3 In-Situ FTIR Fiber Optics for High Temperature Reflectance Measurement

Figure 2.3(a) and (b) respectively show the schematic and photo for the experimental setup of high temperature reflectance measurement with fiber optics. A FTIR fiber coupler (Harrick, Fibermate2) is employed to couple the FTIR with a visible–NIR (Thorlabs, RP21) or IR (High Tech Photonics, AP10757) Y-shape fiber bundle. A fiber probe with collimating and focusing optics yields a beam spot with diameter of 4 mm onto the sample surface, and the normally reflected signal is then collected by the same probe and acquired by the FTIR detectors through optical fibers. The sample is mounted onto the copper disk inside a heater assembly. A thermocouple is utilized to measure the sample temperature and send it to a temperature controller (Omega, CSi8DH), which modulates the power input of the heater and therefore accurately maintains the sample temperature at the setpoint. An aluminum mirror is used as the reference for reflection measurement.

Figure 2.3(c) plots the measured reflectance for reference Si at room temperature with unpolarized incidence, along with the theoretical reflectance and specular reflectance measured by FTIR. The red curve represents the reflectance measured with fiber optics, it can be observed that the curve is fluctuating in visible-blue regime due to the low signal to noise ratio using optical fibers. The blue and black curve respectively shows the reflectance measured by FTIR and the theoretical reflectance. Comparing these

three curves, it is found that difference for these three curves is within 2.5%, indicating the reasonable accuracy of fiber optics measurement.

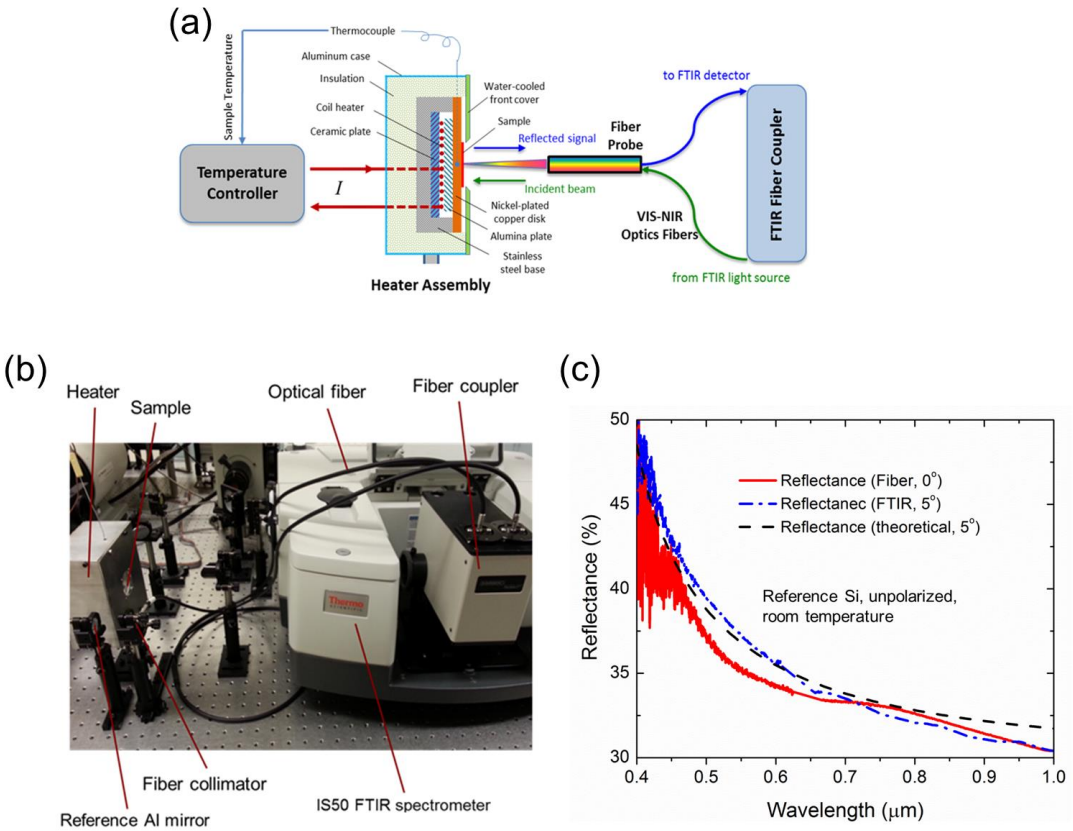

Figure 2.3 (a) Schematic of the experimental setup for the temperature-dependent FTIR fiber optics measurements for characterizing spectral normal reflectance at elevated temperatures. (b) A photo of the FTIR fiber optics setup; (c) Specular reflectance of undoped silicon measured by the FTIR fiber optics setup compared with theoretical value

2.4 High Temperature Emissometry

This section will introduce an emissometry setup to directly measure the sample emittance at high temperatures. Figure 2.4 (a) shows the schematic for the emissometry setup, with a blackbody (Newport, 67030) providing the reference signal and a sample heater to generate the sample signal. The customized sample heater can heat the sample up to 1000^{o}C, with a temperature controller (Omega, CSi8DH) to stabilize the sample temperature at its setpoint. A 1" gold mirror is mounted on a motorized translation stage (Standa, 8MT30-50) and a rotation (Standa, 8MR174-11-20) stage to switch between the blackbody and sample heater.

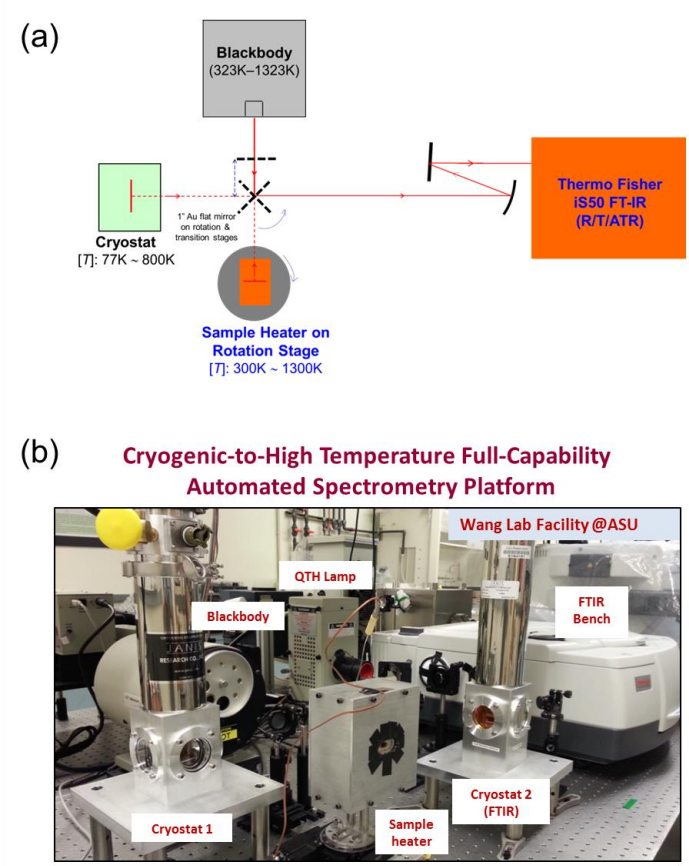

Figure 2.4 (a) Schematic and (b) A photo for the high temperature emissometry setup.

The sample emittance can be measured as:

$$\varepsilon'_{\lambda} = \frac{S_{\text{Sample}} - S_{\text{bg}}}{S_{\text{BB}} - S_{\text{bg}}} \tag{2.4}$$

where ε'_{λ} is the spectral directional emittance, S_{Sample} is the measured signal from the sample mounted in the heater, S_{BB} is the reference signal from the blackbody, and S_{bg} is the background signal. Note that S_{bg} resulting from the background thermal radiation is corrected in Eq. (2.4), and S_{bg} is measured with the gold mirror facing the surrounding background. Figure 2.4(b) presents a photo for the emissometry setup, it is worth mentioning that two croystats are also shown in this photo, which can be used for cryogenic to high temperature measurement in vacuum.

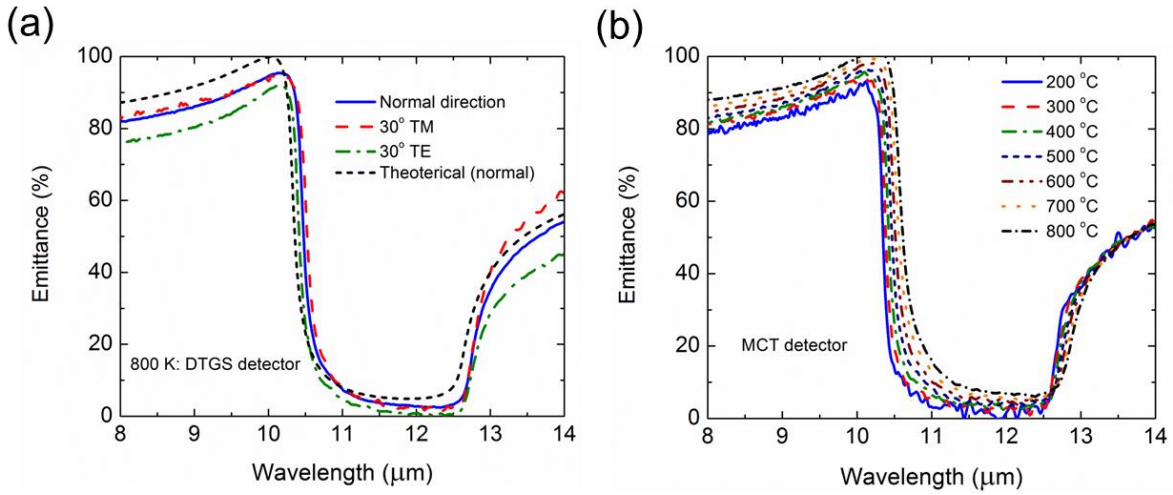

Figure 2.5 Measured emittance for SiC at various (a) incidence angles and (b) temperatures with the high-temperature emissometry setup.

Figure 2.5 shows the emittance for a reference SiC sample measured with the high temperature emissometry setup. Figure 2.5(a) presents the measured emittance at 800 K with the DTGS detector, with incidence angle of 0^{o} and 30^{o}. Note that the emittance at

oblique incidence is different for TE and TM waves, so they are measured separately. The theoretical emittance of SiC is also compared with the measurement results in Fig. 2.5(a), and it can be observed that the theory and measurement shows reasonable match with difference smaller than 5%. It is also found that the emittance for TM wave at 30^{o} is slightly higher than the emittance for TE wave, which is reasonable since TE wave has a higher reflectance generally. Figure 2.5(b) presents the emittance measured from 200^{o}C to 800^{o}C for the SiC sample. Note that the signal strength for thermal radiation is weak at lower temperatures, so the MCT detector with a higher responsivity was employed for the measurement. The measurement was taken at normal incidence, thus the measurement was performed with unpolarized wave. It was observed that the emittance slightly increases as temperature becomes higher. This is due to the change of material property with temperature or the non-linear response of the MCT detector.

CHAPTER 3

HIGHLY EFFICIENT SELECTIVE SOLAR THERMAL ABSORBERS MADE OF METAMATERIALS AND METAFILMS

This chapter presents the design, fabrication and optical characterization of metamaterial and metafilm selective absorbers. A brief introduction is given in Section 3.1 about ideal solar thermal absorbers, which emphasizes the importance of spectral selectivity. Section 3.2 presents the theoretical design of a grating based metamaterial selective solar absorber via FDTD simulation. Section 3.3 describes the fabrication and optical characterization for the grating based metamaterial solar absorber. A metafilm/multilayer selective absorber is discussed in Section 3.4. The high temperature stability for the metafilm absorber is investigated in this section as well.

3.1 Ideal Solar Thermal Absorbers

Figure 3.1 shows the spectral distribution of solar radiative heat flux at AM 1.5, compared with the radiative heat flux for thermal emission of a blackbody at different temperatures. It can be observed that at the temperature of 400^{o}C, the intensity of thermal emission is comparable to incident solar radiation. It is also found that most of the energy from solar radiation is distributed in visible and near infrared regime, while most of the energy from thermal emission is in the mid-infrared range, which is basically the energy loss from the surface solar absorbers. Figure 3.1 also shows the absorptance for an ideal absorber, which exhibits unity absorptance below the cutoff wavelength to maximize

absorbed solar radiation, and zero emittance beyond cutoff wavelength to minimize thermal re-emission. Note that the cutoff wavelength strongly depends on the absorber temperature as the spectral distribution for the intensity of thermal radiation is strongly affected by the temperature.

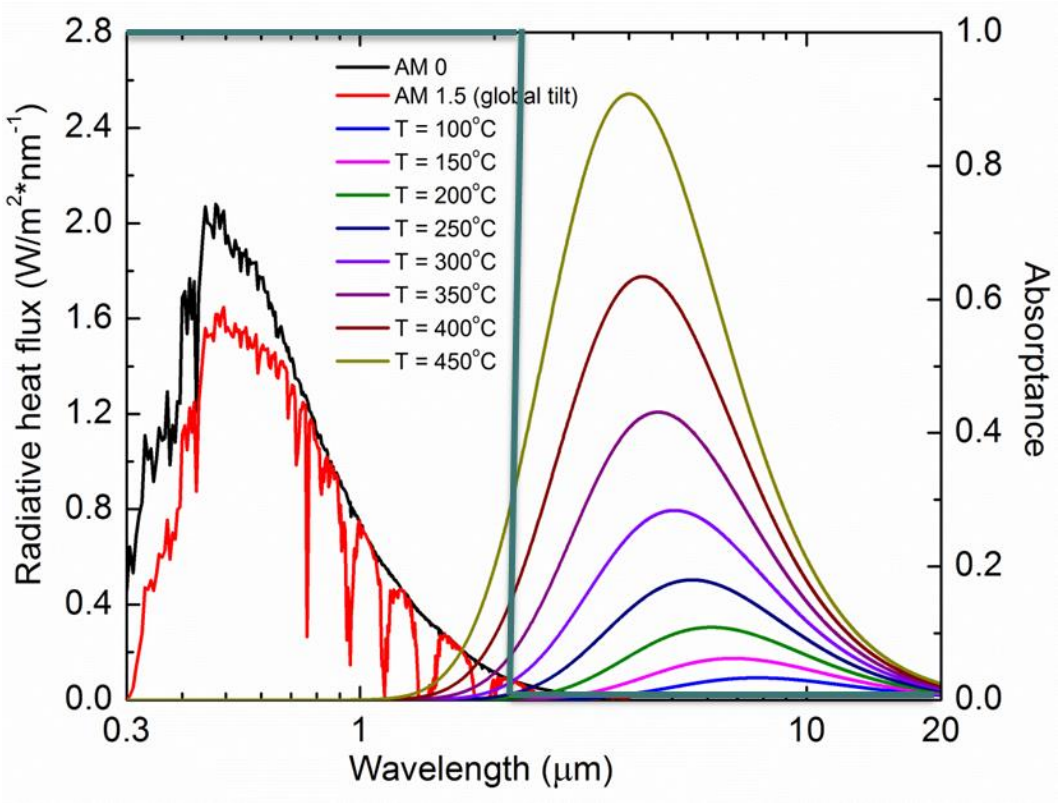

Figure 3.1 Spectral intensity distribution for solar and thermal radiation, as well as the absorptance/emittance for an ideal solar absorber.

3.2 Grating Based Metamaterial Selective Solar Absorber

3.2.1 Theoretical Design of the Metamaterial Selective Solar Absorber

The theoretical design of a metamaterial selective absorber is discussed in section 3.2.1. Figure 3.2 depicts the schematic for the metamaterial absorber, which is a film-coupled structure with tungsten grating and substrate separated by a SiO_2 spacer. The geometric parameters are also labeled in Fig. 2(a). The single sized metamaterial solar

absorber has same sized grating on the top (i.e., $w_1 = w_2$), with grating period Λ, grating height h, and spacer thickness t. On the other hand, the double sized structure exhibits tungsten patches with different width of w_1 and w_2. A wavevector K_{inc} represents the electromagnetic wave with a free-space wavelength λ incident onto the metamaterial structure at a polar angle (or incidence angle) θ, polarization angle ψ, and azimuthal angle ϕ. The polar angle θ denotes the angle between K_{inc} and the surface normal of the structure (i.e., z direction). The angle ψ between electric field vector E and the plane of incidence, defined by K_{inc} and the structure surface normal, is the polarization angle. ψ = 0° indicates the transverse magnetic (TM) polarized wave while ψ = 90° gives the transverse electric (TE) polarized wave. Azimuthal angle ϕ is the angle between the x axis and the plane of incidence, and is taken as ϕ = 0° here for simplicity.

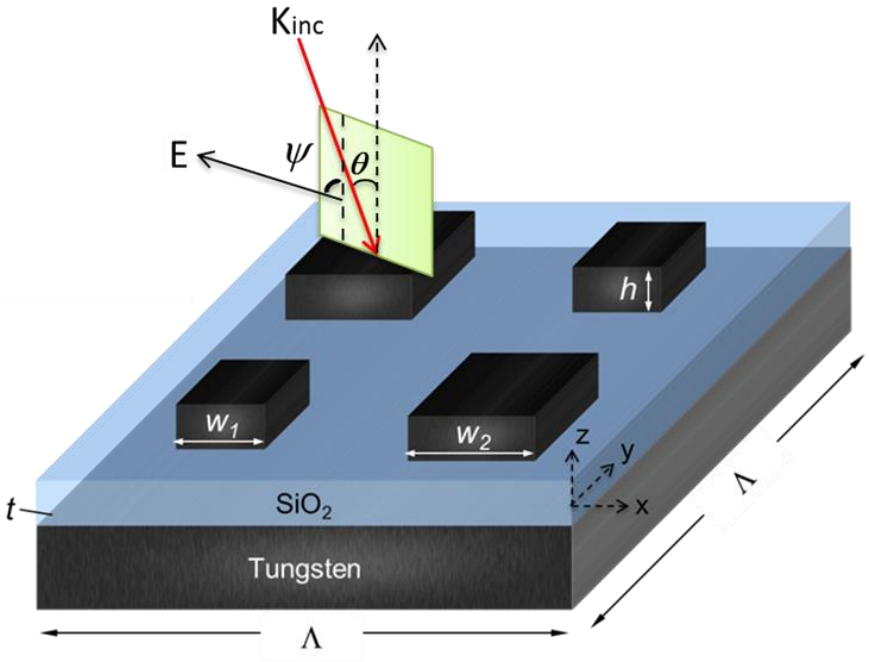

Figure 3.2 Schematic of the metamaterial selective solar absorber.

The finite-difference time-domain (FDTD) method (Lumerical Solutions, Inc.) is

used for calculating the radiative properties of the proposed metamaterial absorbers in a broad spectral region from UV to mid-infrared (i.e., 0.3 μm to 20 μm). The optical constants of tungsten and SiO_2 are both taken from Palik. A broadband linearly polarized plane wave source simulating the incident electromagnetic waves is placed one micron away from the structure. Periodic boundary condition is applied at normal incidence in the x and y directions of the simulation domain, while Bloch boundary condition is used for oblique incidence to account for the phase difference in the periodic structures. Perfectly matched layers with reflection coefficients less than 10^{-6} are placed at the boundaries along the z direction. Non-uniform meshes with minimum mesh size of 5 nm are used, and the relative difference in absorptance is within 0.3% compared with that obtained by a minimum mesh size of 3.3 nm. A frequency-domain field and power monitor is placed above the plane wave source to collect the reflected waves, from which the spectral-directional reflectance at different polarization states can be obtained. A spectral resolution of 5 nm is used for the numerical simulations and is sufficient to resolve the spectra of the radiative properties of studied metamaterial absorbers. The spectral-directional absorptance can be calculated from $\alpha'_\lambda = 1 - R'_\lambda$ since the metamaterial structure is opaque.

The geometric effects on the spectral absorptance of single-sized metamaterial solar absorber at normal incidence is investigated first, aiming to elucidate the physical mechanisms responsible for the enhanced absorption and to optimize geometric parameters to achieve higher absorption in the visible and near-infrared region. The effects of patch width *w*, grating period *Λ*, grating height *h*, and spacer thickness *t* are considered starting from a set of base geometric parameters of *Λ* = 600 nm, *w* = 300 nm,

and $h = t = 60$ nm. Other parameters are fixed at the base values when a specified geometric parameter varies during the numerical simulations. The polarization angle ψ is set to be 0° with the oscillating magnetic field H along the y direction, and the absorptance at TM incidences is obtained. The radiative properties for TM and TE-polarized waves would be the same at normal incidence due to the geometric symmetry. Figures 3.3(a), 3.3(b), 3.3(c) and 3.3(d) show how the normal absorptance changes with patch width w, grating period Λ, grating height h, and spacer thickness t, respectively, in the spectral region from 0.3 μm to 4 μm, where most of solar energy is confined.

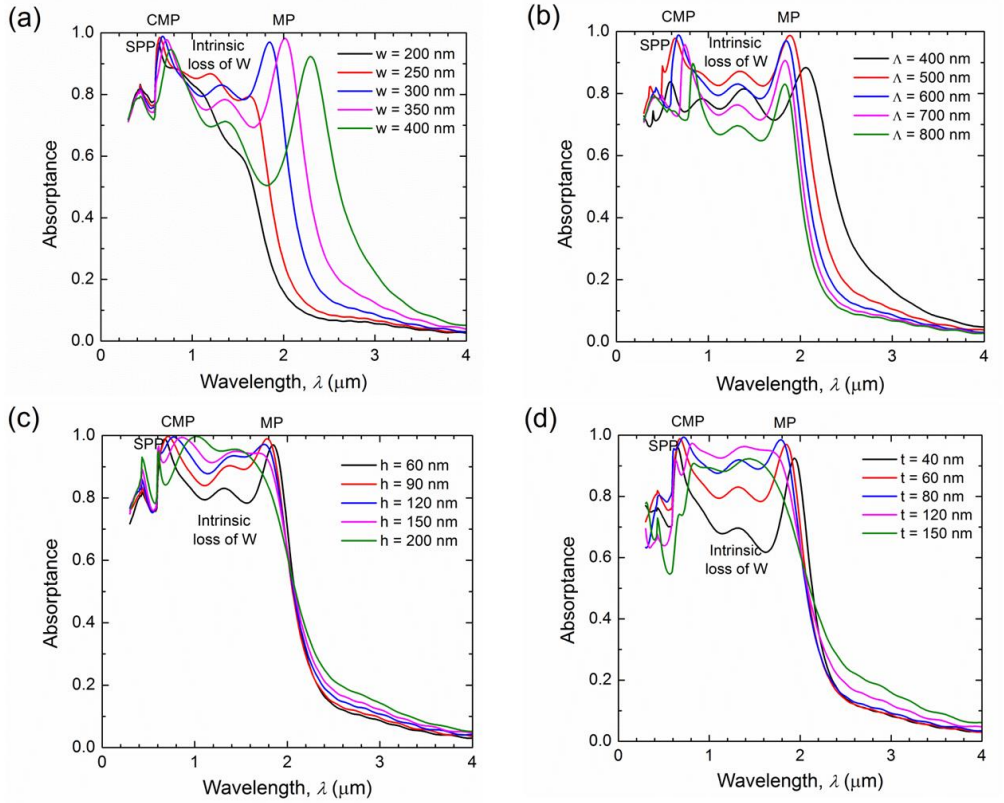

Figure 3.3 Spectral absorptance for single sized metamaterial absorber with different: (a) Grating width; (b) Grating period; (c) Grating height; (d) Spacer thickness.

When the patch width w changes from 200 nm to 400 nm, as shown in Fig. 3.3(a), the normal absorptance is enhanced significantly due to the growth of an absorption peak around λ = 2 μm. Note that, the peak magnitude increases up to 1 at the width of w = 350 nm, and the peak wavelength shifts to longer wavelengths with larger width values. In the meantime, another peak with absorptance more than 0.95 exists around 0.7 μm, and shows much less dependence on the patch width, although the peak shifts slightly to longer wavelengths with larger width. Similar emittance peaks have been found previously in the similar tungsten metamaterial TPV emitters made of 1D and 2D gratings with w = 300 nm, and are attributed to the excitations of MP and SPP modes at longer and shorter wavelengths, respectively. In fact, the absorption peak around 0.7 μm is the hybrid of a SPP mode and a coupled magnetic polariton (CMP) mode, to be explained later with the help of electromagnetic field distribution. The minor absorption peaks around λ = 0.4 μm and 1.4 μm between the two major ones are due to the intrinsic loss associated with the interband transitions in tungsten. It can be clearly observed from this figure that the absorptance (or emittance) drops sharply at wavelengths beyond the MP resonance.

Figure 3.3(b) shows the effect of grating period Λ on the normal spectral absorptance of the single-sized metamaterial solar absorber when it varies from 400 nm to 800 nm. It can be observed that the MP peaks around λ = 1.8 μm remains almost un-shifted, except for Λ = 400 nm, in which case the coupling across the small gap between neighboring patches has some effects on MP peaks. On the other hand, the SPP peaks shift to longer wavelengths with increased grating period. Surface plasmon polaritons or SPPs are the coupling of the collective oscillation of surface charges at the interface to

the external electromagnetic waves at specific wavelengths. The excitation of SPPs between two nonmagnetic materials is determined by the dispersion relation $k_{spp} = (\omega/c_0)\sqrt{\varepsilon_1\varepsilon_2/(\varepsilon_1+\varepsilon_2)}$, where ε_1 and ε_2 are the dielectric functions of materials at each side of interface respectively, and their real parts should have opposite signs to excite SPPs. The SPP resonance wavelengths strongly depend on the grating period Λ and incidence angle θ. Zhao et al. have provided a detailed discussion on the behavior of SPPs at normal and oblique incidence for the 2D TPV emitter with the similar structure. Therefore, the SPP behavior will not be elaborated here again. In addition, it's interesting to notice that as grating period increases, the CMP peaks also shift to longer wavelengths.

Figure 3.3(c) presents the effect of grating height *h* on the normal absorptance of the single-sized metamaterial solar absorber. When *h* varies from 60 nm to 200 nm, the absorptance spectrum from 0.6 μm to 1.8 μm is enhanced with larger *h* values. The MP peak around λ = 1.8 μm depends little on the grating height, and shifts slightly toward shorter wavelength with increasing *h*. The absorptance at the MP peak could be close to 1 with *h* = 90 nm, and the absorptance drops abruptly beyond the MP peak, resulting in absorptance values of 0.5 around λ = 2 μm and below 0.05 at λ = 4 μm. On the short wavelength side, the sharp SPP peak at λ = 0.6 μm does not change with the grating height. However, another peak, associated with the CMP mode, starts to separate from the SPP mode around λ = 0.6 μm, and shifts to longer wavelengths with thicker tungsten patches or larger h values. As a result, a broad absorption band from 0.6 μm to 1.8 μm with $\alpha'_\lambda > 0.9$ is achieved with h = 150 nm.

As shown in Fig. 3.3(d), spacer thickness *t* yields a similar effect as the grating height on the normal absorptance of the single-sized metamaterial solar absorber. When the spacer thickness changes from 40 nm to 150 nm, the MP peak shifts to shorter wavelength, while the peak amplitude first increases to a maximum close to 1 with t = 80 nm and then drops with further thicker spacers. The SPP peak locations do not change with spacer thickness but the amplitudes change with different t values. The CMP peak separates from the SPP peak around λ = 0.6 μm, and shifts slowly towards the longer wavelength with increasing *t*. As a result, the absorptance in the spectral region between 0.6 μm to 1.8 μm is greatly enhanced, with the minimum value of spectral absorptance increases from 0.6 at t = 40 nm to 0.92 at t = 120 nm. However, the absorptance starts to decrease with further thicker spacers.

Besides the MP, CMP and SPP resonance modes, which enhance the absorptance around several particular wavelengths, another important factor for the broadband high absorption is the high intrinsic loss of tungsten used here. Tungsten has several interband transitions around the wavelengths of 0.4 μm, 0.6 μm and 1.4 μm. Metals with relatively low losses such as Ag and Au have been commonly considered for constructing plasmonic metamaterials for potential sensing, imaging and cloaking applications. However, for solar thermal applications, high intrinsic loss is actually beneficial to enhance the absorption of solar radiation across a wide spectral range, therefore tungsten is chosen here. The most important factor to achieve almost perfect absorption in a broad spectral band from visible to the near-infrared region with the designed metamaterial absorber is the coupling effect between different resonance modes and interband

absorption of tungsten. One would expect that the absorptance will be reduced if the resonance modes are far apart and could not effectively couple with each other.

Clearly, the absorptance of the singled-sized metamaterial solar absorber strongly depends on the geometric parameters. Several absorption peaks, associated with the excitations of MP, CMP and SPP modes as well as the intrinsic loss of tungsten, can be clearly seen, and the coupling between these modes results in a broad and enhanced absorption band in the visible and near-infrared region. The peak wavelengths of the MP and CMP modes also show strong dependence on the patch width w, grating period Λ, grating height h, and spacer thickness t, which could be potentially employed to further broaden the absorption peak. The absorption could be also maximized by optimizing the geometric parameters. In order to further understand the physical mechanisms for the absorption enhancement, the behaviors of MP and CMP modes are elucidated below with electromagnetic field distribution.

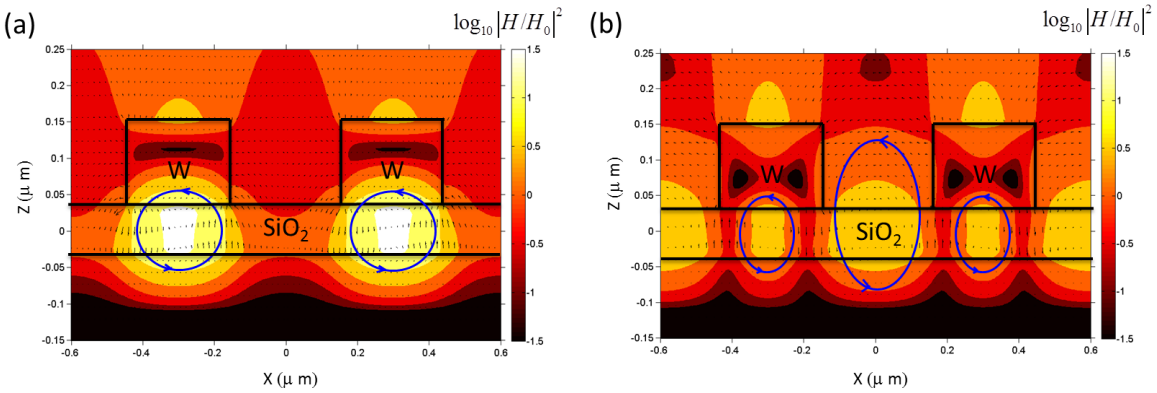

Figure 3.4 Electromagnetic field distribution for the single sized metamaterial absorber at (a) MP resonance; (b) CMP resonance.

Figure 3.4(a) presents the electromagnetic field distribution when the magnetic polariton (MP) is excited at λ = 1.75 μm inside the single-sized metamaterial solar

absorber with geometric parameters of Λ = 600 nm, w = 300 nm, h = 120 nm, and t = 60 nm, calculated from FDTD at normal incidence. The electromagnetic field in two unit cells is shown at the x-z cross section in the middle of the tungsten patch. The contour represents the strength of magnetic field normalized to the incidence, i.e., $\log_{10}|H/H_0|^2$, suggesting the local H field enhancement or suppression. The arrows are the electric field vectors, indicating the direction and strength of induced electric current. Clearly, there is a strong confinement of electromagnetic energy inside the SiO_2 spacer between the top tungsten patches and bottom tungsten film. The strongest field enhancement occurs at the center of the spacer with 1.5 orders of magnitude higher than the incident H field. At the same time, the electric field vectors indicate an induced current loop around the anti-node of the magnetic field. This field pattern is exactly the characteristics of excitation of magnetic resonance, which has been discussed in detail in similar grating structures from previous studies. The basic mechanism is that, the free charges at the tungsten surfaces resonate with incident electromagnetic waves and induce oscillating electric current, which results in resonant magnetic field according to Lenz's law.

Figure 3.4(b) shows the electromagnetic field distribution when the CMP is excited at λ = 0.78 μm in the single-sized metamaterial absorber. Besides the strong magnetic field enhancement and an induced current loop which can be seen inside the spacer between the upper tungsten patches and the bottom tungsten film, which is similar to the behavior of MP, the electric field vectors form another current loop inside the gap between the neighboring tungsten patches, along with strong magnetic field enhancement mainly inside the spacer layer. The localized field could be one order of magnitude stronger than the incident field. The field distribution indicates that two magnetic

polaritons are excited in one unit cell, one is between upper tungsten patches and the film and the other is between neighboring patches. Therefore, coupled magnetic polariton (CMP) is named for this resonance mode. In fact, similar CMP mode has been seen in double-layer 1D Ag grating structures separated by a SiO_2 spacer.

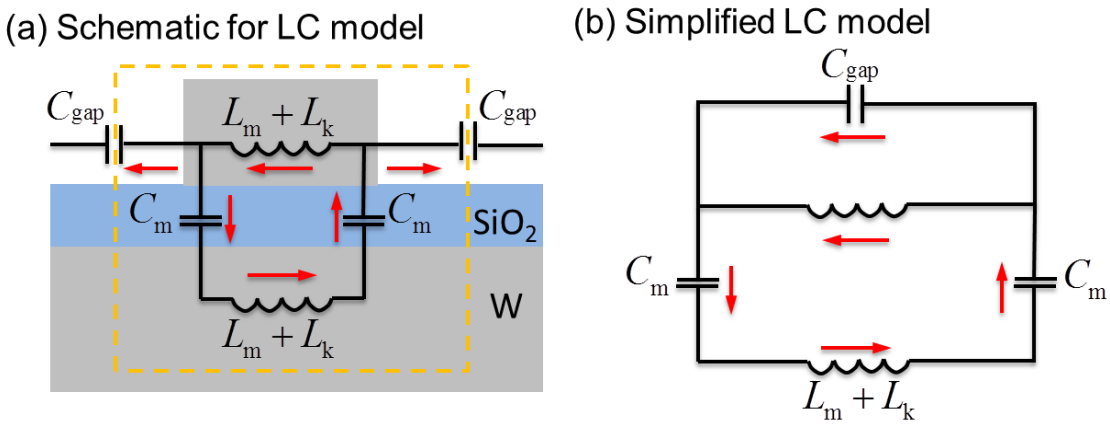

Figure 3.5 (a) A schematic for the *LC* circuit model; (b) The simplified LC circuit model.

An analytical inductor-capacitor (*LC*) model with the illustration shown in Fig. 3.5 can be used to predict the resonance frequency of MP. The interaction between the upper tungsten patches and the bottom tungsten thin film can be represented by a parallel-plate capacitor with $C_m = 0.22\varepsilon_{SiO_2}\varepsilon_0 w/t$ per unit length, and a parallel-plate inductor with $L_m = 0.5\mu_0 wt$ per unit length. The interaction between the neighboring tungsten patches can be modeled as a gap capacitor $C_g = \varepsilon_0 h/(\Lambda - w)$ per unit length. Therefore, the impedance for the LC circuit is:

$$Z_{total} = \frac{L_m + L_k}{1 - \omega^2 C_g (L_m + L_k)} - \frac{2}{\omega^2 C_m} + (L_m + L_k) \tag{3.1}$$

While the resonance frequency can be obtained by zeroing the impedance got from Eq. (3.1), the coupling between neighboring patches is weak for large gaps between the neighboring patches, and the effect of C_g can be neglected when C_g is less than 5% of C_m. In this case, the resonance wavelength of MP can be obtained by:

$$\lambda_{MP} \approx 2\pi c_0 \sqrt{(L_m + L_k)C_m} \tag{3.2}$$

where $L_k = -w/(\omega^2 \varepsilon_0 \varepsilon'_{tungsten} \delta)$ is the kinetic inductance per unit length, accounting for the contribution from drifting charges at nanoscale. $\varepsilon'_{tungsten}$ and δ are the real part of the dielectric function and the penetration depth of tungsten, respectively.

The magnetic resonance wavelengths are calculated based on Eq. (3.2) and plotted as a function of different geometric parameters in Figs. 3.6(a), (b), (c) and (d). The predicted MP resonance wavelengths agree well with the FDTD simulation on the effects of patch width *w*, grating period Λ and spacer thickness *t*. The dependence of MP wavelength on the width can be understood by the fact that, larger width will result in larger values for capacitance C_m and inductance L_m and L_k, and thus increasing MP resonance wavelengths. Similarly, thicker spacers will lead to smaller $L_k C_m$ values, while the other term $L_m C_m$ is independent on the spacer thickness *t* in the *LC* model. Therefore, the MP wavelength decreases with larger *t* values. The *LC* model indicates that resonance wavelength slightly decreases as grating period increases, which matches with the FDTD simulation quite well.

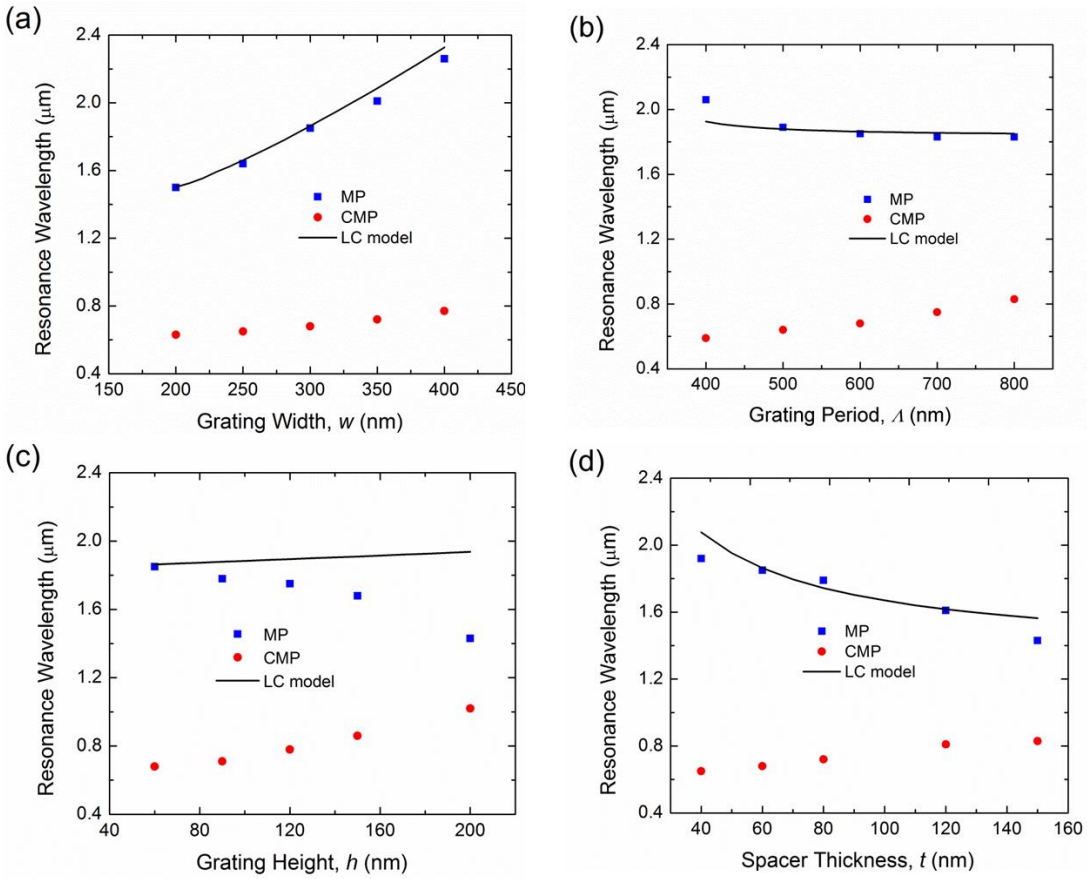

Figure 3.6 The MP resonance frequency predicted by the *LC* model compared with the resonance frequency from FDTD simulation for single sized metamaterial absorber with various (a) Grating width; (b) Grating period; (c) Grating height; (d) Spacer thickness.

On the other hand, the *LC* model indicates that increasing grating height will slightly increase the MP wavelength, however, the FDTD simulation suggests that the MP wavelength decreases slightly with increasing *h*. Note that, the *LC* model is based on several approximations and could not consider the coupling effect between MP and other modes, which may account for the discrepancy on the effect of grating height between the FDTD simulation and *LC* model.

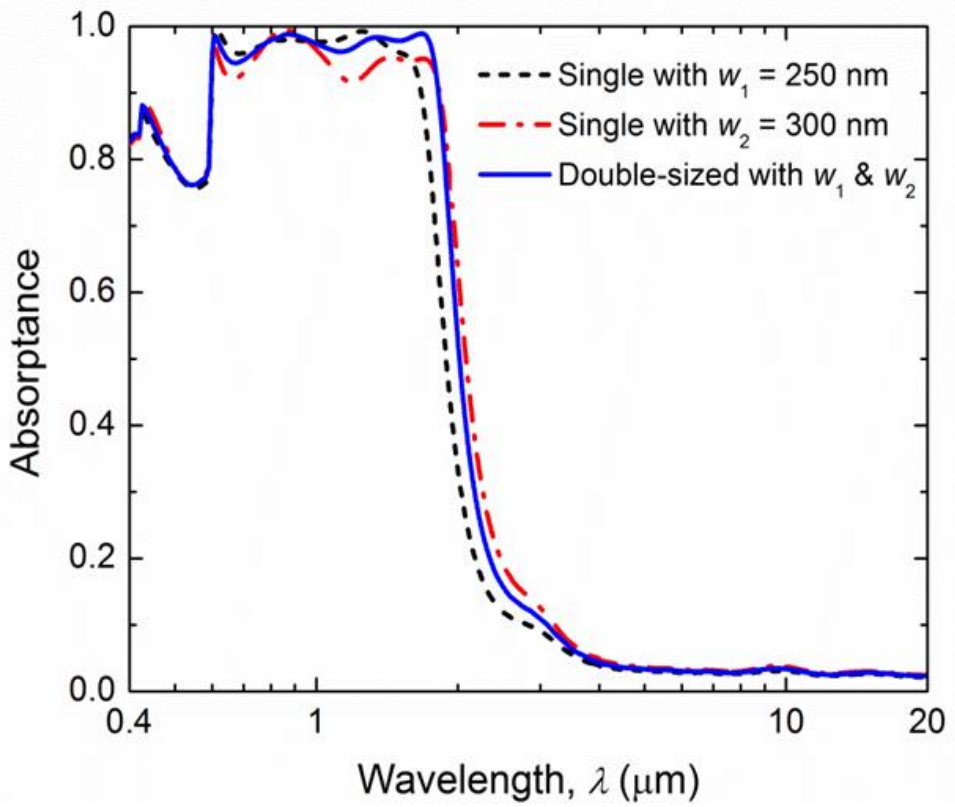

Figure 3.7 Spectral absorptance for the single and double sized metamaterial selective absorber with optimized geometry.

Figure 3.7 shows the absorptance of two single-sized metamaterial absorbers with the same geometric parameters of Λ = 600 nm, h = 150 nm and t = 60 nm but different patch widths w_1 = 250 nm and w_2 = 300 nm, respectively. The grating height h is optimized from the geometric study such that the single-sized metamaterial could have close-to-unity absorptance in the visible and near-infrared region. The single-sized metamaterial absorber with larger patch width w_2 = 300 nm has a broader band of absorption but a little bit lower absorptance in the near-infrared, than the one with smaller patch width of w_1 = 250 nm.

Here we further consider a double-sized metamaterial consisting of patches with two different widths of w_1 = 250 nm and w_2 = 300 nm. Since the MP resonance

wavelengths highly depend on the patch width, MPs could be excited at two different wavelengths determined by different patch sizes. Coupling of these two MP peaks could potentially result in a broader absorption band. The calculated absorptance for the double-sized metamaterial is plotted in Fig. 3.7. By comparison, the double-sized metamaterial has a broader absorption band than the single-sized one with w_1 = 250 nm, and higher absorptance than the single-sized one with w_2 = 300 nm. The minimum absorptance of the double-sized metamaterial is higher than 0.95 in a wide spectral range from 0.6 μm to 1.8 μm. As a selective solar absorber, the low emittance in the longer wavelengths is very crucial to minimize the thermal energy loss from the re-emission of the absorber itself. Figure 3.7 also shows the spectral emittance of the single-sized metamaterials and the double-sized one at normal direction. Clearly, the emittance for the metamaterial solar absorbers is below 0.04 from 4 μm to 20 μm in wavelength. The small peak emittance from 8 μm to 12 μm is due to the phonon absorption of SiO_2.

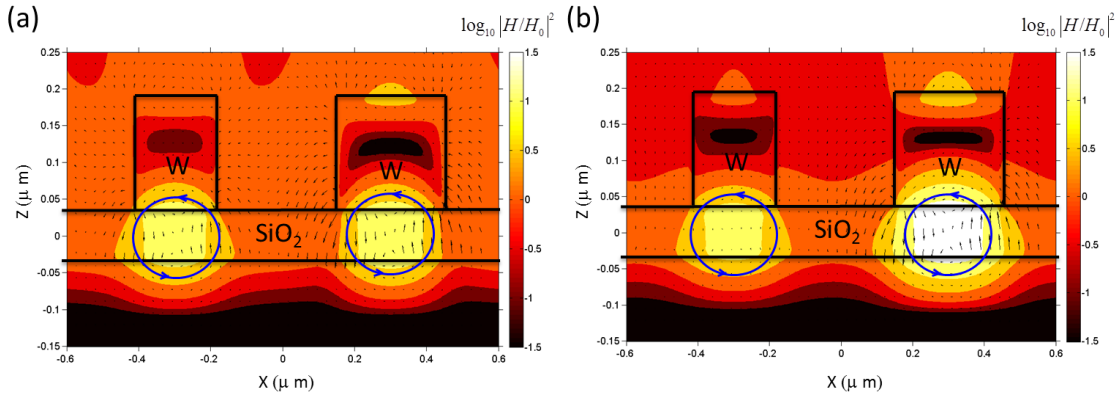

Figure 3.8 Electromagnetic field distributions inside the double-sized metamaterial solar absorber at (a) λ_1 = 1.6 μm and (b) λ_2 = 1.8 μm, which are MP resonance wavelengths of the single-sized metamaterial absorbers with w_1 = 250 nm or w_2 = 300 nm, respectively. The MPs could occur inside the double-sized metamaterial absorbers at both resonance wavelengths under the tungsten patches with different widths of w_1 = 250 nm and w_2 = 300 nm.

To better illustrate the double size effect, the electromagnetic field distributions inside the double-sized metamaterial absorbers are plotted at the MP resonance wavelengths for the single-sized metamaterials with w_1 = 250 nm and w_2 = 300 nm, respectively. As shown in Fig. 3.8(a) at λ_1 = 1.6 μm, MP with local field enhancement can be excited under both patches of different sizes. The excitation of magnetic resonance can be also seen at λ_2 = 1.8 μm in Fig. 3.8(b), while the field localization is much stronger under the larger patch since this wavelength matches well the MP resonance condition for patch with width of w_2. Since the MP wavelengths for w_1 and w_2 are very close, the MPs can be seen under both patches at both resonance wavelengths, indicating strong coupling effect. As a result, the absorption is further enhanced in a broader spectral range inside the double-sized metamaterial absorber.

To quantitatively evaluate the performance of proposed metamaterial structures as solar absorbers, the total solar absorptance (or the fraction of absorbed solar energy) at the normal incidence is calculated by

$$\alpha_{\text{total, N}} = \frac{\int_{0.3\,\mu\text{m}}^{4\,\mu\text{m}} \alpha_{\lambda,N} I_{\text{AM1.5}}(\lambda) d\lambda}{\int_{0.3\,\mu\text{m}}^{4\,\mu\text{m}} I_{\text{AM1.5}}(\lambda) d\lambda} \tag{3.3}$$

Here, $I_{\text{AM1.5}}(\lambda)$ is the spectral intensity of solar irradiation in the US continent taken from the global tilt AM1.5 data [96]. The total absorptance at normal incidence for the single-sized metamaterial absorbers with w_1 = 250 nm and w_2 = 300 nm, and the double-sized one with w_1 and w_2 are 88.06%, 87.96%, and 88.72%, respectively.

While the total absorptance represents the performance to collect solar energy, the total emittance should also be considered as a measurement of thermal energy loss from

the thermal emission of the absorber itself, which can be calculated at normal direction by

$$\varepsilon_{\text{total,N}} = \frac{\int_{0.3\,\mu\text{m}}^{20\,\mu\text{m}} \varepsilon_{\lambda,N} I_{\text{BB}}(\lambda, T_A) d\lambda}{\int_{0.3\,\mu\text{m}}^{20\,\mu\text{m}} I_{\text{BB}}(\lambda, T_A) d\lambda} \tag{3.4}$$

where $I_{\text{BB}}(\lambda, T_{\text{A}})$ is the blackbody spectral intensity at the solar absorber temperature T_{A}. Note that, the total emittance strongly depends on the absorber temperature. Assuming that the absorbers operate at T_{A} = 100°C, the total emittance at normal direction for all three metamaterial solar absorbers are 2.76%, 3.20% and 2.97%, respectively. Therefore, the proposed metamaterial structures could potentially be highly efficient selective solar absorbers with more than 88% solar absorptance and less than 3% total emittance at 100°C.

The directional behavior of the solar absorbers is important for the solar energy absorption at oblique angles. In addition, polarization independence is also critical for a perfect solar absorber to maximize the solar energy absorption since solar radiation is randomly polarized. The effect of polarization angle ψ on the spectral absorptance of the double-sized metamaterial solar absorber is also studied at the normal incidence, shown as the contour plot in Fig. 3.9(a). High absorptance region represented by bright colors can be clearly seen in the short wavelength region from 0.3 μm to 2 μm or so. At a given wavelength, the absorptance does not show any variations with different polarization angles, which changes from 0° to 90°, suggesting the polarization independence of the metamaterial solar absorbers. This is can be understood by the identical behavior between TE (i.e., ψ = 90°) and TM (i.e., ψ = 0°) waves at normal incidence due to the geometric

4-fold symmetry of the double-sized metamaterial structure. For any given polarization with ψ between 0° and 90°, the incident electric field E can be always decomposed into TE and TM polarized waves, resulting in the polarization independence. Therefore, it is crucial to maintain the 4-fold symmetry for designed metamaterial absorbers to achieve polarization independence.

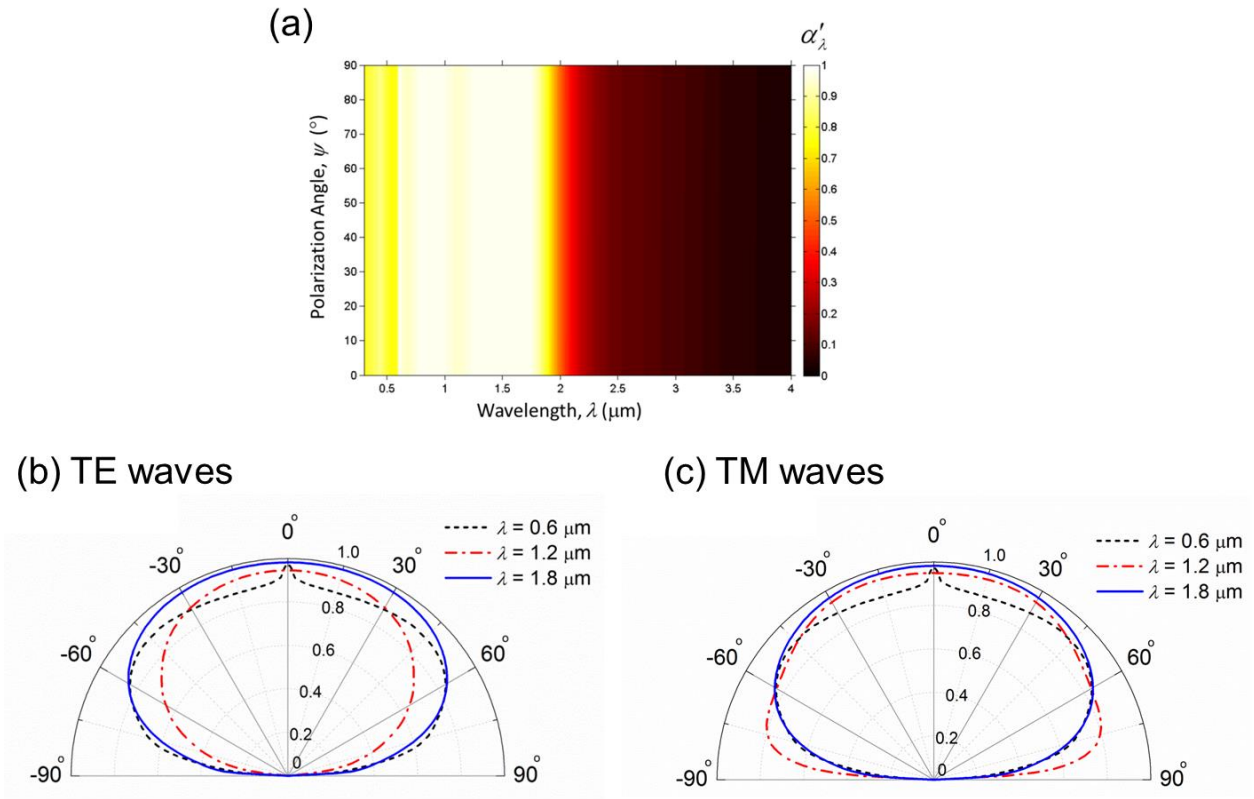

Figure 3.9 (a) The spectral absorptance for multi-sized selective absorber with different polarization angles. The spectral absorptance at λ = 0.6 μm, 1.2 μm and 1.8 μm for (b) TE and (c) TM polarized waves.

Figure 3.9(b) and (c) plots the spectral absorptance of the double-sized metamaterial absorber as a function of polar angle θ at several representative wavelengths of λ = 0.6 μm, 1.2 μm and 1.8 μm for TE (i.e., ψ = 90°) and TM (i.e., ψ =

0°) polarized waves, respectively. At λ = 1.8 μm where the MPs are excited under the tungsten patches, the absorptance is 0.982 at normal incidence, and decreases slightly to 0.975 for TE waves and 0.964 for TM waves at θ = 30°. Even at θ = 60°, the absorptance could be as high as 0.848 for TE waves, and 0.854 for TM waves. The directional-insensitivity at this wavelength is attributed to the directional independence of MPs, which has been discussed previously. The absorptance at λ = 1.2 μm, which is mainly associated with the interband absorption of tungsten, is 0.949 at normal direction. Although the absorptance tends to decrease slightly when the incidence angles increases, the absorptance at θ = 30° is 0.894 for TE waves and 0.941 for TM waves. When the incidence angle changes to 60°, the absorptance is still as high as 0.837 for TM waves, but drops to 0.698 for TE waves. At λ = 0.6 μm there is an absorption peak of 0.98 at normal direction due to the SPP. Since SPP resonance wavelength has strong dependence on the direction, the absorptance then slightly drops but maintains around 0.88 at a broad angular range from 5° up to 60° or so for both polarizations. It can be clearly seen that, the absorptance of the double-sized metamaterial absorber is insensitive to the incidence angle, and high absorptance exists over a large range of incidence angles for both polarizations.

We have demonstrated that, by using two tungsten patches at different sizes, the absorptance of the metamaterial absorber could be further enhanced in a broader spectral region compared to the single-sized ones. Is that possible to further broaden the band with enhanced absorptance by multiple-sized patches? Figure 3.10 shows the spectral absorptance at normal incidence for multiple-sized metamaterials with three or four different patch sizes, in comparison to that of double-sized metamaterial absorber. The

patch width values are w_1 = 250 nm, w_2 = 300 nm, w_3 = 350 nm for the 3 by 3 patch array, and w_1 = 250 nm, w_2 = 300 nm, w_3 = 350 nm, and w_4 = 400 nm for the 4 by 4 patch array. The patches are arranged in a 3 by 3 or 4 by 4 array to be diagonally symmetric. Clearly, with additional larger patch sizes, the high-absorptance band can be further broadened to longer wavelength compared to that of the double-sized metamaterial. This is because the MP resonance wavelength increases with strip width, and additional MPs can be excited at the longer wavelengths with larger patches. However, the absorptance values starts to decrease. This can be explained by the fact that, with more patch sizes, the filling fraction of each patch size becomes less, which leads to less confined solar energy when MP is excited under each patch. As a result, there exists a trade-off between broadening absorption band and achieving high absorption values when more patch sizes are used to design the metamaterial absorbers

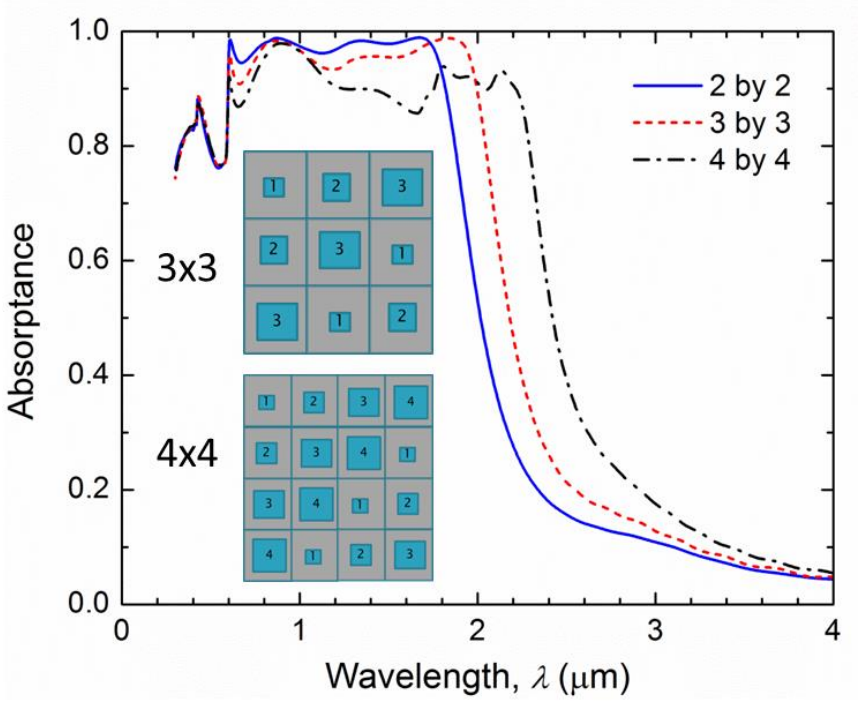

Figure 3.10 The spectral absorptance for multi-sized metamaterial absorber with 3 by 3 and 4 by 4 grating arrays.

In this section, we have numerically designed selective solar absorbers made of metamaterial nanostructures consisting of periodic tungsten square patches on a SiO_2 thin film and a tungsten thin film. High absorptance in the visible and near-infrared region and low emittance in the mid-infrared can be achieved at normal incidence from the single-sized metamaterial absorbers. The physical mechanisms responsible for the high absorption include the excitations of SPP, MP and CMP modes as well as the intrinsic bandgap absorption of tungsten have been elucidated in detail along with the geometric effects on the absorptance spectra. The absorptance can be further enhanced to be close-to-unity for single-sized metamaterial solar absorbers with optimized geometric parameters such as grating height or spacer thickness, and in a broader spectral region with double-sized metamaterial absorbers. The spectral absorptance of the designed double-sized metamaterial absorber is higher than 0.95 in the wavelength region from 0.6 μm to 1.8 μm, while the spectral emittance is lower than 0.04 from 4 μm to 20 μm in the mid-infrared. As a result, the total solar absorptance of the metamaterial absorbers could be more than 88% at normal incidence, while the total normal emittance is around 3% at the absorber temperature of 100°C, suggesting the excellent performance as selective solar absorbers. In addition, the effects of incidence angle and polarization angle have been studied and the results show the direction-insensitive and polarization-independent behaviors of the designed metamaterial solar absorbers. The multi-size effect on the absorptance of the metamaterial absorbers is also investigated, and a trade-off between high absorptance and broad absorption band with multiple patch sizes is identified. The design of perfect metamaterial solar absorbers here would be beneficial to enhance the performance of solar energy harvesting and conversion systems.

3.2.2 Fabrication of the Metamaterial Solar Absorber

In this section, we report on the spectroscopic characterization at both room and elevated temperatures of a selective metamaterial solar absorber made of a 2D titanium grating deposited on an MgF_2 spacer and an opaque tungsten film, as illustrated in Fig. 3.11(a). Tungsten is chosen as the substrate material due to its excellent high-temperature stability, while titanium is selected for the gratings as it is easier to pattern with lift-off process than tungsten.

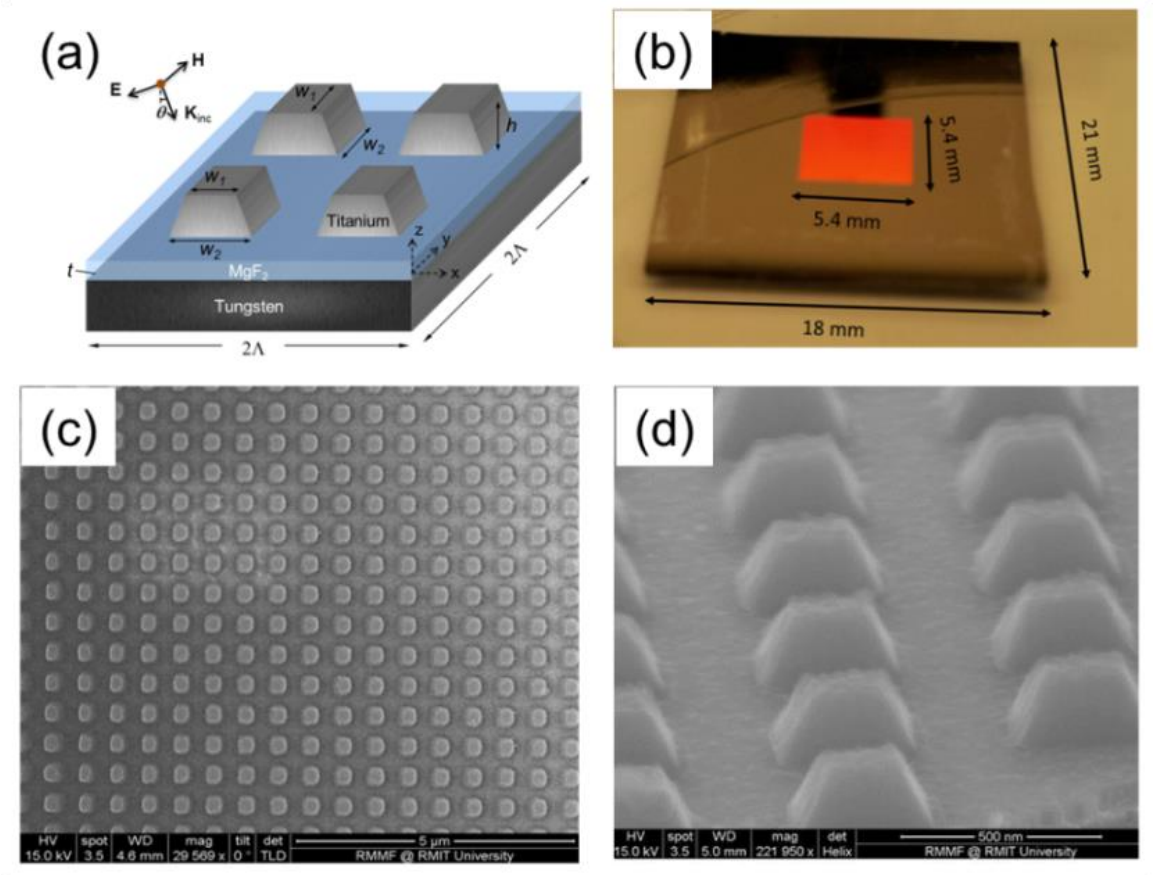

Figure 3.11 (a) Structure schematic for proposed metamaterial solar absorber. (b) A photo of the fabricated sample for optical characterization. SEM images of the fabricated absorber sample from (c) top view and (d) side view.

The selective metamaterial solar absorber is fabricated with the following procedure. First, MgF_2 and tungsten thin films were deposited using e-beam evaporation (Kurt J. Lesker PVD 75) on a silicon substrate. Then, the 2D titanium gratings with period of 600 nm were fabricated onto the MgF_2/W coated Si substrate using electron beam lithography by a multi-step exposure scheme on a FEI Nova Nano SEM with NPGS (J. C. Nabity Lithography Systems, Nanometer Pattern Generation System), followed by e-beam evaporation and lift-off process. Figure 3.11 (b) shows the photo of the fabricated metamaterial solar absorber sample with a 5.4 mm by 5.4 mm pattern area on a 21 mm by 18 mm Si wafer. The fabricated grating patterns at the top layer of the metamaterial solar absorber have excellent symmetry in x and y direction as seen from the top-view SEM image in Figure 3.11 (c), while a trapezoid shape is observed from the side-view SEM image in Figure 3.11 (d), which is typical for metallic gratings patterned from a lift-off process with negative photoresist. The measured geometric parameters are: grating period Λ = 600 nm, grating top width w_1 = 200 nm, bottom width w_2 = 360 nm, grating height h = 170 nm, and MgF_2 spacer thickness t = 50 nm. The tungsten layer has a thickness of 200 nm, which is opaque within the spectral region of interests.

3.2.3 Optical Characterization of the Metamaterial Solar Absorber

The specular reflectance R'_λ of the fabricated solar absorber was measured by the Fourier Transform Infrared (FTIR) spectrometer (Thermo Fisher, iS50) along with a variable-angle reflectance accessory (Harrick Scientific, Seagull) at an incidence angle of 8° from 0.4 to 20 μm in wavelength with a spectral resolution of 4 cm^{-1} in wavenumber. Due to the excellent geometric symmetry in x and y directions of the sample, the

spectrometric measurement was performed with unpolarized waves as the radiative properties have negligible polarization-dependence at near-normal direction. The reflectance from 0.4 to 1.1 μm in wavelength was measured by an internal Si detector, while a DTGS detector was employed at longer wavelengths beyond 1.1 μm. An aluminum mirror was used as the reference and the measured reflectance is normalized based on the theoretical reflectance of aluminum. The measured reflectance was averaged over three measurements (each with 32 scans) by interchanging the sample and reference to reduce the occasional errors during the measurement. In order to check the uncertainty of FTIR measurements, the reflectance of a reference Si sample (Virginia Semiconductor, Boron doped with resistivity of 60 ohms-cm) was measured and compared with its theoretical value, showing the measurement uncertainty within 2%.

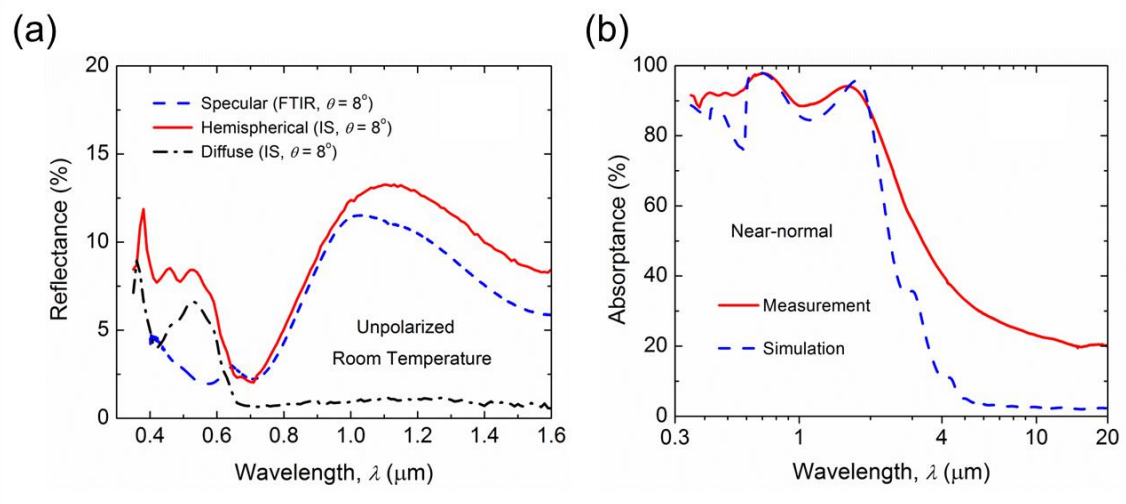

Figure 3.12 (a) Measured room-temperature specular, diffuse, and hemispherical reflectance of the metamaterial solar absorber. (b) Measured and simulated room-temperature spectral absorptance of the metamaterial solar absorber.

The directional-hemispherical reflectance $R'^{\cap}_{\lambda}$ and diffuse reflectance were measured in a custom-built 8-inch integrating sphere (Labsphere, IS) at an incidence

angle of 8°. An unpolarized monochromatic light from UV to NIR (i.e., 0.35 μm to 1.6 μm in wavelength) was provided by the tunable light source (Newport, TLS-250Q) with a spectral resolution of 10 nm. The light signal was modulated with an optical chopper and obtained with a commercial Si detector (Thorlabs, SM05PD1A) and an InGaAs detector (Thorlabs, SM05PD5A) after lock-in amplification (Oriol, Merlin). A silver mirror was employed as the reference and the measured reflectance is corrected with the theoretical reflectance of silver. The reflectance was averaged from five individual measurements. The hemispherical reflectance was measured without a light trap, while the diffuse reflectance was characterized with a light trap mounted at the specular direction. The measurement uncertainty from the IS measurement was checked to be within 2% with the same reference Si sample.

Figure 3.12(a) shows the room-temperature specular, diffuse, and hemispherical reflectance measured at different wavelengths with an incidence angle $\theta = 8°$ from both the FTIR and IS measurements. It can be observed that the specular reflectance R'_λ of the metamaterial solar absorber is lower than 5% at 0.35 μm < λ < 0.8 μm, while R'_λ increases to a maximum value of 11% in the NIR range. The low reflectance indicates high absorptance in the solar spectrum, which is desired for highly-efficient solar absorbers.

The results of Figure 3.12(a) also show that the diffuse reflectance is negligible (less than 1%) at wavelengths λ > 650 nm, indicating that the sample is highly specular. This can be explained by the sub-wavelength nature of the metamaterial solar absorber array due to its periodicity. In periodic structures, all the non-zero diffraction orders are evanescent waves in the sub-wavelength region, which do not contribute to the far-field

diffuse reflection. As a result, the hemispherical reflectance $R'^{\cap}_{\lambda}$ from the IS measurement is almost the same as the specular reflectance R'_{λ} from the FTIR measurement at longer wavelengths beyond 650 nm with a small difference less than 2.5%. This highlights the specular behavior of the metamaterial solar absorber when the incident wavelength is larger than the grating period at normal incidence.

On the other hand, when the incident wavelength is smaller than the grating period, the diffuse reflectance becomes significant and increases up to 6.5% around λ = 0.5 μm due to the non-negligible contribution from higher-order diffracted waves. As a result, the difference between hemispherical and specular reflectance becomes larger at short wavelengths due to the increased diffuse reflection. Note that from the IS measurement, the diffuse reflectance starts to become negligible at 650 nm, which is not the same as the grating period Λ = 600 nm. This is because the reflectance is measured at near-normal with θ = 8° (i.e.,) instead of perfectly normal incidence. The small nonzero oblique incidence angle results in $k_{x,\text{inc}} \neq 0$, thereby slightly shifting the cutoff wavelength to λ = 650 nm.

The spectral-directional absorptance of the metamaterial solar absorber is obtained by $\alpha'_{\lambda} = 1 - R'^{\cap}_{\lambda}$ based on the energy balance as the sample is opaque, while the spectral-directional emittance is simply equal to the spectral-directional absorptance according to Kirchhoff's law: $\alpha'_{\lambda} = \varepsilon'_{\lambda}$. As discussed previously, the metamaterial solar absorber is highly specular at wavelengths λ > 650 nm. Thus, the spectral-hemispherical reflectance $R'^{\cap}_{\lambda}$ at λ > 650 nm is obtained as the specular reflectance (i.e., $R'^{\cap}_{\lambda} = R'_{\lambda}$)

from the FTIR measurement at near-normal incidence, while $R'^{\cap}_{\lambda}$ at shorter wavelengths is acquired from the IS measurement. Figure 3.12(b) shows the characterized spectral absorptance/emittance of the fabricated metamaterial solar absorber under near-normal incidence at room temperature. The metamaterial solar absorber shows absorptance higher than 90% within 0.35 μm < λ < 2 μm from the UV to NIR region, and emittance around 20% from 6 μm < λ < 20 μm in the mid-IR. Therefore, the spectral selectivity of the metamaterial solar absorber is clearly demonstrated, which is crucial for improving the performance of solar absorbers by maximizing solar absorption and minimizing self-emission loss.

FDTD simulation was performed to numerically calculate the spectral-normal absorptance/emittance, which shows excellent agreement with the measurement data in Figure 2b. The FDTD simulation was performed with a commercial package (Lumerical, FDTD Solutions). Optical properties of titanium, MgF_2 and tungsten were obtained from Palik's data.[97] The simulation was implemented in a 0.6 μm × 0.6 μm × 4 μm simulation domain, and the wavelength range of interest is from 0.3 μm to 20 μm with a spectral resolution of 5 nm. Manually refined meshes with size of 5 nm in x and y directions and 2 nm in z direction were employed to ensure the numerical convergence. Periodic boundary conditions were applied in x and y directions for normal incidence, while perfect matched layers with reflection coefficient of 10^{-6} were placed in z direction. A plane wave source was placed at 1.2 μm above the structure surface, and the reflectance R was obtained by a frequency-domain power monitor positioned at 0.5 μm above the plane wave source. The spectral absorptance was obtained using $\alpha = 1 - R'^{\cap}_{\lambda}$ as the

structure is opaque due to the 200 nm tungsten substrate. The theoretical and measured reflectance for the solar absorber at normal direction is compared in Fig. 3. 12 (b), which shows a good match between simulation and experiment.

There are two major absorption peaks from the measurement for the metamaterial solar absorber: one at λ = 0.68 μm with amplitude of 97.8% due to surface plasmon polariton (SPP), and the other at λ = 1.6 μm with amplitude of 94.1% due to magnetic polariton (MP). SPP is a surface wave due to the collective oscillation of plasmon excited at the interface of two materials with permittivity of ε_1 and ε_2.

On the other hand, MP is the coupling between the incident electromagnetic wave and magnetic resonance inside the structure. To explain the excitation mechanism of MP, the electromagnetic field distribution at the MP resonance is obtained from the FDTD simulation and plotted in Fig. 3.13. The arrows show the electric field vectors and the contour represents the strength of the magnetic field normalized as $\log_{10}\left|H / H_0\right|^2$, where H_0 is the incident magnetic field. It can be observed that the electric current forms a loop under the Ti patch, while the magnetic field is greatly enhanced in the local area within the current loop with one order of magnitude higher over the incidence. This is a typical electromagnetic field pattern at MP resonance due to the diamagnetic response inside the grating microstructure, and the strong field confinement explains the high absorption at MP resonance.

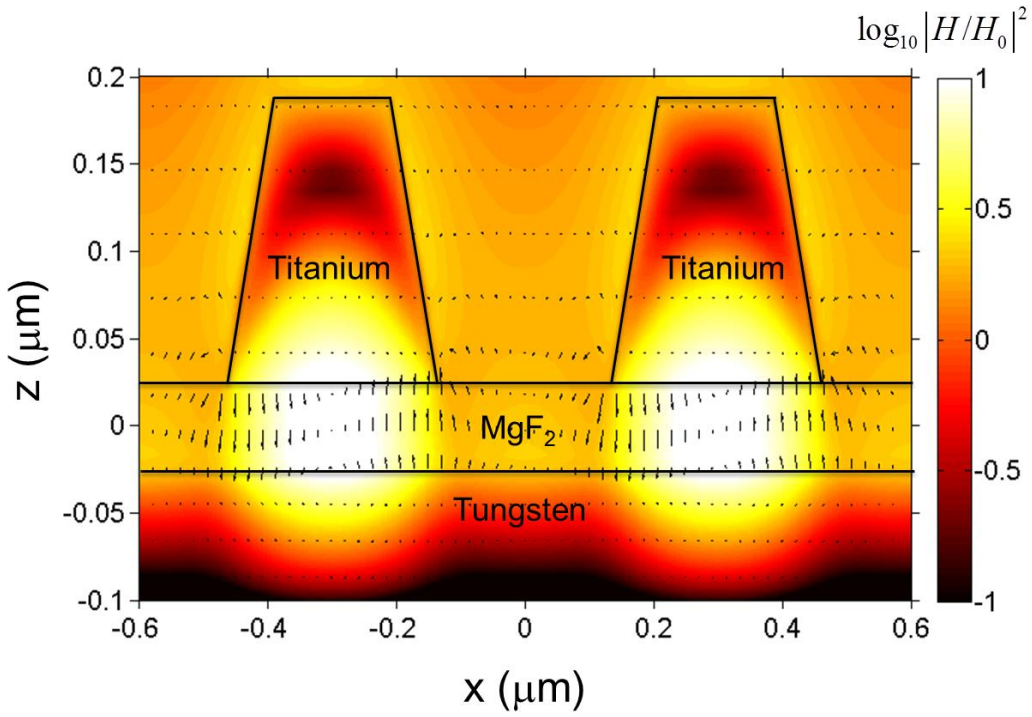

Figure 3.13 Electromagnetic field distribution for the metamaterial absorber at MP resonance.

The measured emittance in the mid infrared is around 20%, which is higher than the 4% predicted from the simulation, possibly due to the oxidation of tungsten and titanium during the sample fabrication process. Note that, the metamaterial solar absorber is essentially highly reflective from the metallic components without any resonance absorption in the long-wavelength region. By addressing the material oxidation issue, it is expected that, the emittance of the metamaterial solar absorber sample can be further reduced to approach the theoretical 4% to better minimize the thermal emission energy loss, thereby further improving the solar thermal conversion performance.

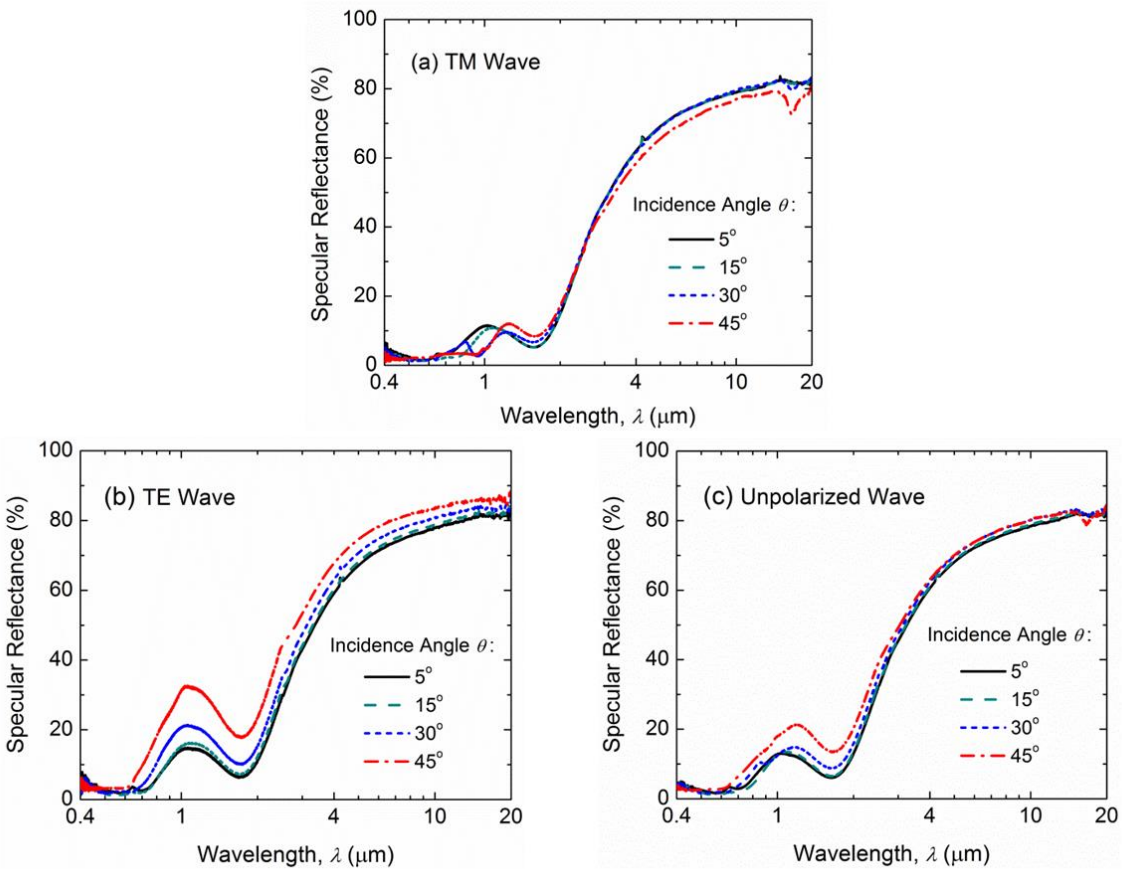

Figure 3.14 Reflectance measured by the FTIR for the metamaterial absorber for (a) TM wave; (b) TE wave; (c) Unpolarized wave.

The optical and radiative properties at oblique angles of a solar absorber are also vital for efficiently harvesting direct sunlight coming from different directions after an optical concentrator. An ideal solar absorber should be diffuse-like with optical and radiative properties independent of direction. Therefore, the specular reflectance of the metamaterial solar absorber was measured by the FTIR spectrometer at several incidence angles θ = 5°, 15°, 30° and 45° with the variable-angle reflectance accessory. The reflectance was measured separately for TM and TE waves with a broadband polarizer

(Thorlabs, WP25M-UB) in visible and NIR regime or the internal wire-grid IR polarizer inside the FTIR.

Figure 3.14(a) plots the measured specular reflectance R'_λ for the metamaterial solar absorber at oblique TM incidence. It can be observed that R'_λ at $\lambda < 0.7$ μm is lower than 5% for all oblique incidences. Moreover, the reflection dip due to the MP excitation at λ = 1.6 μm does not shift with increased incidence angle, thanks to the unique direction-independent characteristic of MP resonance. When the incidence angle increases for TM incidence, the strength of the incident H field parallel to the y-direction grating groove does not change. Thus, the strength of the oscillating current loop for MP does not decrease, and the MP resonance strength remains almost unchanged. As a result, the reflectance at the MP wavelength increases little with larger incidence angle.

Figure 3.14(b) shows the specular reflectance R'_λ of the metamaterial solar absorber at TE oblique incidence. It is found that R'_λ at $\lambda < 0.7$ μm is also lower than 5%. The reflectance at MP resonance increases slightly with larger oblique angles. This is because the strength of incident H field component parallel to the grating groove in y direction decreases as the incidence angle becomes larger for TE waves. As a result, the strength for MP resonance decreases and the absorptance drops. The reflectance at longer wavelengths in the mid-IR also increases slightly at oblique incidences.

Considering the random nature of sunlight, the reflectance for unpolarized waves, which is averaged from both polarizations, is presented in Figure 3.14(c) for different oblique angles. It is observed that when incidence angle θ changes from 5° to 30°, the reflectance for unpolarized incidence barely changes with reflectance lower than 15% in

the visible and NIR region (i.e., 0.4 μm to 2 μm in wavelength). The reflectance slightly increases but remains less than 20% when θ further increases to 45°. The measured optical and radiative properties of the fabricated metamaterial solar absorber sample clearly demonstrate the diffuse-like behaviors at both TM and TE polarizations as well as unpolarized waves.

In order to characterize the optical properties of the metamaterial solar absorber at elevated temperatures, the FTIR fiber optics technique was employed for measuring the temperature-dependent specular reflectance R'_λ from the sample mounted inside a home-designed heater assembly with precise temperature control. The FTIR measurements were performed when the desired temperature was stable at least for 20 min. Note that in the NIR spectral regime, the measured reflectance at each wavelength is averaged from 20 neighboring data points to reduce the fluctuation in measured reflectance caused by the low signal-to-noise ratio from the DTGS detector. A 30-nm-thick SiO_2 layer was deposited onto the sample surface to protect the metamaterial structures from possible oxidation or chemical reaction in air during sample heating, which would change the desired optical properties and degrade the performance of the metamaterial solar absorber at elevated temperatures.

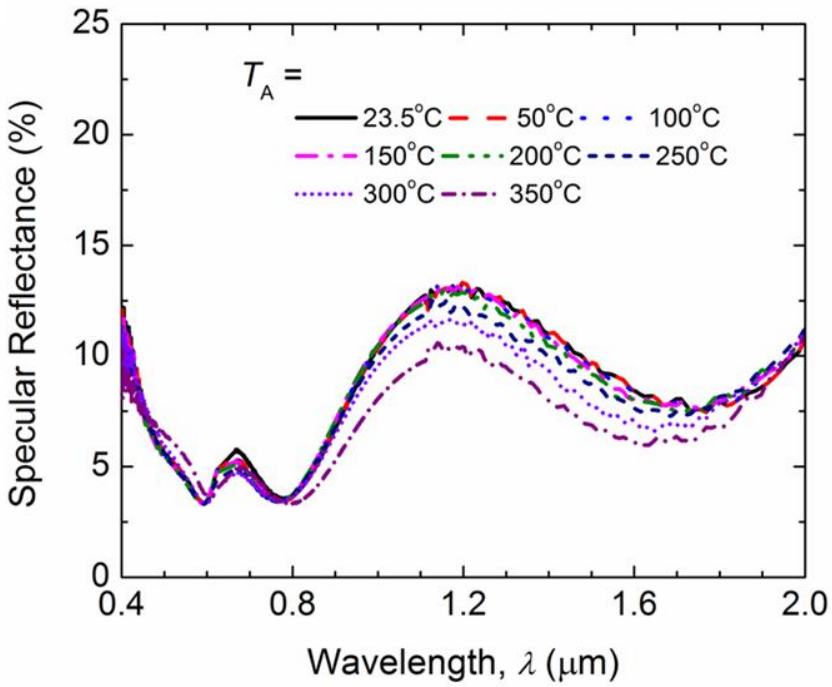

Figure 3.15 Specular reflectance of the metamaterial solar absorber measured at elevated temperatures up to 350°C with temperature-dependent FTIR fiber optics.

Figure 3.15 shows the reflectance for the metamaterial solar absorber when the sample temperature increases from room temperature (23.5°C) to 350°C with an interval of 50°C. It can be seen that the reflectance at wavelengths from 0.4 μm to 0.8 μm barely changes with increased absorber temperature, indicating excellent thermal stability of the fabricated metamaterial solar absorber. The reflectance from 0.8 μm < λ < 2 μm decreases with higher temperatures, which might be due to materials chemical changes. Nevertheless, the slight variation of the reflectance is only within 2.5%, and decreased NIR reflectance at higher temperature is actually beneficial for absorbing more solar energy.

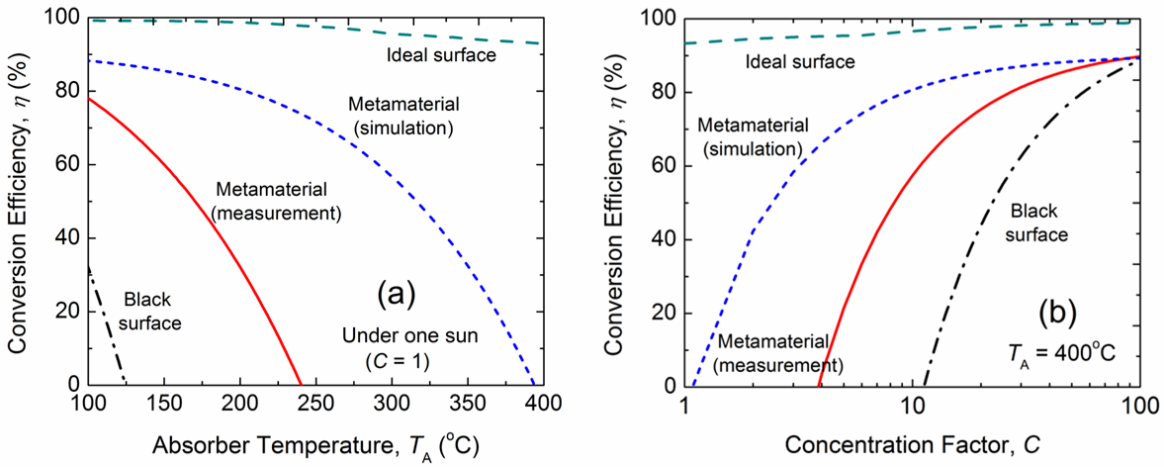

Figure 3.16 (a) Predicted solar-to-heat conversion efficiencies of an ideal selective surface, the metamaterial solar absorber (with optical properties either measured or simulated), and a black surface as a function of absorber temperature T_A under 1 sun. (b) Solar-to-heat conversion efficiency for all three surfaces as a function of concentration factor C at an absorber temperature of T_A = 400°C.

In order to evaluate the performance of the metamaterial as a potential highly-efficient solar thermal absorber, the solar-to-heat conversion efficiency is theoretically analyzed. Assuming no conduction or convection losses, the conversion efficiency of a solar absorber can be calculated by:

$$\eta = \frac{\alpha_{\text{Total,N}} CG - \varepsilon_{\text{Total,N}} (\sigma T_A^4 - \sigma T_{\text{sky}}^4)}{CG} \tag{3.5}$$

where C is the concentration factor, G is the heat flux of incident solar irradiation at AM1.5 (global tilt) [96], T_A is the absorber temperature, and T_{sky} = 20°C is the sky temperature. $\alpha_{\text{Total,N}}$ and $\varepsilon_{\text{Total,N}}$ are respectively the total normal absorptance and emittance for the solar absorber, which can be respectively calculated by:

$$\alpha_{\text{Total,N}} = \int_0^\infty \alpha'_{\lambda,\text{N}} I_{\text{AM1.5}}(\lambda) d\lambda \Big/ \int_0^\infty I_{\text{AM1.5}}(\lambda) d\lambda \tag{3.6}$$

$$\varepsilon_{\text{Total,N}} = \int_0^\infty \varepsilon'_{\lambda,N} I_{\text{BB}}(\lambda, T_{\text{A}}) d\lambda \Big/ \int_0^\infty I_{\text{BB}}(\lambda, T_{\text{A}}) d\lambda \tag{3.7}$$

where $I_{\text{AM1.5}}(\lambda)$ is the spectral intensity of solar irradiation at AM1.5 (global tilt), $I_{\text{BB}}(\lambda, T_{\text{A}})$ is the spectral blackbody radiative intensity at the solar absorber temperature T_{A}, and $\alpha'_{\lambda,N}$ and $\varepsilon'_{\lambda,N}$ are respectively the spectral normal absorptance and emittance of the solar absorber measured at room temperature. Note that both $\alpha'_{\lambda,N}$ and $\varepsilon'_{\lambda,N}$ are taken to be independent on temperature as observed from the temperature-dependent optical characterization. For the calculation of total absorptance, the spectral integration is limited to the wavelength region from 0.35 μm to 4 μm, because our instrument cannot measure optical properties at wavelengths below 0.35 μm while the available AM1.5 data only covers wavelengths up to 4 μm. There is still around 7% of solar radiation outside of this spectral range mainly in the UV regime. Similarly, the spectral integration for total emittance is performed in the wavelengths from 0.35 μm to 20 μm limited by the available measurement data. Note that, there is only 4% energy outside this spectral regime mainly in the far-infrared for a blackbody with a temperature of 400°C. Since the metamaterial solar absorber is quite diffuse with oblique angles θ < 45° from the directional optical property characterization, the total hemispherical absorptance or emittance can be reasonably approximated by the total normal absorptance or emittance.

Figure 3.16 (a) plots the conversion efficiency η as a function of absorber temperature T_{A} under 1 sun (i.e., no optical concentration) for an ideal selective surface, the metamaterial solar absorber with optical and radiative properties taken from either measurements or the FDTD simulation, and a black surface. The absorptance for the ideal surface is unity below the cutoff wavelength to maximize absorbed solar radiation, while

its emittance is zero beyond the cutoff wavelength to minimize spontaneous thermal emission loss. The cutoff wavelength for the ideal selective solar absorber is optimized at each absorber temperature for maximal conversion efficiency, which represents the upper limit. On the other hand, the black surface has unity absorptance and emittance in the entire spectral regime (i.e., $\varepsilon = \alpha = 1$), whose conversion efficiency indicates the lowest limit.

It is observed that the conversion efficiency for the metamaterial solar absorber with measured optical properties could reach 78.1% at the absorber temperature T_A = 100˚C and monotonically drops to zero at the stagnation temperature of 241˚C, at which no solar thermal energy is harvested. The efficiency for the metamaterial absorber with simulated optical properties shows relatively higher values. Theoretically, the proposed metamaterial absorber could have a conversion efficiency as high as 88.3% at T_A = 100˚C and a much higher stagnation temperature of 393˚C. The discrepancy on the efficiency results from larger emittance in the mid-IR region from the measurement than simulation. The performance of the fabricated metamaterial absorber can be further improved to approach the theoretical values after the oxidation issues during the sample fabrication are addressed.

In comparison, a black surface could only convert about 32% of solar energy to useful heat at T_A = 100˚C, while its efficiency drops quickly to zero at 125˚C, suggesting the great importance of spectral selectivity in enhancing the solar-to-heat conversion efficiency. On the other hand, the efficiency of the metamaterial absorber is about 10% (with simulated optical properties) or 20% (with measured data) less than the ideal surface at T_A = 100˚C, mainly due to the larger emittance in the mid-IR around 4%

(simulated) and 20% (measured). The absorptance within solar spectrum of the metamaterial is also smaller than the ideal by 5% to 10%, but at low optical concentrations, the self-emission loss determined by the mid-IR emittance plays a major role in determining the amount of harvested solar energy. The difference between the metamaterial absorber and the ideal surface becomes even larger when temperature goes up as the ideal surface maintains high efficiencies of 98.7% at 200˚C, and 93% at 400˚C. This is because the cut-off wavelength of the ideal surface is optimized at each temperature, as the blackbody spectrum governed by the Planck's law would shift towards shorter wavelengths with higher absorber temperature. On the other hand, the cut-off wavelength for the metamaterial absorber is around λ = 2 μm or so and does not change with absorber temperature. In fact, the cut-off wavelength of the metamaterial absorber is determined by the MP resonance wavelength, which can be easily tuned with geometric parameters such as grating width. Therefore, for a given absorber temperature required by a particular solar thermal system, the cut-off wavelength as well as the absorptance/emittance spectrum can be optimized during the design and fabrication processes for achieving maximal solar-to-heat conversion efficiency.

It is known that with concentrated sunlight, the solar-to-heat conversion efficiency can be further improved. Here, we consider the effect of concentration factor *C* from 1 to 50 at an absorber temperature T_A = 400˚C for a medium-temperature application. Note that the thermal energy at 400˚C carries quite amount of exergy, and could potentially deliver electricity with heat engines in Rankin cycle or solid-state devices such as thermoelectrics and TPV besides heating and cooling applications. Figure 3.16(b) shows that, the metamaterial absorber with measured optical properties could

harvest 21.5 % of solar energy to useful heat under 5 suns, 57.4 % with 10 suns, and 80% with 25 suns. For the metamaterial absorber with even lower IR emittance as simulated, the efficiency could be as high as 71% under 5 suns and 81% with 10 suns, indicating room for improvement with the current fabricated sample. With more optical concentrations up to 100 suns, the conversion efficiency of the metamaterial absorber (with optical properties both measured and simulated) saturates towards 90%. In comparison, the efficiency of the ideal surface slightly increases from 93% to 98% at the same temperature from 1 sun to 100 suns, while that of a black surface is improved greatly with more optical concentrations from 0% at 11 suns toward 90% with 100 suns, suggesting that the spectral selectivity becomes less important with a factor larger than 100 as thermal emission loss becomes negligible with highly concentrated incident solar radiative flux.

3.3 Fabry-Perot Metafilm Selective Solar Absorber with High Temperature Stability

3.3.1 Theoretical Design and Optimization of the Metafilm Selective Solar Absorber

In this section, we have theoretically designed, optimized as well as experimentally fabricated an ultrathin multilayer selective solar absorber. The specular reflectance was measured by an FTIR spectrometer at both near normal and oblique incidences. The diffuse reflectance was examined by an integrating sphere coupled to a tunable light source. Moreover, the temperature dependent reflectance was measured by a novel FTIR fiber optics setup, investigating the thermal stability for this solar absorber in ambient. The multilayer sample was further characterized with a scanning electron

microscope (SEM) as well as Rutherford backscattering spectroscopy (RBS) to investigate its behavior after being heated at a high temperature in ambient.

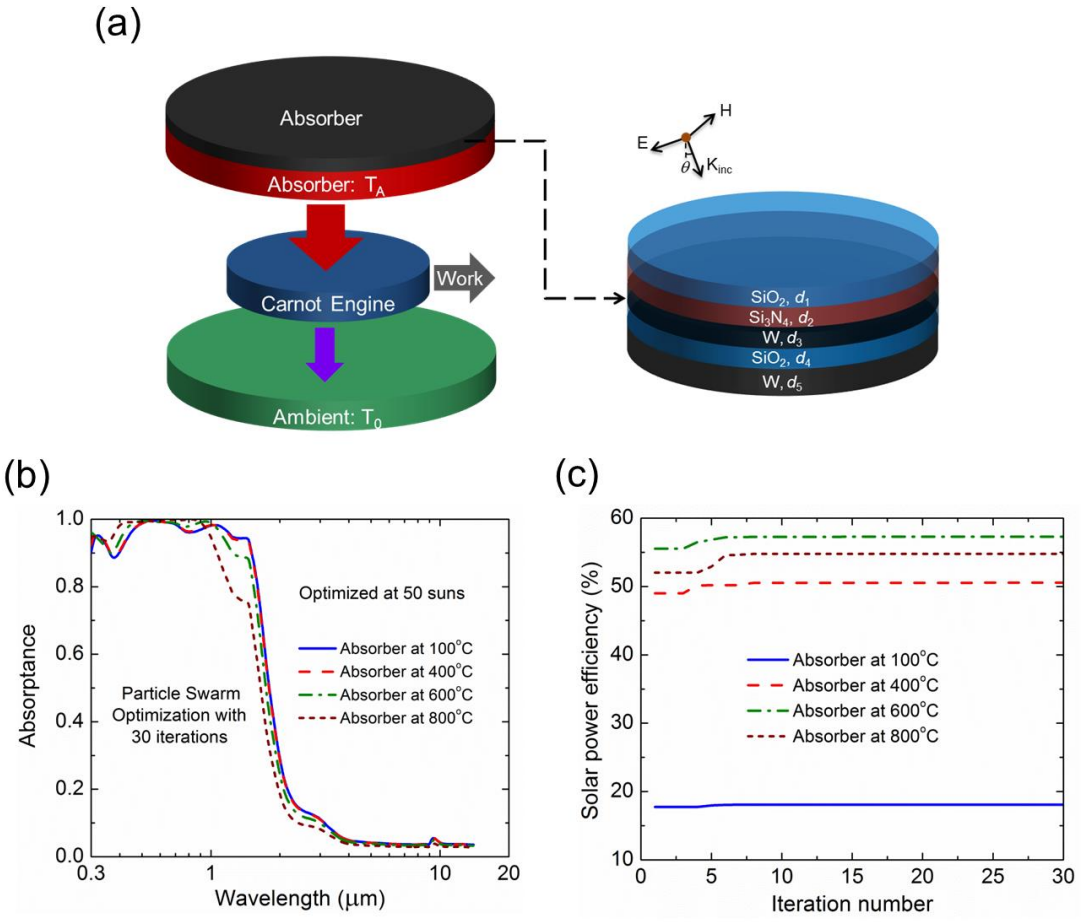

Figure 3.17 (a) Schematic for the metafilm solar absorber; (b) Spectral absorptance for the metafilm absorber optimized at different temperature; (c) Solar power efficiency for the optimized metafilm absorbers.

Figure 3.17 (a) illustrates a solar thermal system, along with a Carnot heat engine. Figure 3.17 (a) also shows the schematic for this selective solar absorber, which is a five layer structure with SiO_2-Si_3N_4-W-SiO_2-W configuration deposited on top of a Si wafer. The W-SiO_2-W stack at the bottom forms a Fabry-Perot cavity [62], which exhibits enhanced absorption at its resonance wavelength. On the other hand, the Si_3N_4 and SiO_2

layers on the top serve as anti-reflection coatings to further reduce the light reflection and enhance the absorption. Tungsten was chosen for two reasons: 1. It is a refractory metal with a high melting point, making it excellent for high-temperature solar thermal absorbers; 2. Tungsten is highly lossy in the visible and NIR spectral regime, which will enhance light absorption in that range. The performance of this selective absorber was optimized by the particle-swarm optimization method [98, 99], with the object function defined as the solar-to-power conversion efficiency, which is calculated by:

$$\eta_{\text{solar-power}} = \eta_{\text{solar-thermal}} * (1 - \frac{T_{\text{bg}}}{T_{\text{A}}}) = \frac{\alpha_{\text{Total,N}} CG - \varepsilon_{\text{Total,N}} (\sigma T_{\text{A}}^4 - \sigma T_{\text{bg}}^4)}{CG} * (1 - \frac{T_{\text{bg}}}{T_{\text{A}}}) \quad (3.8)$$

where $\eta_{\text{solar-thermal}}$ is the solar-to-thermal efficiency, $1 - T_{\text{bg}} / T_{\text{A}}$ is the efficiency of a Carnot heat engine, C is the concentration factor (taken as 50 for this optimization), G is the total solar radiative heat flux at AM 1.5 (global tilt) [96], σ is the Stefan-Boltzmann constant, T_{A} is the absorber temperature, and T_{bg} is the environment temperature (300 K). $\alpha_{\text{Total,N}}$ and $\varepsilon_{\text{Total,N}}$ are respectively the total absorptance and emittance integrated over the entire spectral range:

$$\alpha_{\text{Total}} = \int_0^\infty \alpha'_{\lambda,\text{N}} G_{\text{AM1.5}}(\lambda) d\lambda \Big/ \int_0^\infty G_{\text{AM1.5}}(\lambda) d\lambda \quad (3.9)$$

$$\varepsilon_{\text{Total}} = \int_0^\infty \varepsilon'_{\lambda,N} I_{\text{BB}}(\lambda, T_{\text{A}}) d\lambda \Big/ \int_0^\infty I_{\text{BB}}(\lambda, T_{\text{A}}) d\lambda \quad (3.10)$$

where $G_{\text{AM1.5}}$ is the spectral intensity of solar radiation at AM1.5 (global tilt), $I_{\text{BB}}(\lambda, T_{\text{A}})$ is the spectral blackbody radiative intensity at the solar absorber temperature of T_{A}, $\alpha'_{\lambda,\text{N}}$ and $\varepsilon'_{\lambda,N}$ are respectively the spectral normal absorptance and emittance of the solar

absorber. Note that both α and ε are considered to be independent on the incidence angle here, which will be confirmed later by the optical characterization at oblique incidences for this selective absorber. The integration range is from 0.3 μm to 14 μm for the calculation of α_{Total} and $\varepsilon_{\text{Total}}$ due to limited data for the optical constants obtained from Palik [97], which covers 97% of the solar radiation and 98% of the thermal radiation for an absorber at 1000^{o}C.

Figure 3.17(b) shows the spectral absorptance for the selective solar absorber calculated with the transfer matrix method [35], which was optimized at 50 suns with the absorber temperature of 100^{o}C, 400^{o}C, 600^{o}C and 800^{o}C. It is observed that after 30 iterations, the optimized solar absorbers exhibit excellent spectral selectivity with absorptance larger than 95% in solar spectrum and emittance less than 5% in IR range. It is also noticed that the absorption band blue shifts to shorter wavelength for optimized absorbers at higher temperatures. This is because as the absorber temperature increases, the peak for thermal radiative intensity will blue shift based on Wien's displacement law. Therefore, the absorption band (i.e. emission band) for the solar absorber needs to blue shift as well to suppress the total thermal emittance. Figure 3.17(c) is the solar-to-power conversion efficiency for the optimized solar absorbers at different temperatures. It is observed that the solar-to-power efficiency for solar absorbers reaches the optimum after 30 iterations, with the optimum efficiency of 18.1%, 50.6%, 57.3% and 54.8% for the solar absorbers at 100^{o}C, 400^{o}C, 600^{o}C and 800^{o}C respectively.

3.3.2 Fabrication of the Metafilm Selective Solar Absorber

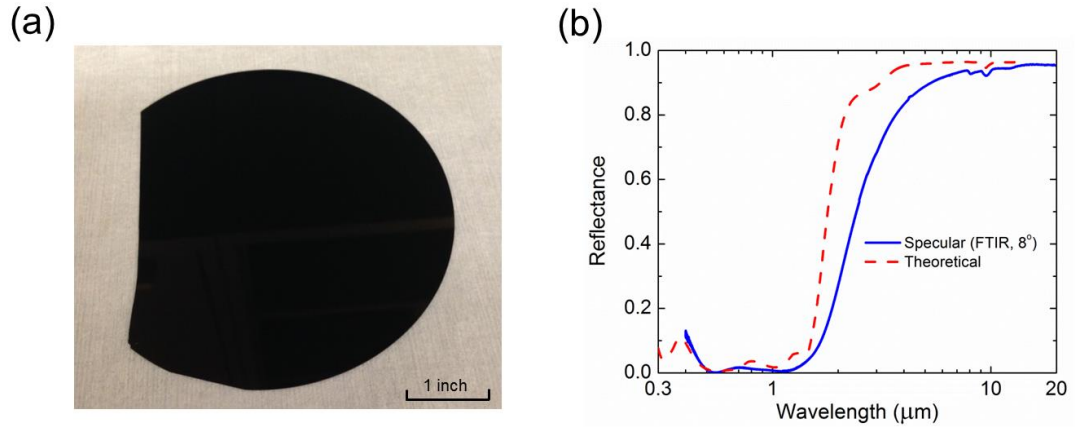

Figure 3.18 (a) A photo of the as fabricated metafilm solar absorber on a 4 inch wafer; (b) Reflectance of the metafilm absorber measured by the FTIR compared with theoretical value.

The solar absorber optimized at 400^{o}C was selected for sample fabrication, with the geometric and fabrication parameters specified in Table 3.1. Note that the entire ultrathin multilayer stack is around 400 nm in thickness. The W-SiO_2-W stack at the bottom was fabricated by sputtering (Lesker, PVD75 Sputter Coater), while the Si_3N_4 and SiO_2 layers on top were deposited with chemical vapor deposition (CVD, ASU Center for Solid State Electronics Research, Plasma Quest). The dielectric layers on top were deposited with CVD so they could exhibit better quality to serve as an oxygen passivation layer under high temperatures [100]. Figure 3.18(a) shows a photo for the multilayer solar absorber fabricated on a 4-inch Si wafer, which appears black due to its high absorptance in the visible spectral regime.

The specular spectral reflectance for the fabricated multilayer structure was characterized with the FTIR spectrometer (Thermo Scientific, iS50) at the incidence angle of 8^{o} with a variable-angle reflectance accessory (Harrick, Seagull). The reflectance

was measured from 0.4 μm to 20 μm with a resolution of 4 cm^{-1} in wavenumber. The measurement was averaged from 32 scans with an Al mirror as the reference, and the measured reflectance was normalized by the theoretical reflectance of Al. Figure 3.18(b) plots the reflectance measured by the FTIR as well as the theoretical reflectance for comparison. A good match between theory and measurement can be observed in the visible and NIR spectral regime, while the measured reflectance is lower from 2 μm to 10 μm, which is most probably due to the impurities and oxidation of the materials. The fabricated sample exhibits reflectance less than 3% from 0.5 μm to 1.2 μm, as well as reflectance higher than 90% in the mid-IR range beyond 5 μm. Note that the multilayer has zero transmission as the 200 nm tungsten layer at the bottom is optically opaque, so the absorptance can be calculated by $\alpha = 1 - R$ based on energy balance. As a result, the fabricated solar absorber is demonstrated to be highly absorbing in the solar spectrum while weakly emitting in the IR range.

Table 3.1. Deposition parameters for different layers in the multilayer selective solar absorber.

Material	Layer thickness (nm)	Deposition method	Deposition rate (Å/s)	Base pressure (10^{-6} Torr)	Sputtering pressure (mTorr)	Sputtering power (W)
W substrate	200	DC Sputtering	1.2	2	1.6	100
SiO_2 cavity	71	DC Sputtering	0.65	2	2	200
W thin film	10	RF Sputtering	0.4	2	2	35
Material	Layer thickness (nm)	Deposition method	Deposition rate (Å/s)	Chamber temperature (^oC)	Chamber wall temperature (^oC)	Reflected RF power (W)
Si_3N_4	50	CVD	~0.7	300	40	~2
SiO_2 top layer	73	CVD	~1.1	300	40	~2

3.3.3 Optical Characterization of the Metafilm Absorber at Room Temperature

In addition to spectral selectivity, an ideal solar absorber should also exhibit consistent performance at various incidence angles to harvest the sunlight incident from arbitrary directions. In order to investigate the angular dependence of optical properties for the selective solar absorber, its specular reflectance was measured at oblique incidence angles with the FTIR. Note that the optical behavior is different for different polarizations at oblique incidences. Therefore, the measurement was performed separately for transverse electric (TE) and transverse magnetic (TM) incidence. TE wave indicates the incident wave with electric field perpendicular to the plane of incidence defined by the incident wavevector and surface normal, while TM wave represents the wave with magnetic field perpendicular to the plane of incidence. The linearly polarized incident wave was obtained with a broadband polarizer (Thorlabs, WP25M-UB) in the visible and NIR regime and the FTIR internal wire-grid polarizer in the IR range.

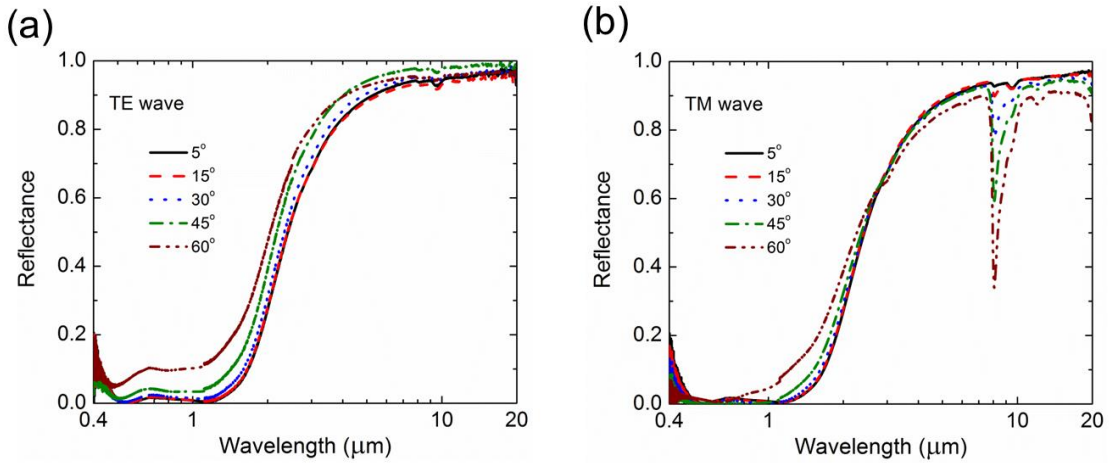

Figure 3.19 Reflectance at oblique incidence of the metafilm absorber for: (a) TE wave; (b) TM wave.

The measured specular reflectance with oblique incidence for both TE and TM polarizations is shown in Fig. 3.19, for incidence angle of 5^o, 15^o, 30^o, 45^o and 60^o. From Figure 3.19(a) which shows the measurement for TE incidence, it can be observed that the reflectance barely changes at incidence angles up to 45^o in the entire wavelength range, but slightly increases up to around 10% at the incidence angle of 60^o in the visible and NIR spectral regime. On the other hand, the reflectance for this selective solar absorber barely changes in the visible and NIR range for TM incidence, but exhibits a reflection dip around 8 μm whose reflectance decreases down to 30% when the incidence angle increases up to 60^o. This reflection dip is due to the excitation of Berreman leaky mode [101, 102] in the phonon band of SiO_2, in which it is lossy due to the strong absorption caused by the lattice vibrations. Note that the Berreman mode can only be excited for TM incidence. To summarize, the optical properties for this multilayer sample are insensitive to the incidence angle at most wavelengths with incidence angle up to 45^o, for both TM and TE polarizations.

3.3.4 Optical Characterization of the Metafilm Absorber at Elevated Temperature

Consistent performance at elevated temperatures is crucially important for solar thermal absorbers, especially for absorbers in CSP systems to maintain their efficient optical performance under concentrated incident solar radiation. In order to characterize the optical properties of the multilayer solar absorber at different temperatures, the fiber optics setup coupled to the FTIR bench was employed for the temperature dependent reflectance measurement. The sample was stabilized at its setpoint for at least 30 minutes

before each measurement. The measurement was performed from 0.45 μm to 18 μm, and the results were averaged from 100 scans with a resolution of 16cm^{-1}.

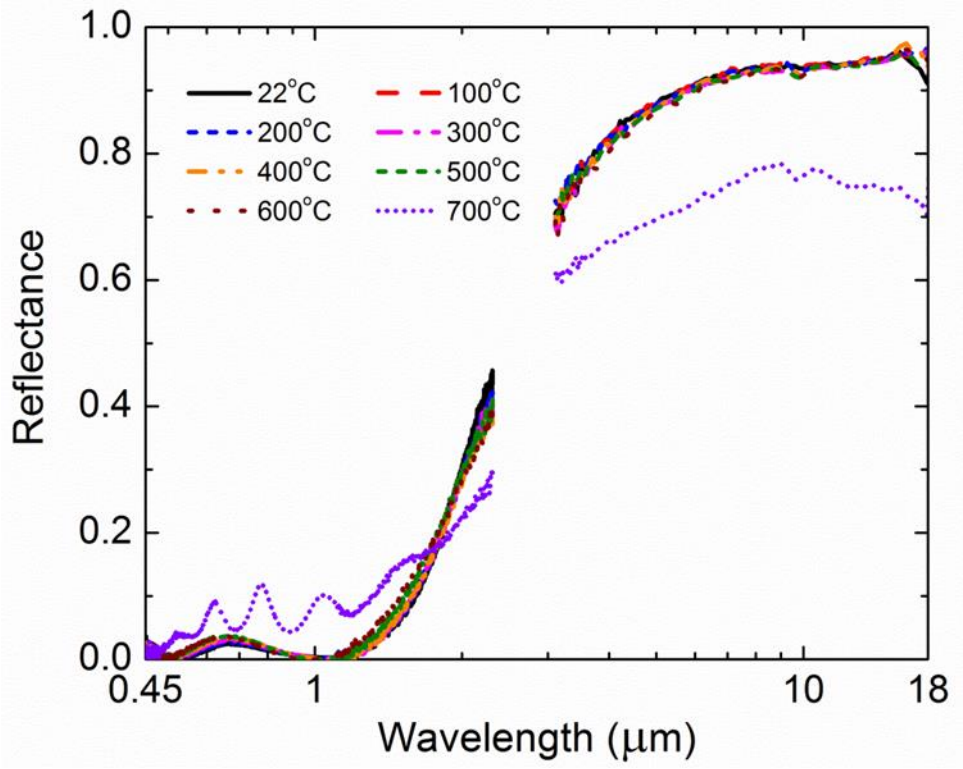

Figure 3.20 Reflectance at elevated temperatures for the metafilm absorber measured by the FTIR fiber optics.

An Al mirror was used to measure the reference signal S_{ref}, and the sample signal S_{sample} was measured as the signal reflected from the sample surface. Note that the noise signal needs to be corrected as the fiber head will directly reflect part of the signal, which is neither reflected by the Al mirror nor the multilayer absorber sample. Therefore, the noise signal S_{noise} was measured with the optical fiber facing the ambient. By correcting the noise signal and normalizing the sample reflectance to the theoretical reflectance of the Al mirror, the sample reflectance can be obtained by:

$$R_{corrected} = \frac{S_{sample} - S_{noise}}{S_{ref} - S_{noise}} * R_{Al} \tag{3.11}$$

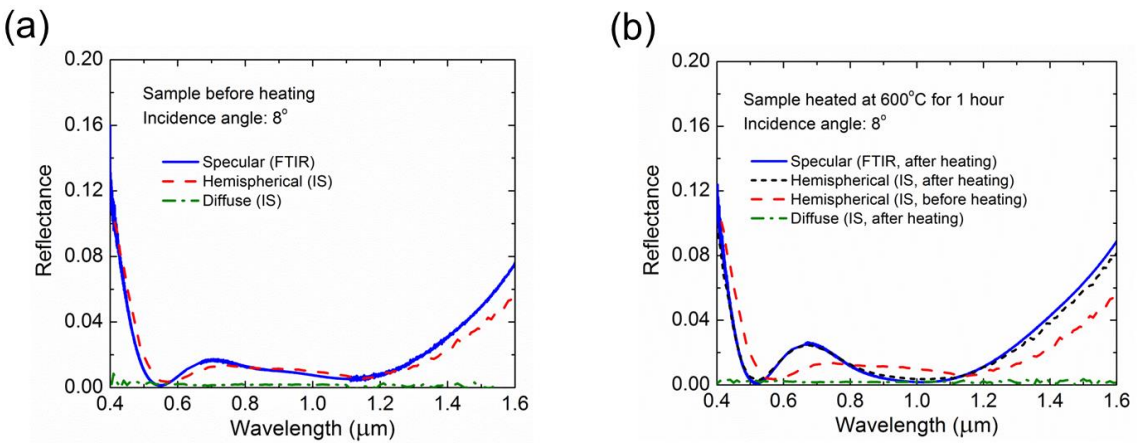

Figure 3.21 Hemispherical and diffuse reflectance measured in the integrating sphere for the metafilm absorber: (a) Before heating; (b) After being heated at 600°C for 1 hour.

Figure 3.20 shows the temperature dependent reflectance for the multilayer absorber measured by the fiber optics setup. It can be seen that the reflectance of the tested sample barely changes from room temperature to 600°C, indicating its excellent high temperature stability up to that temperature. On the other hand, the visible-NIR reflectance starts to increase and the IR reflectance begins to decrease when the temperature further increases up to 700°C. This indicates the instability possibly caused by physical or chemical changes at that temperature. Note that the reflectance from 2.3 μm to 3.1 μm is not plotted, due to a poor signal to noise ratio in that wavelength range which is outside of the transmission band for both the vis-NIR and IR optical fiber.

In previous sections, only the specular reflectance is measured for the multilayer absorber. However, the diffuse reflectance might be significant for the absorber sample, especially when it has been heated up in ambient under high temperatures. The hemispherical and diffuse reflectance was measured for the multilayer absorber sample both before and after being heated at 600°C for an hour in ambient. Figure 3.21(a) shows

the measurement results for the sample before heating. It can be found that the diffuse reflectance is negligible, indicating excellent specularity for this multilayer absorber, which is reasonable for a planar multilayer structure without nano-structures on top. The hemispherical reflectance is also plotted for comparison with the specular reflectance measured by the FTIR. Note that the specular reflectance measured by the FTIR is essentially the hemispherical reflectance as the multilayer absorber is proved to be highly specular. It is observed that the hemispherical reflectance measured by the integrating sphere shows excellent consistency with the specular reflectance measured by the FTIR, with a difference less than 2.5%. This indicates a good agreement between the measurement results from these two setups. In addition, this sample was measured after being heated in a furnace at 600^{o}C for 1 hour in order to examine its specularity after heating. It can be found in Fig. 3.21(b) that the diffuse reflectance is still negligible for the sample after heating, demonstrating that this sample remains highly specular even after being heated at 600^{o}C in ambient for an hour. The hemispherical reflectance is also compared between the multilayer sample before and after heating in Figure 3.21(b), indicating a difference less than 3% for the sample before and after heating, which further confirms the stability of this solar absorber at temperature up to 600^{o}C.

As indicated by Figure 3.21, the optical properties for the multilayer solar absorber are stable at temperature up to 600^{o}C, but would change dramatically at 700^{o}C. In order to figure out the reason causing the instability at 700^{o}C, the sample before and after heating was observed under the SEM. Figures 3.22(a) and (b) show the SEM images for the sample before and after being heated at 600^{o}C for 1 hour, indicating no substantial difference. On the other hand, it is shown in Figure 3.22(c) that when the sample was

further heated at 700°C in ambient for 1 hour, blisters with diameter around 200 μm were formed at the sample surface. There are two possible reasons for the surface blistering: 1. The thermal stress due to the CTE (coefficient of thermal expansion) mismatch between the silicon wafer and tungsten substrate; 2. Outgassing of helium at high temperature, which was trapped inside the multilayer structure during the CVD process. The surface blistering could be potentially avoided by employing materials with better CTE match to reduce the thermal stress or thermal annealing to release the helium from the CVD process.

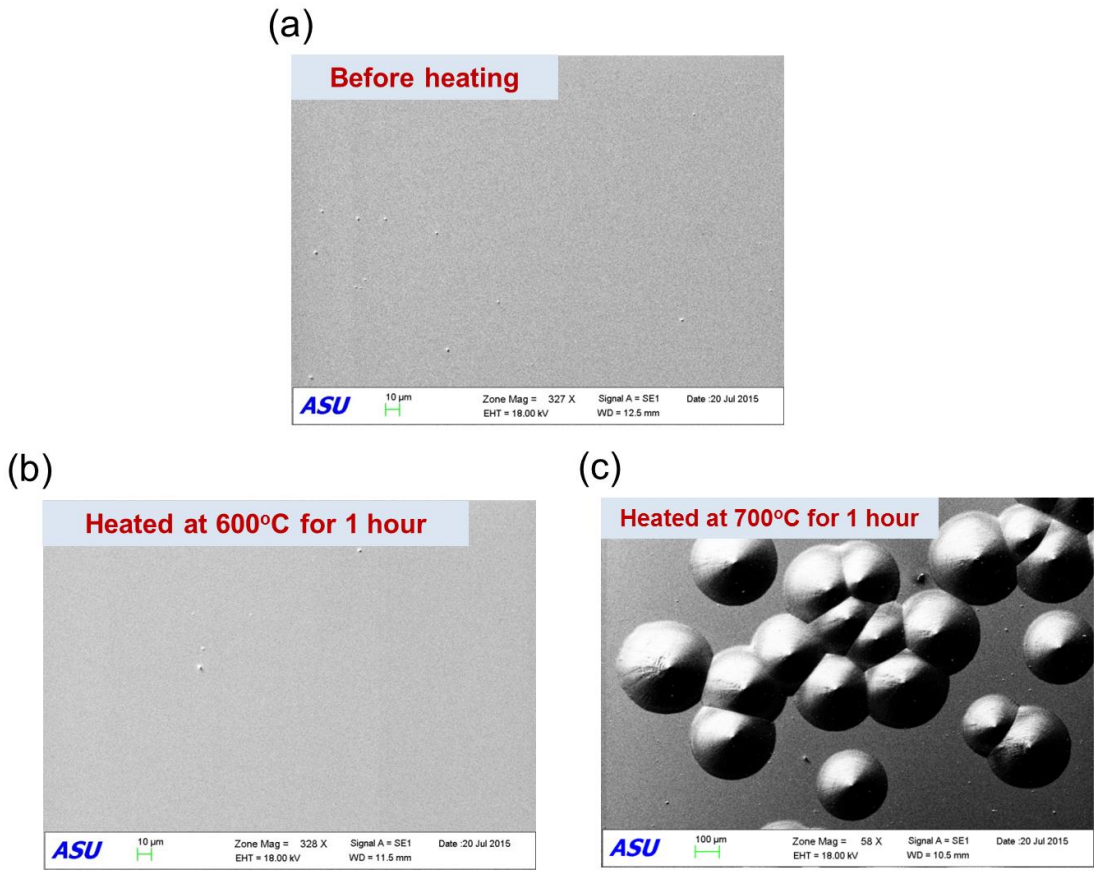

Figure 3.22 SEM images for the metafilm absorber (a) Before heating; (b) After being heated at 600°C for 1 hour; (c) After being heated at 700°C for 1 hour.

Figure 3.23 shows the result for the RBS analysis for the multilayer absorber before and after heating. RBS is a technique that reveals the chemical composition and depth information by impinging an ion beam (helium ions in this case) onto the sample and measuring the back scattering condition of ions. In the graph showing the result from the RBS analysis, each individual peak represents the ions backscattered with a certain energy, which indicates the existence of one particular element at a certain depth. It can be observed from Figure 3.23 that the RBS results for the multilayer sample before and after being heated at 600^{o}C are almost identical, confirming its thermal stability at temperatures up to 600^{o}C. On the other hand, the RBS curve for the sample heated at 700^{o}C shows a significant difference. The peak associated with the tungsten substrate becomes lower, but expands to the lower energy region towards the bottom left. This phenomenon is due to the surface blistering, as when the multilayer blisters up, part of the ions will need to penetrate a longer distance through the tungsten substrate before being scattered. Therefore, these scattered ions exhibit a lower energy due to the higher energy loss while penetrating through a longer distance in the tungsten layer. As a result, less scattered ions exhibit higher energy and the peak associated with tungsten substrate will be lower on the high energy end. On the other hand, more scattered ions exhibit lower energy and the peak indicating tungsten substrate will expand to lower energy region.

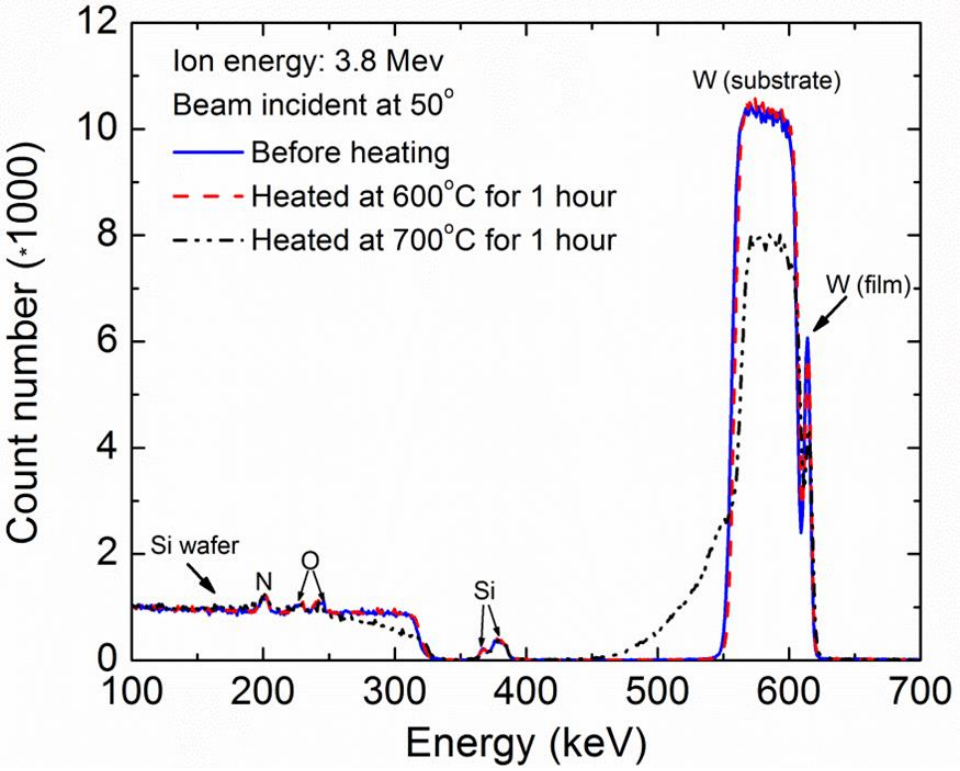

Figure 3.23 RBS diagram for the metafilm absorber before and after being heated at 600°C or 700°Cfor 1 hour.

In order to quantitatively evaluate the performance of the multilayer selective solar absorber, its solar-to-power efficiency was investigated theoretically through Eq. (3.8). Since the multilayer absorber was demonstrated to be diffuse as well as thermally stable up to 600°C, its near-normal room temperature optical properties obtained from the FTIR measurement was employed for the efficiency analysis up to 550°C. Figure 3.24(a) shows the solar-to-power conversion efficiency $\eta_{\text{solar-power}}$ of the ideal, multilayer and black absorber as the absorber temperature varies from 100°C to 800°C. Note that the concentration factor was fixed at 5 and the ambient temperature was considered as 20°C. An ideal absorber has an optimized cutoff wavelength, below which the spectral absorptance is unity, while beyond it the absorptance becomes zero. On the other hand, a

black absorber exhibits unity absorptance over the entire wavelength range. It is observed from Fig. 3.24(a) that the $\eta_{\text{solar-power}}$ for the three absorbers are similar at the absorber temperature of 100°C, which are 21.3% for the ideal absorber, 19.6% for the multilayer absorber and 18.5% for the black absorber, respectively. This is because the thermal re-emission loss is negligible when the absorber temperature is relatively low, hence reducing the thermal re-emission loss via the spectral selectivity of the absorber does not have a big impact on the performance of the absorber. On the other hand, the three different absorbers show remarkably different performance when the absorber temperature is higher, and it is found that the efficiency for the ideal, multilayer and black absorber respectively peaks at 59.1%, 39.38% and 22.1%. The conversion efficiency of the multilayer absorber drops to zero at the temperature of 550°C, indicating no solar energy converted by the absorber. On the other hand, the stagnation temperature for the black absorber is much lower at 280°C. Nevertheless, the conversion efficiency of the ideal absorber is still as high as 56% when the temperature reaches 800°C. This demonstrates the importance of spectral selectivity in improving the performance of solar thermal absorbers.

Figure 3.24(b) shows the solar-to-power conversion efficiency for the three types of absorber when the concentration factor varies from 1 to 100. In this analysis, the absorber temperature was considered as 400°C and the ambient temperature was taken as 20°C. It can be observed that the solar-to-power conversion efficiency increases with a higher concentration factor, since the energy loss through thermal re-emission will be relatively smaller when compared with a larger input solar radiation. It is also found that the difference between the efficiency of the three absorbers is larger at smaller

concentration factors, which becomes less significant as the concentration factor increases. This is because spectral selectivity is less important at larger concentration factors when the thermal re-emission loss becomes negligible. It is observed that the multilayer absorber could convert 40% of solar radiation into power under 5 suns, and this number increases to 42% under 10 suns and 51% under 100 suns. The multilayer absorber converts no solar energy when the concentration factor is below 1.6 suns. In comparison, the black absorber's solar-to-power efficiency is below zero when the concentration factor is less than 10.5 suns. In summary, the multilayer shows much better performance than the black surface, but there is still room for improvement to approach to the performance of the ideal absorber.

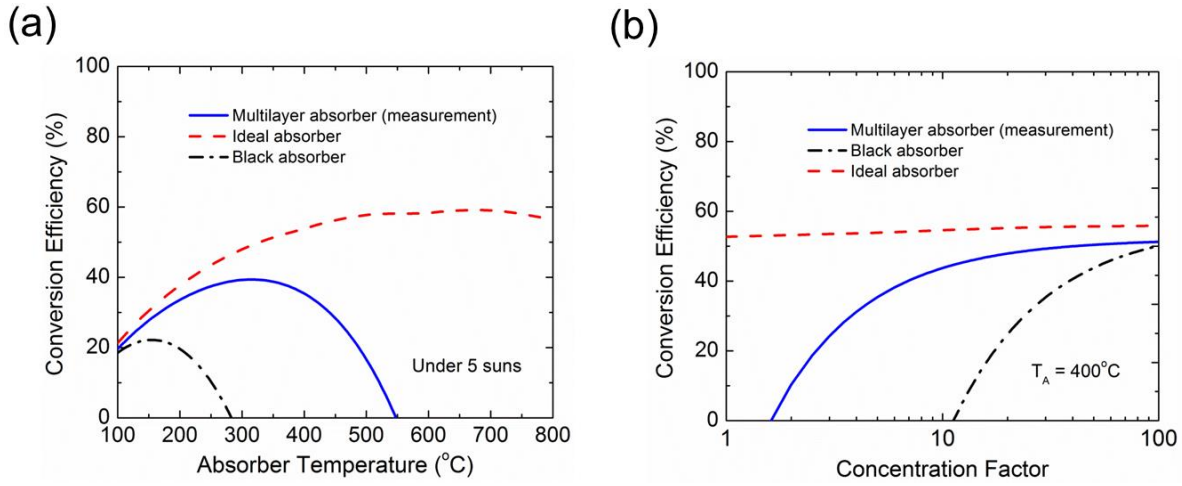

Figure 3.24 Solar to power efficiency for the metafilm absorber with different: (a) Absorber temperatures; (b) Concentration factors.

CHAPTER 4

SOLAR THERMOPHOTOVOLTAIC AND THERMOPHOTOVOLTAIC CONVERSION ENHANCED BY METAMATERIAL AND METAFILM ABSORBERS AND EMITTERS

Different from photovoltaic systems, solar thermophotovoltaic (STPV) systems have an intermediate absorber/emitter module which absorbs broadband solar radiation and emits narrow band thermal radiation that matches with the bandgap of TPV cell. Therefore the conversion efficiency for STPV systems could be potentially much enhanced. One of the main factors that limit the efficiency of STPV systems is the non-ideal absorber and emitter which do not exhibit perfect radiative properties to tailor the broadband solar radiation into narrow band thermal emission. In this chapter, metamaterial based selective absorber and emitter are discussed for enhancing the conversion efficiency of STPV systems. In this chapter, the theoretical analysis for STPV systems employing metamaterial absorber and emitter is discussed in Section 4.1, while the experimental work about TPV system is introduced in Section 4.2.

4.1 Theoretical Analysis on STPV Systems Enhanced by Metamaterial Absorbers/Emitters

4.1.1 Theoretical Analysis for STPV System Employing Ideal Absorber/Emitter and Actual TPV Cells

Figure 4.1 shows the energy balance in an STPV system: the incident solar radiation is converted into heat by the solar absorber, with part of the energy dissipated

through reflection and thermal re-emission; the emitter is then heated up and emits thermal radiation towards the TPV cell, which in turn generates electricity. Note that the temperature of the absorber and emitter is associated with the incident solar radiation and their radiative properties. Neglecting the temperature difference between the absorber and emitter (i.e., $T_{\text{abs}} = T_{\text{emit}}$) as well as the conduction and convection losses, the energy balance at steady state for the absorber-emitter module yields:

$$A_{\text{abs}}(q_{\text{in}} - q_{\text{ref}} - q_{\text{re-emit}} - q_{\text{abs,side}}) = A_{\text{emit}}(q_{\text{E-PV}} + q_{\text{envi}}) \tag{4.1}$$

where A_{abs} and A_{emit} are respectively the top surface area of the solar absorber and the bottom surface area of the TPV emitter. q_{in} is the incident solar radiative heat flux, q_{ref} is the reflected solar radiative flux from the absorber, and $q_{\text{re-emit}}$ is the heat flux through thermal re-emission from the solar absorber surface. $q_{\text{abs,side}} = \sigma\varepsilon_{\text{abs,side}}(T_{\text{abs}}^4 - T_{\text{bg}}^4)A_{\text{abs,side}} / A_{\text{abs}}$ represents the thermal emission loss from the sidewall of the solar absorber normalized to the absorber's top surface area, where σ is the Stefan-Boltzmann constant, $\varepsilon_{\text{abs,side}}$ is the emittance of the absorber sidewall, and $A_{\text{abs,side}}$ is the sidewall surface area for the absorber.

On the other hand, q_{envi} represents the radiative energy flux from the TPV emitter to the environment (from top, bottom and sidewall surfaces) normalized to its bottom surface area, and $q_{\text{E-PV}}$ is the radiative heat flux from the emitter to the TPV cell. Assuming that the radiative properties for the absorber and emitter are independent of

direction (i.e., diffuse surfaces), q_{ref} , $q_{\text{re-emit}}$, $q_{\text{E-PV}}$, and q_{envi} can be respectively calculated by:

$$q_{\text{ref}} = \int_{0.3\mu\text{m}}^{4\mu\text{m}} [1-\alpha_{\text{abs}}(\lambda)] G_{\text{AM1.5}}(\lambda) d\lambda \tag{4.2}$$

$$q_{\text{re-emit}} = \int_{1\mu\text{m}}^{20\mu\text{m}} \varepsilon_{\text{abs}}(\lambda) [E_{\text{bb}}(\lambda, T_{\text{abs}}) - E_{\text{bb}}(\lambda, T_{\text{bg}})] d\lambda \tag{4.3}$$

$$q_{\text{E-PV}} = \int_{1\mu\text{m}}^{20\mu\text{m}} q_{\lambda,\text{ E-PV}} d\lambda = \int_{1\mu\text{m}}^{20\mu\text{m}} \frac{\left[E_{\text{bb}}(\lambda, T_{\text{emit}}) - E_{\text{bb}}(\lambda, T_{\text{cell}})\right]}{R_{\text{emit,cell}}} d\lambda \tag{4.4}$$

$$q_{\text{envi}} = q_{\text{emit,bottom}} + q_{\text{emit, side}} + q_{\text{emit,top}} \tag{4.5}$$

In Eqs. (4.2-4.4), $\alpha_{\text{abs}}(\lambda)$ and $\varepsilon_{\text{abs}}(\lambda)$ are respectively the spectral absorptance and emittance of the absorber which are identical according to Kirchhoff's law, $G_{\text{AM1.5}}$ represents the solar radiative heat flux at air mass 1.5 (AM1.5) [96], $E_{\text{bb}}(\lambda, T)$ is the spectral blackbody emissive power at the temperature of T, T_{abs} is the absorber temperature, T_{bg} is the background temperature (considered as 20 °C), T_{emit} is temperature of the emitter, and T_{cell} is the cell temperature (considered as 20 °C). $R_{\text{emit,cell}} = \frac{1-\varepsilon_{\text{emit}}(\lambda)}{\varepsilon_{\text{emit}}(\lambda)} + \frac{1}{F} + \frac{1-\varepsilon_{\text{cell}}(\lambda)}{\varepsilon_{\text{cell}}(\lambda)}$ is the radiative resistance between the TPV emitter and cell, where $\varepsilon_{\text{emit}}(\lambda)$ is the spectral emittance of the emitter, $\varepsilon_{\text{cell}}$ is the emittance of the InGaAsSb TPV cell, and F is the view factor between the TPV emitter and cell. Assuming that the emitter and TPV cell are both square-shaped with the same length of L and separated by a distance d, the view factor F can be calculated as [103]:

$$F = \frac{1}{\pi r^2}\left(\ln\frac{x^4}{1+2r^2} + 4ry\right) \tag{4.6}$$

where $r = L/d$, $x = \sqrt{1+r^2}$, and $y = x\tan^{-1}\left(\frac{r}{x}\right) - \tan^{-1}(r)$.

In Eq. (4.5), q_{envi} which represents the energy flux lost to the environment consists of three modes. The first term $q_{\text{emit,bottom}} = \int_{1\mu\text{m}}^{20\mu\text{m}} (E_{\text{bb}}(\lambda, T_{\text{emit}}) - E_{\text{bb}}(\lambda, T_{\text{bg}}))d\lambda / R_{\text{emit,bottom}}$ is the radiative heat flux from the TPV emitter to the environment due to the non-unity view factor between the emitter and cell. $R_{\text{emit,bottom}} = \frac{1-\varepsilon_{\text{emit}}(\lambda)}{\varepsilon_{\text{emit}}(\lambda)} + \frac{1}{1-F}$ represents the radiative resistance between the TPV emitter and background environment from the bottom side of the TPV emitter. The second term $q_{\text{emit,side}} = \sigma\varepsilon_{\text{emit,side}}(T_{\text{emit}}^4 - T_{\text{bg}}^4)A_{\text{emit,side}} / A_{\text{emit}}$ is the radiative heat flux through the sidewall of the emitter normalized to the bottom surface area of the emitter, in which $\varepsilon_{\text{emit,side}}$ and $A_{\text{emit,side}}$ are respectively the emittance and surface area of the emitter sidewall. The third term $q_{\text{emit,top}} = \sigma\varepsilon_{\text{emit,top}}(T_{\text{emit}}^4 - T_{\text{bg}}^4)A_{\text{emit,top}} / A_{\text{emit}}$ accounts for the radiative heat flux from the top of the TPV emitter while the absorber area is smaller than the emitter area. $\varepsilon_{\text{emit,top}}$ is the thermal emittance for the top surface of the TPV emitter, and $A_{\text{emit,top}}$ is the area for the top surface of the emitter which is not covered by the absorber. Note that the integration range for the thermal radiative power is from 1 μm to 20 μm in wavelength due to the limited data for the radiative properties of the absorber and emitter, while the considered spectral range contains 98.5% of the thermal radiative energy for a blackbody at temperature of 1000 K. On the other hand, the spectral integration for solar radiation is

from 0.3 μm to 4 μm in wavelength due to the limited AM1.5 data, which covers around 96% of solar energy.

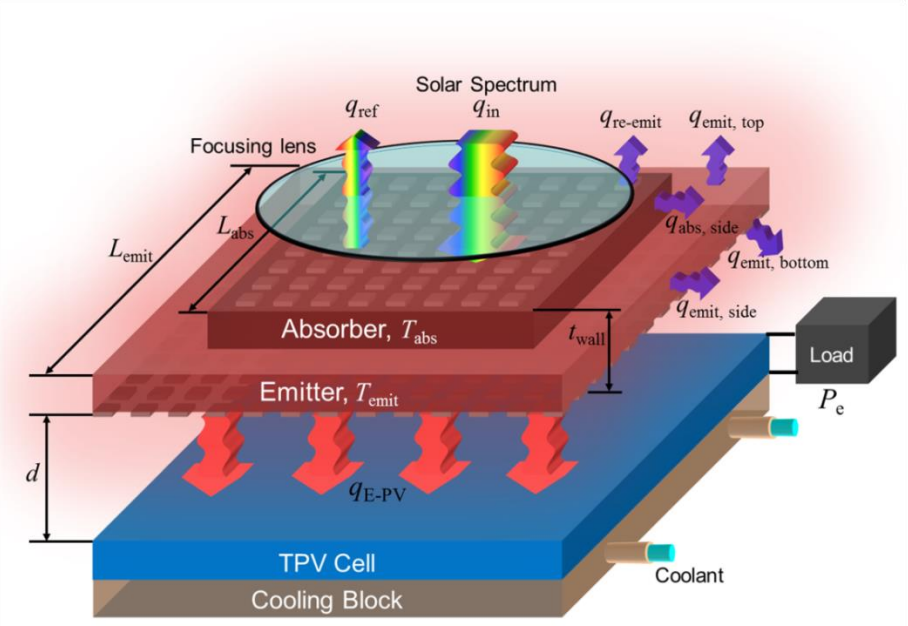

Figure 4.1 Schematic for a solar thermophotovoltaic system

The total solar-to-electricity conversion efficiency for an STPV system is obtained by dividing the generated electrical power density by the total incident solar flux, which can be decomposed into three sub-efficiencies by:

$$\eta_{TPV} = \eta_{abs} \cdot \eta_{emit} \cdot \eta_{cell} \tag{4.7}$$

In Eq. (4.7), $\eta_{abs} = (q_{in} - q_{ref} - q_{re\text{-}emit} - q_{abs,side}) / q_{in}$ is the absorber efficiency, which is defined as the ratio of the energy flux converted to heat by the absorber divided by the total incident solar radiative heat flux. $\eta_{emit} = q_{E\text{-}PV,\ E \geq E_g} / (q_{E\text{-}PV} + q_{envi})$ is the emitter efficiency defined as the percentage of useful thermal radiative energy from the emitter which is collected by the TPV cell, where $q_{E\text{-}PV,\ E \geq E_g}$ represents the radiative heat flux collected by the TPV cell with photon energy above its bandgap. $\eta_{cell} = P_e / q_{E\text{-}PV,\ E \geq E_g}$ is

the TPV cell efficiency characterized as the ratio of the generated electricity power density divided by the useful radiative heat flux collected by the TPV cell, where P_e is the electricity power density generated by the TPV cell.

The TPV cell employed in this work is made of InGaAsSb with a bandgap of 0.54 eV (equivalently 2.3 μm in wavelength) [104]. The generated power density P_e can be calculated by:

$$P_e = V_{oc} I_{sc} FF \tag{4.8}$$

where V_{oc} and FF are respectively the open-circuit voltage and filling factor of the TPV cell obtained from Ref. [104]. I_{sc} is the short-circuit density calculated by:

$$I_{sc} = \int_{1\mu m}^{2.3\mu m} \frac{e\lambda}{hc} \eta_i(\lambda) q_{\lambda,\text{E-PV}} d\lambda \tag{4.9}$$

where e is the elementary electric charge, $\eta_i(\lambda)$ is the internal quantum efficiency (IQE) of the TPV cell [104], h is Planck's constant, c is the speed of light in vacuum, and $q_{\lambda,\text{E-PV}}$ is the spectral radiative heat flux between the TPV emitter and cell which can be obtained from Eq. (4.4). Note that the integration range is from 1 μm to 2.3 μm, which covers the wavelength range in which the TPV cell has non-zero quantum efficiency.

Figure 4.2(a) shows the spectral distribution of solar radiative heat flux at AM 1.5, as well as the thermal radiative heat flux from a blackbody at different temperatures. It can be observed that at the temperature of 400 °C, the intensity of thermal emission is comparable to the incident solar radiation. It is also found that most of the energy from solar radiation is distributed in visible and near infrared regime, while most of the energy from thermal emission is in the mid-infrared range according to Wien's displacement law.

In order to maximize the efficiency of solar absorbers, it is crucially important to increase the absorbed solar radiation and reduce the energy loss from thermal re-emission, which can be realized by modifying the radiative properties of the solar absorbers. Figure 4.2(b) shows the absorptance for an ideal absorber, which exhibits unity absorptance below cutoff wavelength $\lambda_{c,abs}$ to maximize the absorbed solar radiation, and zero emittance beyond cutoff wavelength to minimize the thermal re-emission. Note that, the efficiency of an ideal absorber is a function of $\lambda_{c,abs}$, and the optimal $\lambda_{c,abs}$ varies with changed incident solar concentrations.

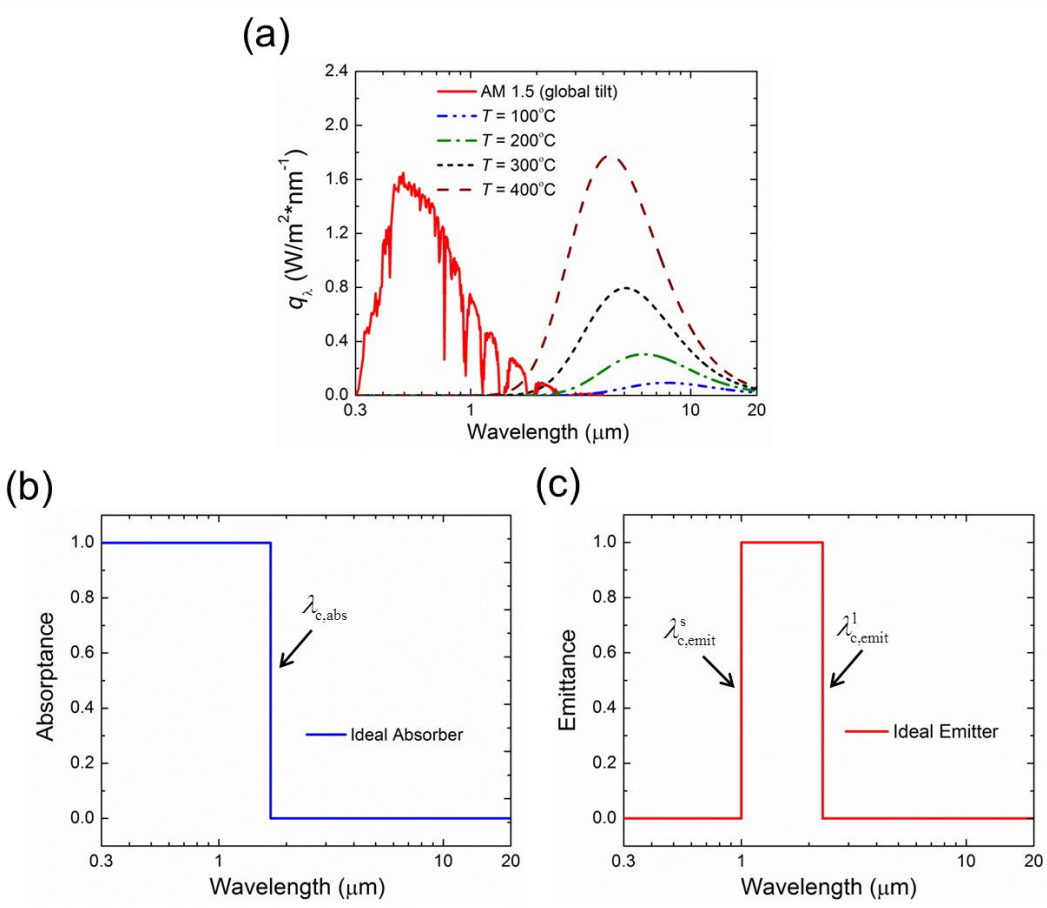

Figure 4.2 (a) Radiative energy distribution for solar and thermal radiation; (b) Absorptance for an ideal solar absorber; (c) Emittance for an ideal TPV emitter.

The emittance for an ideal TPV emitter is plotted in Fig. 4.2(c), which is unity in the wavelength range between $\lambda_{c,emit}^{s}$ and $\lambda_{c,emit}^{l}$, and zero outside this spectral regime. The purpose for this narrowband emitter is to avoid the wasted photons below the bandgap, which cannot generate electron-hole pairs, as well as to reduce the wasted excess energy above the bandgap. Since the value of $\lambda_{c,emit}^{l}$ is fixed at 2.3 μm which is the band edge of the InGaAsSb cell, the value of $\lambda_{c,emit}^{s}$ determines the performance of the TPV emitter. Similar to $\lambda_{c,abs}$, the value of $\lambda_{c,emit}^{s}$ needs to be optimized to maximize the STPV conversion efficiency. A great amount of the excess photon energy above bandgap of the TPV cell will be wasted if $\lambda_{c,emit}^{s}$ is too small (i.e., broad emission band), while the temperature of the absorber will dramatically increase if $\lambda_{c,emit}^{s}$ is too close to $\lambda_{c,emit}^{l}$ (with a narrow emission band), which will in turn increase the thermal re-emission loss and diminish the performance of the solar absorber.

In order to investigate the effect of $\lambda_{c,abs}$ and $\lambda_{c,emit}^{s}$ on the performance of the STPV system, parameter sweeps are performed for $\lambda_{c,abs}$ and $\lambda_{c,emit}^{s}$ with a fixed concentration factor of 50. Note that in the analysis here, the energy loss due to sidewall emission from the absorber-emitter module ($q_{abs,side}$ and $q_{emit,side}$) is neglected, as well as the energy loss due to non-unity view factor between the TPV emitter and cell ($q_{emit,bottom}$). These non-ideal factors will be discussed later. Also, the STPV systems with the same absorber and emitter area are discussed first, while the non-planar configuration with a smaller absorber and bigger emitter will be considered later.

The absorber/emitter temperature is plotted as a function of cutoff wavelengths in Fig. 4.3(a), in which brighter color represents higher temperature. Note that the absorber temperature is obtained by analyzing the energy balance defined in Eq. (4.1), and it is strongly correlated with the concentration factor for the incident solar radiation. It can be observed that as $\lambda_{c,emit}^{s}$ increases, the absorber temperature increases up to higher than 1600 K. This is because the emission band becomes narrower as $\lambda_{c,emit}^{s}$ increases, which will increase the absorber/emitter temperature due to weaker heat dissipation from the emitter. Note that in practice, the absorber temperature is limited by the melting point of the materials used for the absorber and emitter.

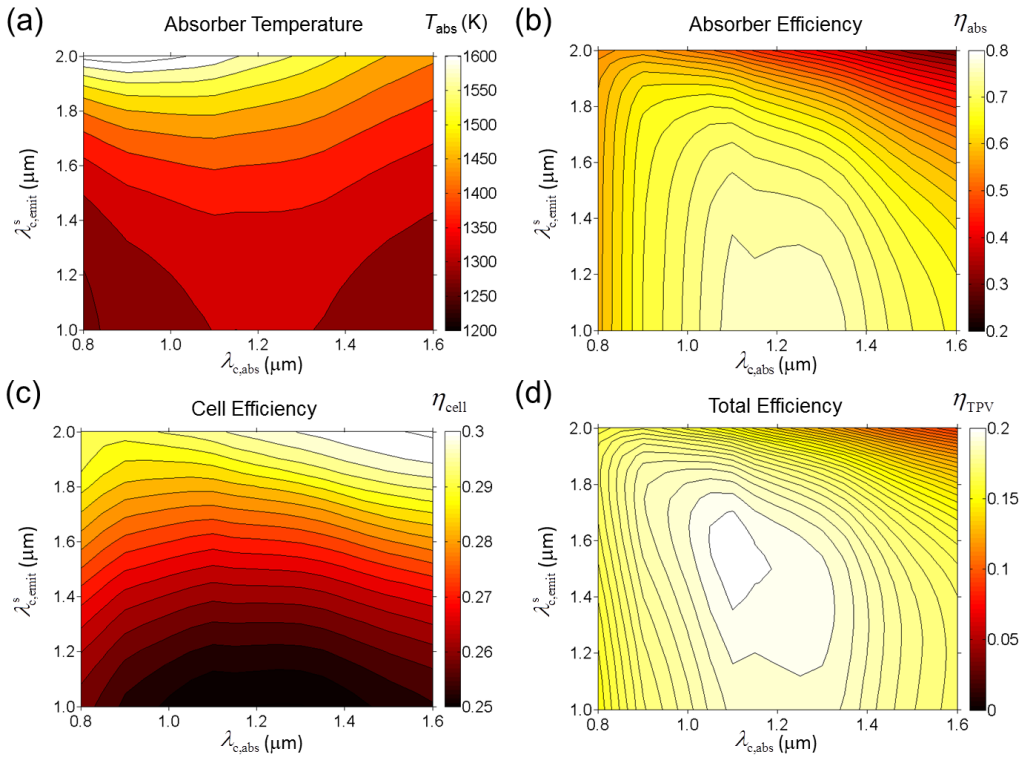

Figure 4.3 (a) Absorber temperature; (b) Absorber efficiency; (c) Cell efficiency and (d) Total system efficiency for STPV system employing absorber and emitter with different cutoff wavelengths.

Figure 4.3(b) shows the absorber efficiency as a function of $\lambda_{c,abs}$ and $\lambda_{c,emit}^{s}$. It can be found that the absorber efficiency is maximized when $\lambda_{c,abs}$ is around 1.2 μm, in which case most incident solar radiation can be absorbed and little energy is dissipated through thermal radiation. It can also be observed that the absorber efficiency decreases as $\lambda_{c,emit}^{s}$ increases, which is the result of an increased absorber temperature caused by the narrower emission band. It is easy to understand that the absorber efficiency will drop when the thermal re-emission loss increases due to raised absorber temperature. Note that the emitter efficiency is 100% regardless of the values of $\lambda_{c,abs}$ and $\lambda_{c,emit}^{s}$, which is because the emittance for an ideal emitter is zero below the bandgap of TPV cell. Therefore, without considering the radiative energy lost to the environment through the sidewall and bottom surface of the emitter, the fraction of useful photon energy above the bandgap of TPV cell is always 100%.

Figure 4.3(c) shows the TPV cell efficiency as a function of cutoff wavelengths. It can be observed that the cell efficiency increases as $\lambda_{c,emit}^{s}$ increases (i.e. narrower emission band). This is because photons with energy higher than the bandgap of TPV cell can at most generate one electron-hole pair in most cases, and the excess energy exceeding the bandgap is wasted. Therefore, in order to maximize the TPV cell efficiency, it is ideal to have an emitter with an extremely narrow emission band right above the bandgap of the TPV cell. However, this will increase the absorber temperature and diminish the performance of the STPV absorber as indicated in Fig. 4.3(b). Therefore, there exists a trade-off between the absorber efficiency and TPV cell efficiency

associated with the width of the emitter's emission band. After all, it is the total efficiency for the STPV system that matters. Figure 4.3(d) plots the total conversion efficiency for the STPV system as a function of $\lambda_{c,abs}$ and $\lambda_{c,emit}^{s}$. It can be found that the maximum total efficiency of 20% occurs when $\lambda_{c,abs}$ and $\lambda_{c,emit}^{s}$ are respectively around 1.1 μm and 1.5 μm. Note that these optimal cutoff wavelengths are only valid under 50 suns, and they will vary with different concentration factors.

The performance of the STPV system with ideal absorbers and emitters is further investigated under varied incident solar concentration factors. Note that the cutoff wavelengths of ideal absorber and emitter are optimized to achieve maximum total conversion efficiency for a given concentration factor. Figure 4.4(a) shows the absorber temperature as a function of the incident concentration factor, which shows that the absorber temperature increases from 1230 K to 1700 K when the concentration factor increases from 20 to 200. Figure 4.4(b) plots the absorber, emitter, cell and total efficiency as a function of the absorber temperature. It can be observed that the absorber efficiency decreases with increased absorber temperature. This is because when the absorber temperature increases, the peak for thermal radiative intensity will shift to shorter wavelengths (Wien's displacement law), where the emittance for the absorber is high. Therefore, the radiation loss becomes stronger which leads to a lower absorber efficiency. The emitter efficiency is 100% as the emittance is zero below the bandgap of TPV cell for ideal emitters, with the assumption that the energy losses from sidewall and non-unity emitter-cell view factor are neglected. The cell efficiency decreases with increased emitter temperature, which will be discussed in detail later. In sum, the total efficiency for the STPV system with ideal surfaces decreases from 22.6% to 11.1% when

the absorber temperature increases from 1230 K to 1700 K.

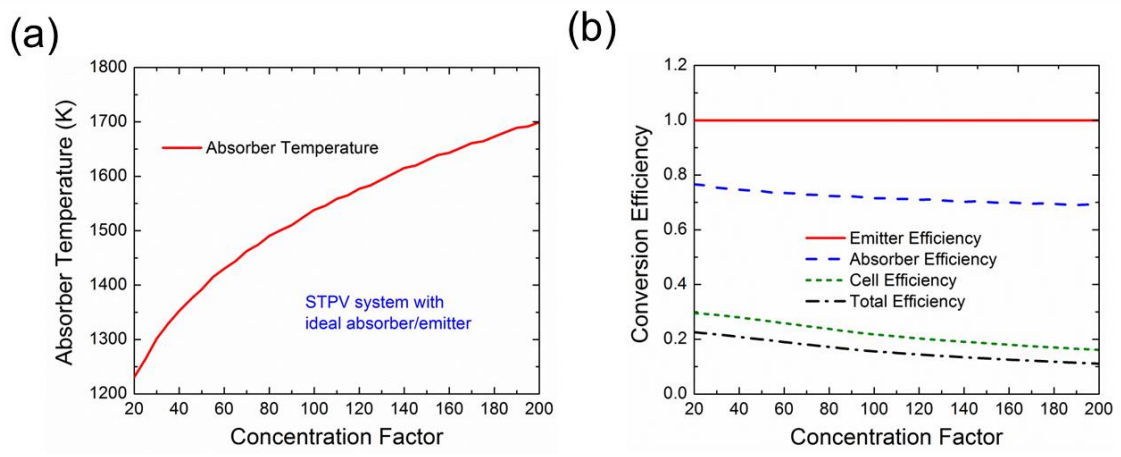

Figure 4.4 (a) Absorber temperature and (b) Total system efficiency for STPV system employing ideal absorber and emitter.

4.1.2 Theoretical Analysis for STPV System Employing Metamaterial Absorber/Emitter and Actual TPV Cells

Previously, the performance of the STPV systems with ideal absorbers and emitters is investigated. However, in actual STPV systems, the absorber and emitter have neither ideal cutoff wavelengths nor perfect (unity or zero) spectral absorptance/emittance. Here, we consider to employ film-coupled metamaterial absorbers and emitters, whose radiative properties exhibit strongly spectral selectivity and diffuse behaviors from our previous theoretical [12, 39] and experimental studies [39] to enhance the STPV performance.

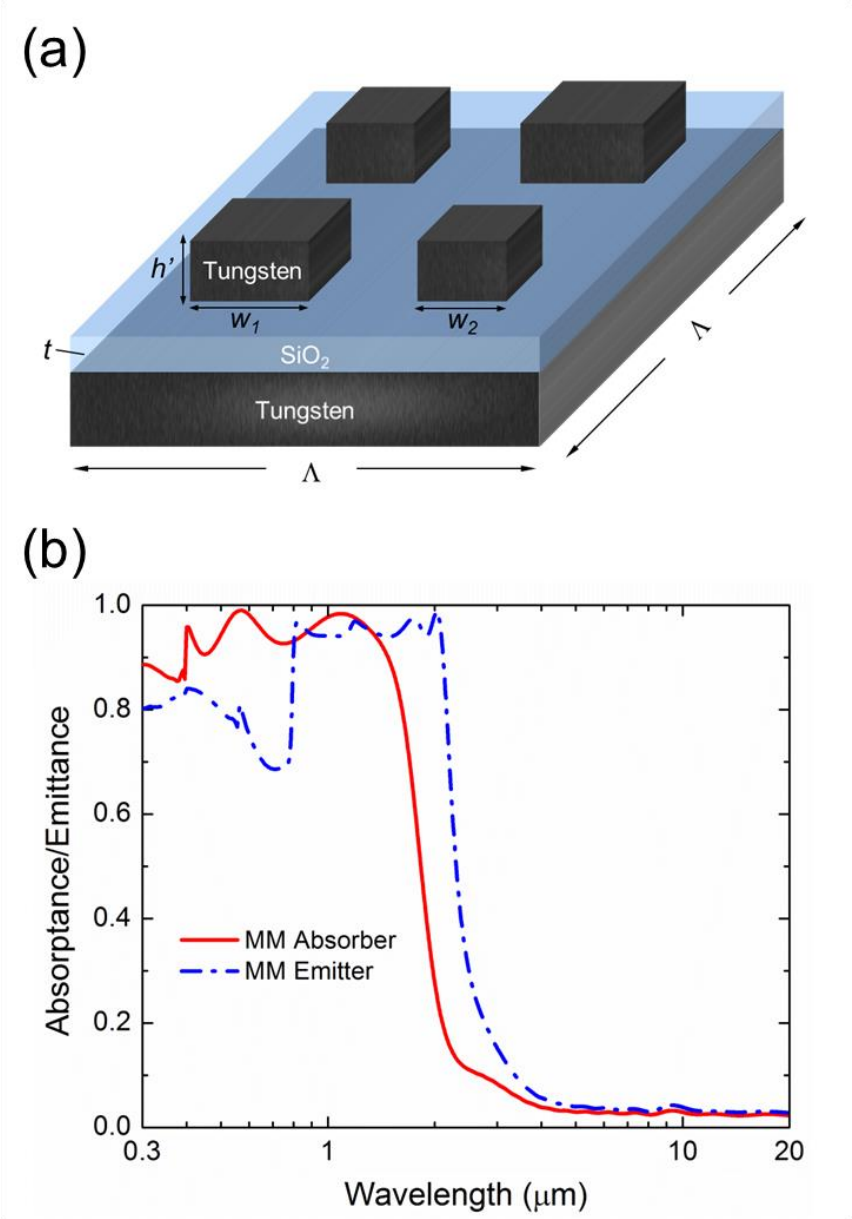

Figure 4.5 (a) Schematic for the metamaterial absorber and emitter; (b) Simulated normal absorptance/emittance of designed selective metamaterial solar absorber and thermal emitter in the STPV system.

Figure 4.5(a) depicts the schematic for the metamaterial absorber and emitter, which are film-coupled structures with tungsten grating and substrate separated by a SiO_2 spacer. The geometric parameters are different for the absorber and emitter with different cutoff wavelengths. The absorber has single sized grating on the top (i.e., $w_1 = w_2 = 0.2$

μm), with grating period $\Lambda/2$ = 0.4 μm, grating height h' = 100 nm, and spacer thickness t = 60 nm. On the other hand, the emitter is made of double sized grating with w_1 = 0.3 μm, w_2 = 0.4 μm, Λ = 1.6 μm, h' = 200 nm, and spacer thickness t = 60 nm. Note that the radiative properties for the metamaterial absorber and emitter are highly dependent on the geometric parameters and can be tuned for different applications.

The spectral normal absorptance/emittance obtained from finite-difference time-domain (FDTD) simulations for the metamaterial absorber and emitter is plotted in Fig. 4.5(b), with the wavelength in logarithm scale. It can be observed that the metamaterial absorber exhibits high absorptance from 0.3 to 1.5 μm, and low emittance beyond 1.5 μm. On the other hand, the emitter has a high emittance between 0.8 and 2.2 μm, and low emittance down to 4% in the mid-infrared. The spectral selectivity of the radiative properties of metamaterial absorber and emitter is due to the phenomenon of Wood's Anomaly, as well as the excitation of surface plasmon polariton (SPP) and magnetic polariton (MP), which have been thoroughly studied in Ref. [12]. Note that even though the cutoff wavelengths for the solar absorber and TPV emitter can be tuned by changing the geometric parameters, the tunability is still limited and the radiative properties for the actual absorber and emitter cannot be modified to be exactly the same as ideal ones. Though the spectral-normal radiative properties are shown here, our previous studies have demonstrated the diffuse-like behaviors of these film-coupled metamaterials.

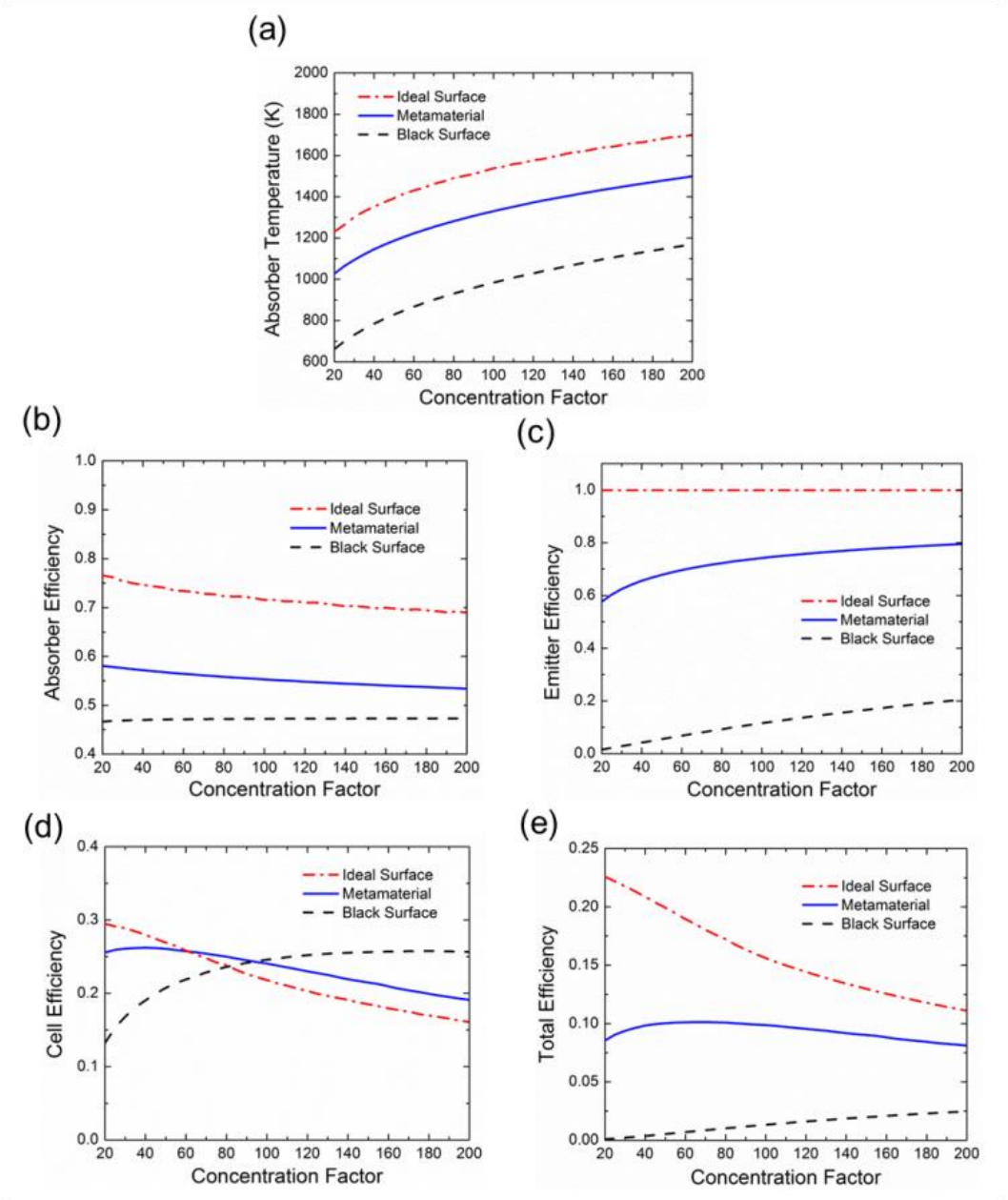

Figure 4.6 (a) Absorber temperature; (b) Absorber efficiency; (c) Emitter efficiency; (d) Cell efficiency; and (e) Total efficiency for STPV systems with metamaterial, ideal and black absorber/emitter.

With the radiative properties obtained for the metamaterial absorber and emitter, the performance of the STPV system utilizing metamaterial absorber and emitter can be analyzed. Figure 4.6(a) shows the absorber/emitter temperature under different solar

concentrations, for the STPV systems with ideal, metamaterial and black surfaces as absorber and emitter. It is observed that for the STPV system with metamaterial surfaces, the absorber temperature increases from around 1000 K to 1500 K when concentration factor ranges from 20 to 200. Through comparison, it is found that the absorber temperature for the STPV system with ideal surfaces is the highest, while the STPV system with black surfaces exhibits the lowest absorber temperature. This is because the total emittance for an ideal emitter is very low due to its narrow emission band, which leads to a higher absorber/emitter temperature due to a weaker heat dissipation through thermal radiation from the emitter. On the contrary, since the total emittance for the black emitter is as high as unity, the temperature of black absorber/emitter will be the lowest.

Figure 4.6(b) shows the absorber efficiency as a function of concentration factor for STPV systems with ideal, metamaterial and black absorber/emitter. It is observed that for the STPV system with metamaterial surfaces, the absorber efficiency drops from 58% to 53% when concentration factor varies from 20 to 200. The decreased absorber efficiency with increased concentration factor is mainly because the peak of thermal radiative intensity shifts to shorter wavelength when the absorber temperature is increased with higher concentration factors. Therefore, the total thermal emittance for the solar absorber will be higher as its spectral emittance is higher in shorter wavelengths, which leads to a higher thermal re-emission loss and a lower absorber efficiency. The same trend is also observed for the STPV system with ideal surfaces, whose absorber efficiency is about 20% higher than the STPV system with metamaterial surfaces. On the other hand, the absorber efficiency of the STPV system with black surfaces barely changes with concentration factor, as the total emittance for the black absorber remains as

unity regardless of its temperature. As a result of spectral selectivity, the STPV system with metamaterial surfaces exhibits an absorber efficiency which is at least 10% higher than that with black surfaces.

Figure 4.6(c) shows the emitter efficiency as a function of the concentration factor. As explained previously, the emitter efficiency remains as 100% for STPV systems with ideal emitter. On the other hand, the emitter efficiencies for STPV systems with metamaterial and black emitters are below 100% due to the wasted emission below the bandgap of TPV cell. It is observed that the emitter efficiency increases from 58% to 80% for the STPV system with metamaterial surfaces, as the concentration factor increases from 20 to 200. This is because the emitter temperature increases with increased incident solar concentration, which shifts the peak for radiative intensity to shorter wavelength and decreases the percentage of emitted photons with energy below the bandgap of the TPV cell. By comparison, the STPV system with black emitter exhibits much poorer emitter efficiency due to its non-selective thermal emittance, and a large amount of energy is wasted on photons with energy below the bandgap of the TPV cell.

Figure 4.6(d) indicates the cell efficiency for the STPV systems with different absorber/emitter surfaces under varied solar concentration. It can be observed that the cell efficiency of the STPV system with ideal surfaces decreases with increased incident solar concentration, while the STPV system with black surfaces exhibits opposite trend. On the other hand, the trend for cell efficiency of the STPV system with metamaterial absorber and emitter is not monotonic, which increases first but starts to decrease at concentration factor around 40. The different trends originate from different absorber/emitter temperatures for the three STPV systems. The cell efficiency reaches maximum when

most photons emitted from the emitter have photon energy right above the cell bandgap, in which case little energy is wasted on photons with energy either lower or much higher than the bandgap of the TPV cell. For the STPV system with metamaterial surfaces, the cell efficiency reaches maximum with a concentration factor of around 40, which corresponds to an emitter temperature of 1200 K. Based on Wien's displacement law, the peak for thermal radiative intensity is at 2.4 μm with temperature of 1200 K, which is close to the bandgap of the TPV cell. Therefore, the maximum cell efficiency is obtained with a concentration factor of around 40 for the STPV system with metamaterial surfaces, when most of the photon energy is right above the bandgap of TPV cell. On the other hand, the emitter temperature is higher for the STPV system with ideal surfaces, and the emitter temperature reaches 1200 K at a concentration factor smaller than 20. Therefore, the peak of radiative intensity is shifting away from the bandgap to shorter wavelengths when the concentration factor increases from 20 to 200. As a result, the cell efficiency decreases with increased solar concentration. In contrast, for the STPV system with black surfaces which exhibits a lower emitter temperature, the peak for thermal radiative intensity is shifting towards the bandgap of TPV cell from longer wavelength when the concentration factor increases from 20 to 200. Therefore, the cell efficiency increases with increased solar concentration for the STPV system with black surfaces.

Figure 4.6(e) shows the total efficiency for the STPV systems with ideal, metamaterial and black surfaces. It can be observed that the total conversion efficiency for the STPV system with metamaterial absorber and emitter varies from 8% to 10% with different solar concentrations, which is greatly enhanced compared with the efficiency of less than 2.5% for the STPV system with black absorber and emitter. However, it is still

lower than the STPV system with ideal absorber and emitter, which varies from 11% to 23% with different incident solar concentrations.

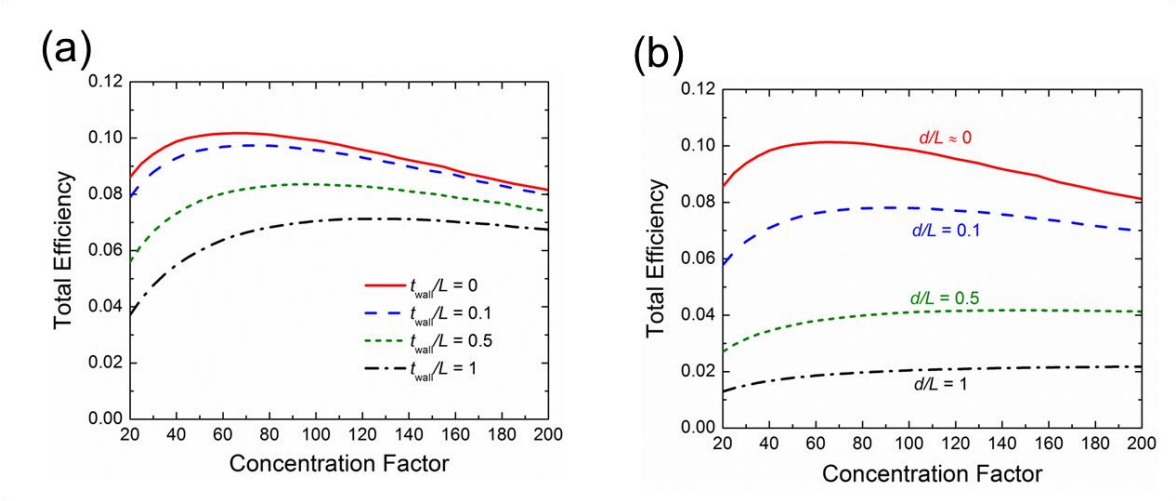

Figure 4.7 Effects on the total system efficiency of: (a) Sidewall thickness; (b) Non-unity view factor between the TPV emitter and cell.

The discussions about previous figures consider the ideal cases that there are no energy losses through sidewall emission from the absorber ($q_{abs,side} = 0$) and emitter ($q_{emit,side} = 0$), and that the view factor between the TPV emitter and cell is unity ($q_{emit,bottom} = 0$). However, these two non-ideal factors have to be considered in practical applications. Figure 4.7(a) shows the total conversion efficiency with different ratios of t_{wall}/L for the STPV system with metamaterial absorber and emitter. Note that t_{wall} is the total sidewall thickness for the absorber-emitter module which will affect both the $q_{abs,side}$ and $q_{emit,side}$, while L is the length for the STPV absorber and emitter ($L_{abs} = L_{emit} = L$). The emittance of the sidewall for both the absorber and emitter is taken as 0.05 (the sidewall is assumed to be diffuse and gray) considering that the sidewall is covered by weakly emitting materials (metal). Due to the energy loss through sidewall emission, the

STPV system shows diminished performance with thicker sidewall, with a maximum total efficiency of 10.1%, 9.7%, 8.4% and 7.1% when the t_{wall}/L ratio is respectively 0, 0.1, 0.5 and 1. Figure 4.7(b) shows the effect of the distance d between the TPV emitter and cell, in which the d/L ratio affects $q_{emit,bottom}$ by changing the view factor between the TPV emitter and cell. It can be found that the maximum total efficiency for the STPV system decreases from 10.1% to 2.2% when the value of the d/L ratio is increased from 0 to 1, indicating a substantial energy loss due to a decreased view factor between the TPV emitter and cell. As a conclusion, it is crucial to fabricated ultrathin solar absorber and TPV emitter, as well as to keep a small distance between the TPV emitter and cell for a large view factor.

Previous discussions analyzed the efficiency of STPV systems with simple planar layout (i.e. same emitter and absorber surface areas), while a different emitter-absorber area ratio (A_{emit}/A_{abs}) with the solar radiation concentrated to a smaller absorber would also affect the photon transport and power generation. Note that when the absorber and emitter have different surface areas, the $q_{emit,top}$ in Eq. (4.5) will not be zero, which is different from the STPV system with planar layout. The emittance for the top surface of the emitter is considered as 0.05, which is the same as the sidewall. Figure 4.8(a) shows the absorber/emitter temperature for the metamaterial based STPV system with different A_{emit}/A_{abs} ratios. Note that in this case the sidewall emission loss is neglected, and the view factor between the TPV emitter and cell is considered as 1. It can be found that a larger A_{emit}/A_{abs} ratio results in a lower absorber temperature. This is because with a larger A_{emit}/A_{abs} ratio, the absorber-emitter module is absorbing less solar radiation and emitting more thermal radiation, which leads to a lower absorber temperature.

Figure 4.8(b) shows the absorber efficiency for the metamaterial based STPV system with different A_{emit}/A_{abs} ratios. It can be observed that the absorber efficiency increases from around 55% to 85% as the A_{emit}/A_{abs} ratio varies from 1 to 8. This is because the energy loss through thermal self-emission is greatly reduced when the absorber temperature is decreased with a larger A_{emit}/A_{abs} ratio.

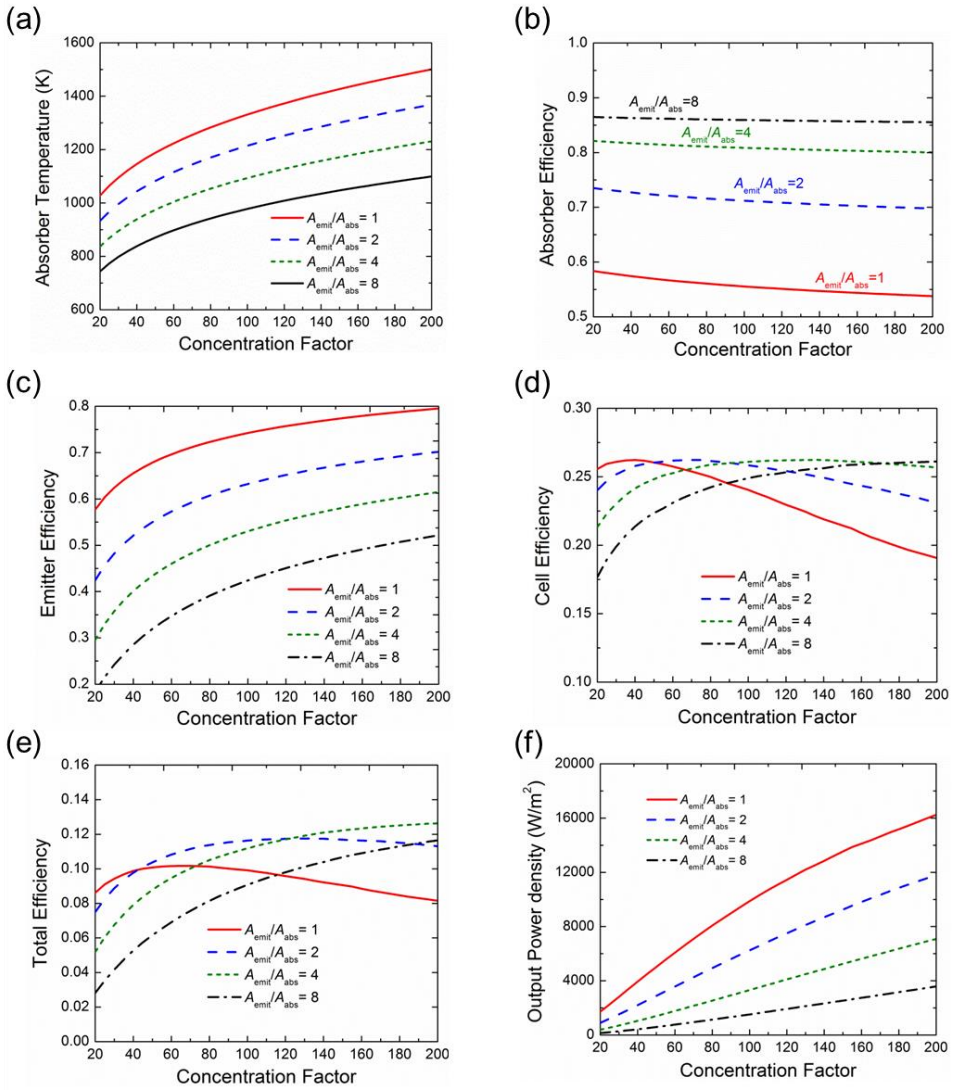

Figure 4.8 Effects of absorber-emitter area ratio on the: (a) Absorber temperature; (b) Absorber efficiency; (c) Emitter efficiency; (d) Cell efficiency; (e) Total efficiency; (f) Total output power density of the STPV system.

Figure 4.8(c) plots the emitter efficiency with different A_{emit}/A_{abs} ratios. In contrary to the effect of A_{emit}/A_{abs} ratio on the absorber efficiency, the emitter efficiency decreases with increased A_{emit}/A_{abs} ratio. This is caused by two main reasons: 1. There will be more radiative energy loss from the top of the emitter when the A_{emit}/A_{abs} ratio becomes larger; 2. When the emitter temperature decreases with larger A_{emit}/A_{abs} ratio, the emitter will radiate more photons with energy below the bandgap of the TPV cell, which leads to a lower percentage of useful photon energy (i.e. emitter efficiency).

Figure 4.8(d) shows that the cell efficiency is not substantially different with varied A_{emit}/A_{abs} ratio. It can be also observed that the cell efficiency reaches maximum at lower concentration factor for smaller A_{emit}/A_{abs} ratios, while the maximum cell efficiency is acquired at higher concentration factor for larger A_{emit}/A_{abs} ratios. This is also related with different emitter temperature when the A_{emit}/A_{abs} ratio is varied. As shown in Fig. 4.6, the cell efficiency reaches maximum when the emitter temperature is around 1200 K. For STPV systems with larger A_{emit}/A_{abs} ratios, the emitter temperature is lower and reaches 1200 K at higher concentration factors; while for STPV systems with smaller A_{emit}/A_{abs} ratios, the emitter temperature is higher and reaches 1200 K at lower concentration factors. Therefore, the maximum cell efficiency for the STPV systems with larger A_{emit}/A_{abs} ratios reaches maximum at a higher concentration.

It is found here that the A_{emit}/A_{abs} ratio has different effects on the absorber, emitter and cell efficiency of the STPV system. Therefore, the total efficiency for the STPV system will not simply increase or decrease with increased A_{emit}/A_{abs} ratio. Instead, an optimized A_{emit}/A_{abs} ratio exists for maximum total efficiency. Figure 4.8(e) shows that the STPV systems with A_{emit}/A_{abs} ratios of 2 or 4 exhibit maximum total efficiency for

most concentration factors. The total system efficiency can reach a maximum of 12.6% under 200 suns with an A_{emit}/A_{abs} ratio of 4. Although a larger A_{emit}/A_{abs} ratio leads to a higher system efficiency at most incident concentration factors, a smaller absorber area will lead to a decreased total power output density from the TPV cell due to the decreased power input onto a smaller absorber area. Figure 4.8(f) shows the output power density from the TPV cell for different A_{emit}/A_{abs} ratios, which indicates that a larger A_{emit}/A_{abs} ratio achieves a higher system efficiency at the cost of a lower output power density.

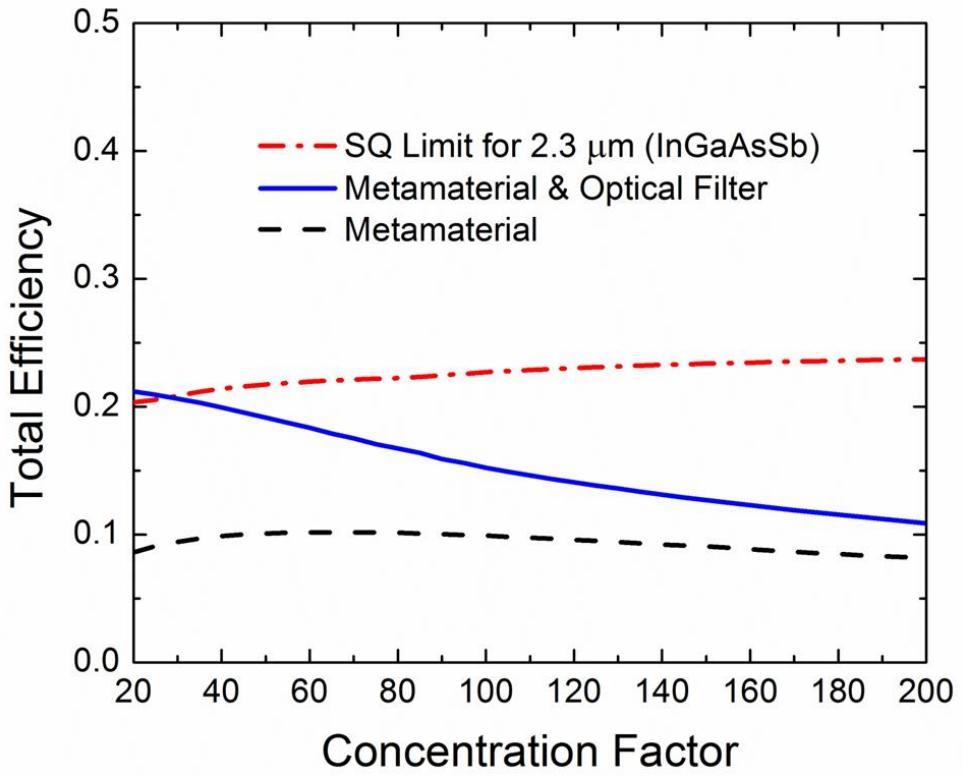

Figure 4.9 Total STPV efficiency for the systems employing metamaterial absorber/emitter, metamaterial absorber/emitter & optical filter, as well as the Shockley-Queisser limit for InGaAsSb cell. The optical filter for the absorber has transmittance $T = 1$ for $\lambda < 1$ μm, while $T = 0$ for $\lambda > 1$ μm. The optical filter for the emitter has $T = 1$ for only a narrow transmission band between 1.5 μm and 2.2 μm.

Apart from changing the absorber/emitter area ratio, adding an optical filter to the STPV absorber and emitter is another possible approach to further boost the system efficiency. The STPV absorber requires an optical filter with unity transmittance in the visible and NIR to transmit solar radiation onto the absorber, while it should have zero transmittance in the IR to reflect the thermal re-emission of the absorber back to the system and reduce the energy loss. On the other hand, the optical filter for the emitter should possess a narrow transmission band in the NIR just above the bandgap of the TPV cell, where the cell efficiency will be the highest.

The efficiency of the STPV system employing optical filters was investigated and the result is shown in Fig. 4.9. An optical filter with $T = 1$ for $\lambda < 1$ μm and $T = 0$ for $\lambda > 1$ μm was considered for the STPV absorber, while another filter with a narrow transmission band between 1.5 μm and 2.2 μm was integrated with the emitter. The efficiency for the STPV system employing metamaterial absorber/emitter and optical filters is shown by the blue curve in Fig. 4.9. The efficiencies for STPV system without optical filters as well as the Shockley-Queisser limit for InGaAsSb cell are also plotted as a comparison. It is observed that by adding the optical filters into the STPV system, the conversion efficiency is greatly boosted, even surpassing the Shockley Queisser limit at low concentration factors. Comparing the conversion efficiency for the STPV systems with and without optical filters, it is observed that the enhancement of efficiency is higher at low concentration factors, while the enhancement becomes less significant at high concentration factors. This is because that at high concentration factors, reducing the thermal re-emission loss becomes less important since the absorbed incident radiation is huge and dominating in determining the absorber efficiency. Therefore the optical filter

for the absorber is not important. On the other hand, when the incident solar radiation becomes stronger, the emitter temperature will be higher which shifts its emission band to shorter wavelength. As a result, the optical filter for the emitter is less important since the wasted photons with energy below the bandgap of the TPV cell will be less. Hence reducing this part of energy loss by adding an emitter filter is less important.

4.1.3 Theoretical Analysis for STPV System Employing Ideal Cells

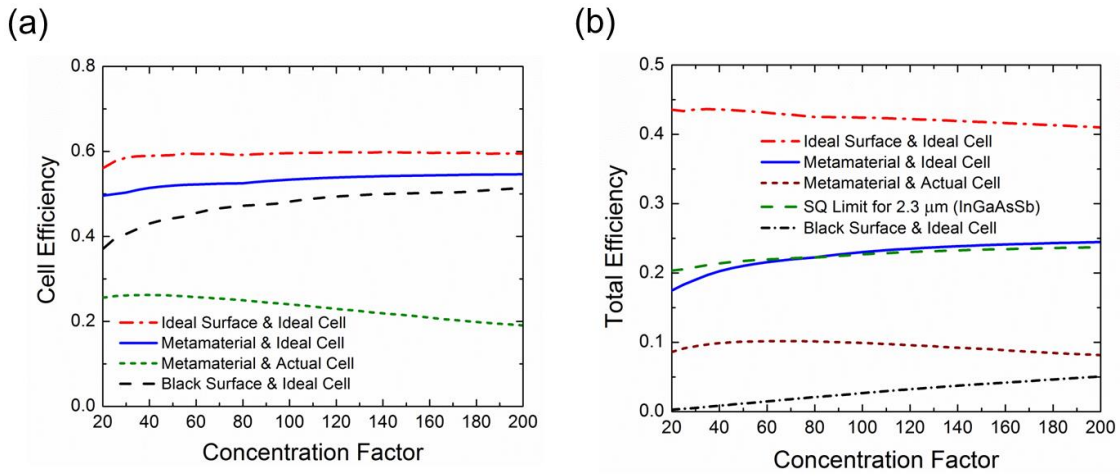

Figure 4.10 (a) Cell efficiency and (b) Total efficiency for STPV systems employing different set of absorber/emitter and cells (actual and ideal).

In previous section, the efficiency analysis for STPV systems employing actual InGaAsSb cell is performed. It can be observed that the total conversion efficiency is strongly constrained by the low cell efficiency. In order to figure out the potential for the STPV efficiency to surpass the Shockley Queisser limit, the STPV systems employing ideal cells are investigated in this section. Note that the generated current of an ideal cell is limited by the Shockley Queisser limit [52] and can be calculated by:

$$I = \int_{E_G}^{\infty} \frac{2\pi e\varepsilon(E)E^2 dE}{h^3c^2 \exp(\frac{E}{kT_{\text{emit}}}) - 1} - \int_{E_G}^{\infty} \frac{2\pi eE^2 dE}{h^3c^2 \exp(\frac{E - qV}{kT_{\text{cell}}}) - 1} \tag{4.10}$$

where I is the current, E is the photon energy, $\varepsilon(E)$ is the emitter emittance, T_{emit} and T_{cell} are respectively the cell and emitter temperature, h is the Planck's constant, c is the speed of light in vacuum, e is the elementary charge, and V is the voltage bias for the solar cell. The generated power for ideal cells can be calculated by:

$$P_{\text{cell, ideal}} = \max(I(V)V) \tag{4.11}$$

The cell efficiency can be determined by $\eta_{\text{cell}} = P_{\text{cell,ideal}} / q_{\text{E-PV, E}\geq\text{E}_g}$.

Figure 4.10(a) shows the cell efficiency for STPV systems employing ideal cell, in comparison with the cell efficiency for STPV systems utilizing actual cell. It is found that the cell efficiency for STPV systems employing ideal cells is enormously boosted compared with systems utilizing actual cell, which reaches to around 60% for the STPV system with ideal absorber/emitter and ideal cell. It is also found that the cell efficiency for the STPV system with ideal surface is slightly higher than the STPV systems with metamaterial and black surfaces. This is because that the emitted thermal radiation towards the TPV cell from the ideal emitter is a narrow band emission with most of the energy right above the bandgap of the cell. In this case, the wasted energy carried by photons with energy below the cell bandgap will be reduced, as well as the energy loss in hot electrons, which leads to a slightly higher cell efficiency.

Figure 4.10(b) presents the total conversion efficiency for STPV systems employing ideal cell along with different absorber/emitter sets. It is found that the STPV system with ideal absorber/emitter & ideal cell shows conversion efficiency higher than

40%, which is much higher than the Shockley Queisser limit. For STPV system with metamaterial absorber/emitter and ideal cell, the conversion efficiency is comparable to the Shockley Queisser limit, which surpasses the Shockley Queisser limit at concentration factor large than 100. It is found in this section that, for STPV system employing ideal TPV cells, the conversion efficiency could be enormously boosted and exhibit the potential to exceed the Shockley Queisser limit.

4.2 Experimental Investigation of TPV System Employing Metafilm Emitter

In this Section, the experimental investigation of a TPV system employing metafilm emitter will be discussed. The experimental fabrication of the TPV emitter will be discussed here, which a multilayer structure with W-SiO_2-W-Si_3N_4-SiO_2 configuration.

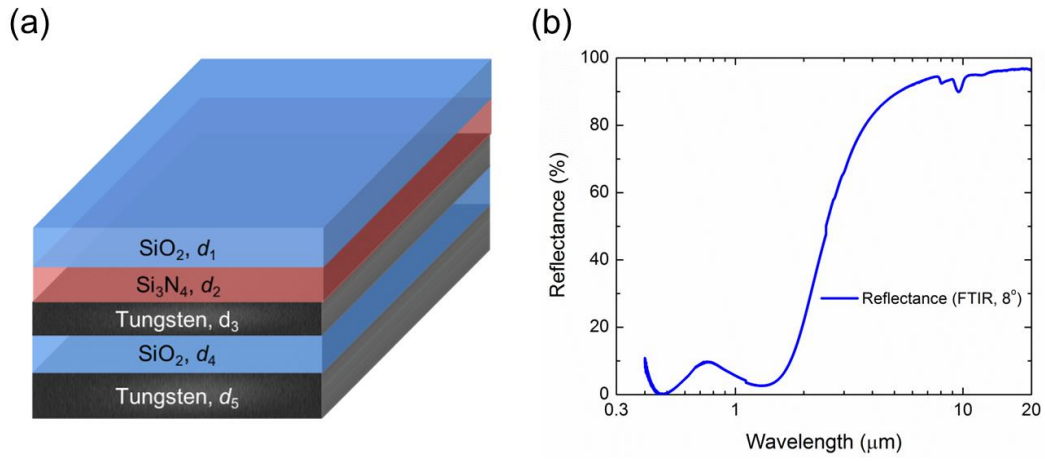

Figure 4.11 (a) Structure schematic and (b) Measured specular reflectance by the FTIR for the multilayer TPV emitter.

Figure 4.11(a) shows the schematic of the TPV emitter, it is a fiver layer metafilm structure with W-SiO_2-W-Si_3N_4-SiO_2 configuration. The W-SiO_2-W layers form a Fabry-Perot cavity to achieve spectral selectivity in its emittance, while the Si_3N_4 and SiO_2

layers on the top serve as anti-reflection coatings to enhance the visible/NIR emittance as well as protective layers. The W-SiO_2-W stack at the bottom was fabricated by sputtering (Lesker, PVD75 Sputter Coater), while the Si_3N_4 and SiO_2 layers on top were deposited with chemical vapor deposition (CVD, ASU Center for Solid State Electronics Research, Plasma Quest). The dielectric layers on top were deposited with CVD so they could exhibit better quality to serve as an oxygen passivation layer under high temperatures [100]. The fabrication parameters for the multilayer emitter are shown in Table 4.1.

Figure 4.11(b) show the specular reflectance of the TPV emitter measured with the FTIR spectrometer at incidence angle of 8^o. The reflectance was measured from 0.4 μm to 20 μm with a resolution of 4 cm^{-1} in wavenumber. The measurement was averaged from 32 scans with an Al mirror as the reference, and the measured reflectance was normalized by the theoretical reflectance of Al. It is observed that the reflectance is lower than 10% from 0.4 μm~ 1.5 μm, indicating emittance > 90% from 0.4 μm~ 1.5 μm for the TPV emitter considering that $\alpha = 1\text{-}R$. On the other hand, the IR reflectance is higher than 90%, demonstrating that the TPV emitter is weakly emitting in the IR.

Table 4.1. Deposition parameters for different layers in the multilayer selective solar absorber.

Material	Layer thickness (nm)	Deposition method	Deposition rate (Å/s)	Base pressure (10^{-6} Torr)	Sputtering pressure (mTorr)	Sputtering power (W)
W substrate	300	DC Sputtering	1.8	2.5	3.5	150
SiO_2 cavity	55	DC Sputtering	0.45	2.5	3.5	200
W thin film	10	RF Sputtering	0.5	2.5	40	35
Material	Depostion time (s)	Deposition method	Base pressure (mTorr)	Chamber temperature (^{o}C)	Chamber wall temperature (^{o}C)	Reflected RF power (W)
Si_3N_4	1071	CVD	50	300	40	~2
SiO_2 top layer	996	CVD	50	300	40	~2

The future work will cover the experimental testing and characterization for the TPV system. The system will be packaged in a vacuum chamber, with a motorized Z stage based platform to maintain a small gab between the TPV emitter and cell. The IV curve will be characterized for the TPV cell and the system conversion efficiency will be measured.

CHAPTER 5

PLASMONIC LIGHT TRAPPING IN NANOMETER PHOTOVOLTAIC LAYER WITH FILM-COUPLED METAMATERIALS

Conventional solar cells are usually hundreds of microns in thickness due to the small absorption coefficient of semiconductor materials. Geometric approaches such as anti-reflection coating and surface texturing could potentially enhance light absorption and reduce the thickness of solar cells, but the enhancement is limited by the $4n^2$ limit. On the other hand, plasmonic light trapping can achieve significant absorption enhancement in micro/nanostructured thin-film solar cells through the excitation of plasmonic resonances. In this chapter, a film-coupled concave grating metamaterial structure is proposed to enhance light absorption in an ultrathin photovoltaic layer.

5.1 Theoretical Background: Excitation of MPs in Concave Grating Based Metamaterials

A concave grating based metamaterial is discussed in this section, and the excitation mechanism of MPs is investigated. Figure 5.1(a) depicts the periodic film-coupled metamaterial structure under investigation, which is made of aluminum concave grating on a SiO_2 spacer and aluminum substrate. The 2D periodic mesh-like grating, which is considered to be symmetric in x and y directions for simplicity, has a cavity width *b*, ridge width *w*, grating period Λ, and grating height *h*, while the SiO_2 spacer thickness is *t*.

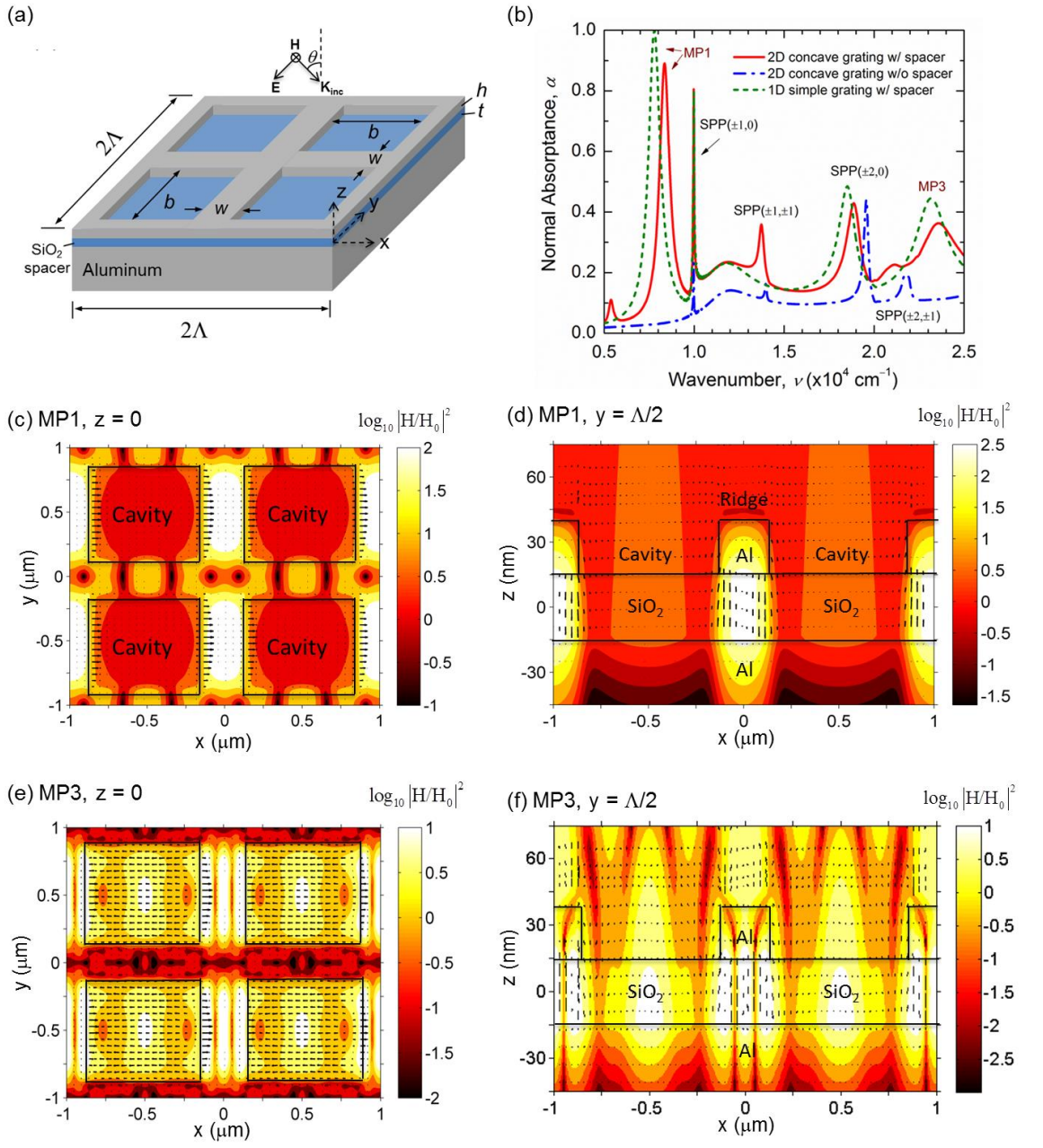

Figure 5.1 (a) Schematic and (b) normal absorptance for the concave grating metamaterial. Electromagnetic field distribution from the (c) top view and (d) cross-section view for MP1. Electromagnetic field distribution from the (e) top view and (f) cross-section view for MP3.

The spectral normal absorptance of the film-coupled concave grating structure with the set of base geometric values is presented in Fig. 5.1(b) at TM-wave incidence.

Absorption peaks are observed at the several frequencies of 8350 cm^{-1} (with absorptance α = 0.89), 9970 cm^{-1} (α = 0.80), 13740 cm^{-1} (α = 0.36), 18870 cm^{-1} (α = 0.43), 21150 cm^{-1} (α = 0.23), and 23580 cm^{-1} (α = 0.36). These peaks were respectively labeled as MP1, SPP(±1,0), SPP(±1,±1), SPP(±2,0), SPP(±2,±1), and MP3 from lower to higher frequencies, which are associated with the excitations of different MP and SPP modes.

To explain underlying mechanism for these absorption peaks associated with MPs, the distribution of electromagnetic fields at different sections inside the structure are illustrated in Fig. 5.1, with arrows symbolizing electric field vectors and contour representing the magnetic field strength as the logarithm of the square of magnetic field normalized to the incidence (i.e., $\log_{10}|H/H_{inc}|^2$). The electromagnetic fields from top and cross-section view were plotted for MP1 in Fig. 5.1(c) and Fig. 5.1(d), while Fig. 5.1(e) and Fig. 5.1(f) depict the electromagnetic field distribution for MP3.

At the MP1 resonance, magnetic field is greatly enhanced by more than two orders of magnitude under the y-direction ridges only in the section between left and right cavities (i.e., discontinuous region along x direction), but is suppressed under the x-direction ridges (i.e., continuous region), as shown in Fig. 5.1(c). As further observed in Fig. 5.1(d), the magnetic field enhancement occurs inside the dielectric spacer only underneath top metallic ridges, accompany by an induced electric current loop. The electromagnetic field distribution shows the exact behavior of magnetic resonance or MP as previously studied in film-coupled 1D grating structures. The internal magnetic resonance is excited by the external electromagnetic waves at a particular frequency, and the coupling leads to the collective oscillation of charges, which forms a current loop and

induces a resonant magnetic field, resulting in strong energy absorption inside the structure.

Figures 5.1(e) and 5.1(f) show the electromagnetic field distribution at MP3 resonance, which is the third harmonic mode of MP featured with three antinodes in localized magnetic fields and three electric current loops with alternating directions. Similarly, the magnetic resonance with MP3 occurs only under y-direction ridges at the section between cavities, and is disabled under the continuous x-direction ridges. Note that the second harmonic mode MP2 is not observed here because the magnetic field strengths of two antinodes with opposite directions cancel each other due to the symmetry at normal incidence.

5.2 Design of a Film-Coupled Concave Grating Metamaterial Structure for Light Trapping

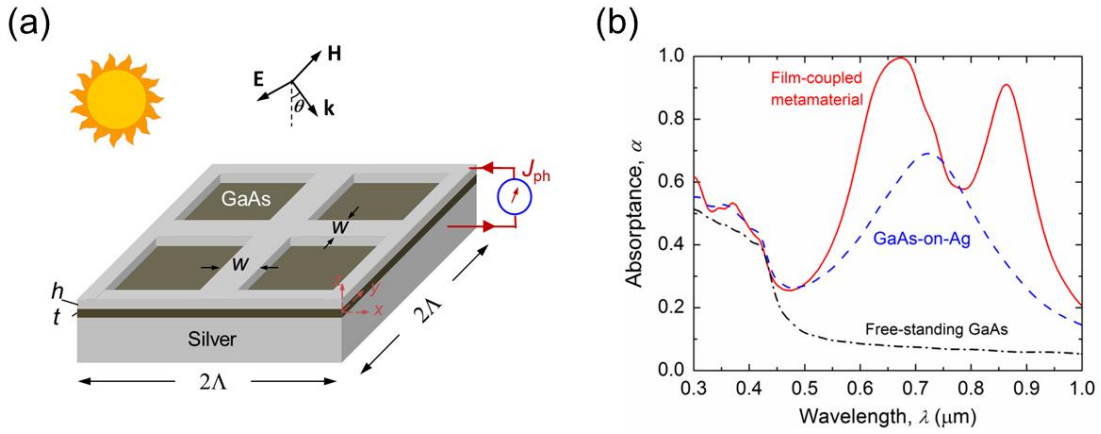

Figure 5.2 (a) Schematic for the light trapping structure; (b) Absorptance for the grating based light trapping structure, GaAs-Ag films, and free standing GaAs film.

By exciting plasmonic resonances inside the concave grating metamaterial structures, the light absorption and photovoltaic generation can be potentially enhanced. The schematic of the metamaterial light trapping structure is depicted in Fig. 5.2(a), a crystalline GaAs layer with thickness t = 30 nm is sandwiched by a concave grating and substrate both made of Ag. The grating period is Λ = 150 nm, while grating width and height are respectively w = 30 nm and h = 20 nm.

Figure 5.2(b) shows the normal absorptance at TM incidence with H field along y direction for the film-coupled metamaterial solar cell in comparison with a GaAs-on-Ag structure and a free-standing GaAs layer with the same thicknesses. For a free-standing 30-nm GaAs layer, the absorptance decreases dramatically at longer wavelengths beyond 400 nm due to the low intrinsic absorption coefficient of GaAs. Therefore, it is highly desired that the light absorption could be significantly enhanced in this spectral region from 400 nm up to the bandgap of GaAs around 870 nm in wavelength, which is crucial to improve the electricity generation. When an Ag back reflector was placed below the ultrathin GaAs layer, which is the GaAs-on-Ag structure, it is observed that there exists an absorption peak at λ = 0.72 μm with absorptance α = 0.69. This absorption peak is caused by the destructive interference between the incident and reflected waves inside the GaAs layer.

Now consider a subwavelength concave grating added onto the GaAs layer on Ag substrate, which is the proposed film-coupled light trapping structure. As shown in Fig. 5.2(b), the spectral absorptance exhibits two spectral peaks located at λ = 0.67 μm with unity absorptance and at λ = 0.86 μm with α = 0.9, respectively. Thanks to these two absorption peaks, the film-coupled light trapping structure exhibits much greater light

absorption compared with the free-standing GaAs film and the GaAs-on-Ag structure. Both absorption peaks are located above the bandgap of GaAs and thus could effectively enhance the light absorption for electron-hole pair generation. However, it is crucial to understand the physical mechanisms that are responsible for the enhanced light absorption in the film-coupled ultrathin solar cell structure.

The absorption peak at λ_{FP} = 0.67 μm is associated with the Fabry-Perot resonance in the Ag-GaAs-Ag cavity, which leads to near-unity absorptance. On the other hand, the long-wavelength resonance peak located at λ_{MP} = 0.86 μm is actually due to the excitation of MP, which has been studied in the concave grating structure in previous section.

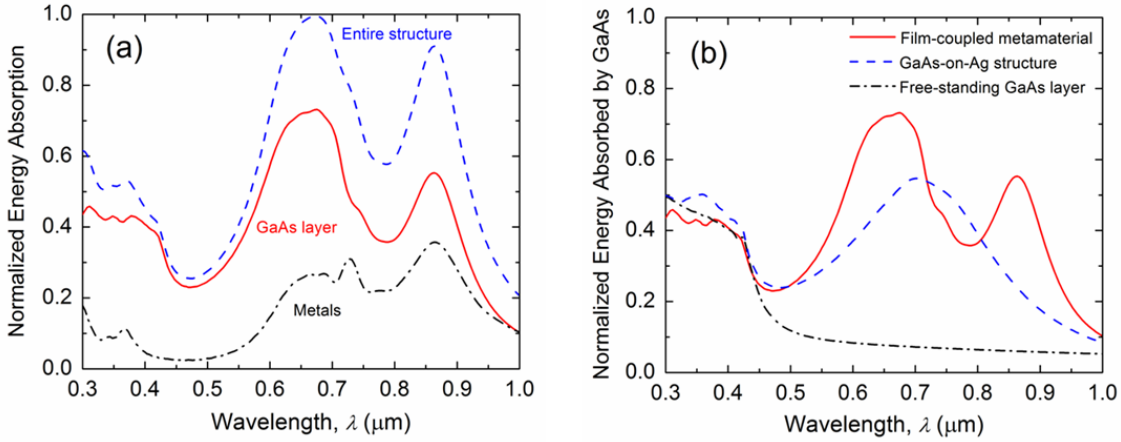

Figure 5.3 (a) Absorptance in each layer in the grating based light trapping structure; (b) Absorptance in the GaAs layer for the grating based light trapping structure, GaAs-Ag films, and free standing GaAs film.

Although light absorption can be significantly enhanced in the film-coupled concave grating structure by exciting MP and taking advantage of interference effect, only the amount of energy absorbed by the photovoltaic layer can contribute to the generation of electron-hole pairs. Energy absorbed by other materials like metals in the

structure is essentially loss. Therefore, it is crucial to evaluate the amount of energy absorbed by the active layer instead of the entire structure.

The absorbed energy normalized to incidence by the entire structure, GaAs, and metals is shown in Fig. 5.3(a) for the film-coupled light trapping structure. It can be observed that in the short-wavelength region from 0.3 μm to 0.45 μm, most of the energy are absorbed in the GaAs layer, while energy loss in Ag is negligible. Although the loss in Ag increases as wavelength increases, the energy absorbed by the GaAs could be as high as 70% at the absorption peak at λ_{FP} = 0.67 μm due to wave interference effect. The GaAs layer could still absorb as much as 55% of the incident light close to its bandgap, thanks to the excitation of MP at λ_{MP} = 0.86 μm, while another 34% is absorbed by the metals due to the ohmic loss when the induced electric current oscillates at the metal surfaces.

To have a better idea on the effectiveness of light trapping with the film-coupled metamaterial structure, Fig. 5.3(b) compares the energy absorbed by the GaAs layer in the light trapping metamaterial structure compared with that in the free-standing GaAs layer and the GaAs-on-Ag structure. Clearly, the film-coupled structure has superior performance in trapping light over the free-standing photovoltaic layer that only absorbs 5% of light in the long wavelengths, thanks to the effects of MP and wave interference excited above the bandgap. Although the GaAs-on-Ag structure could effectively trap light with the interference effect, it is not practical as a front contact is always required to harvest free charges but might deteriorate the optical performance. The proposed film-coupled metamaterial structure could not only effectively trap light to enhance the light absorption but also readily serve as electrical contacts for practical considerations.

In order to quantitatively evaluate performance for the film-coupled light trapping structure as an ultrathin solar cell, the short-circuit current density J_{sc} is calculated by:

$$J_{sc} = \frac{q}{hc_0} \int_{300nm}^{870nm} a_{GaAs}(\lambda) I(\lambda) \lambda d\lambda \tag{5.1}$$

where $I(\lambda)$ is the solar radiative heat flux at AM1.5 (global tilt), q is elementary charge, and h is Planck's constant. The calculated J_{sc} values are respectively 14.9 mA/cm^2, 12.5 mA/cm^2, and 3.8 mA/cm^2 for the film-coupled metamaterial solar cell, the GaAs-on-Ag structure, and the free-standing GaAs layer. Clearly, the short-circuit current is greatly enhanced by relatively almost three times with the film-coupled light trapping structure over the free-standing layer. Although it seems that the relative enhancement of 20% over the GaAs-on-Ag structure is not that significant, the film-coupled metamaterial structure is much more practical design as a solar cell. Note that, 100% internal quantum efficiency is assumed in the calculation of J_{sc}, because the charge transport mechanism in the ultrathin GaAs layer with sub-100 nm thickness, which is little understood and needs to be further studied, would be expected to be quite different from the bulk counterpart.

In practice, sample fabrication processes usually suffer from the manufacturing tolerance, which would unavoidably cause the variation of the geometric dimensions from the designed values. The slight geometric uncertainty from fabrication may influence the performance of the light trapping solar cell. Here, the effect of ridge width w on the performance of the proposed film-coupled light trapping structure is investigated. Figure 5.4 shows the total absorptance of the light trapping structure with ridge width w = 25 nm, 30 nm, and 35 nm (i.e., geometric tolerance of ±16.7%), while other geometric

parameters remain the same. It can be observed that the absorption peak associated with Fabry-Perot resonance is little affected by the ridge width, and the resonance wavelength remains to be around λ_{FP} = 0.67 μm. This is because the small change in grating ridge width will not affect the interference condition inside the Fabry-Perot cavity.

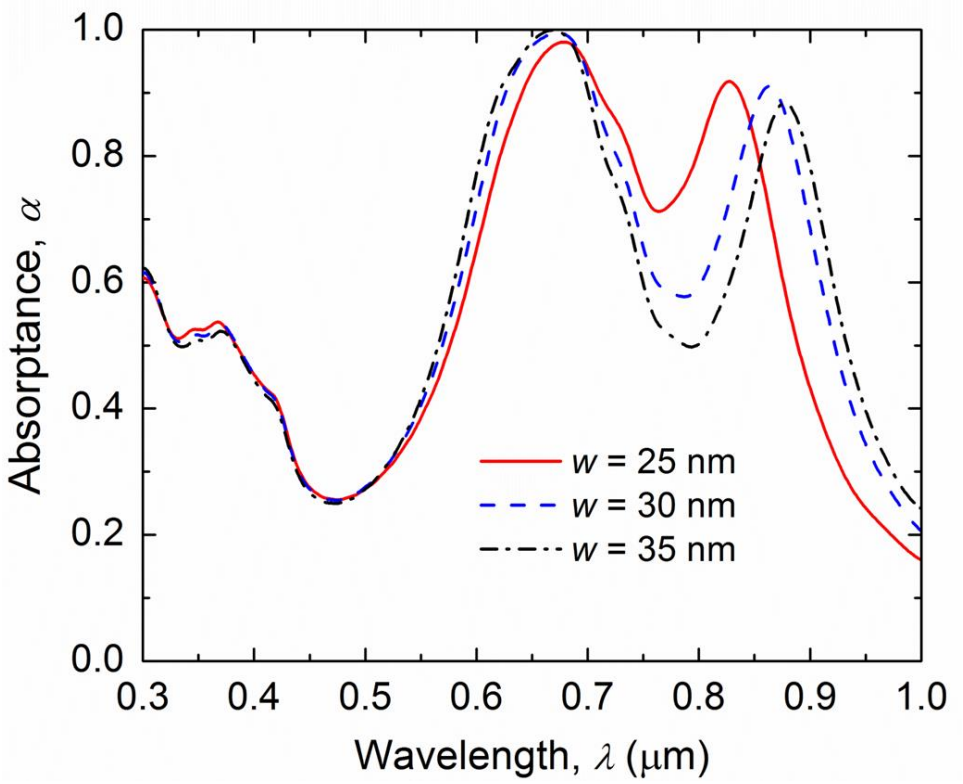

Figure 5.4 Effects of ridge width on the absorptance of the light trapping structure.

On the other hand, the other absorption peak due to magnetic resonance slightly shifts with varied ridge width, i.e., blue-shifting from λ_{MP} = 0.86 μm to 0.83 μm when the actual width is 5 nm less than the desired value of 30 nm, or red-shifting to 0.88 μm with a larger width w = 35 nm. The dependence of the magnetic resonance wavelength on the grating width has been discussed previously in a similar film-coupled concave grating structure but with lossless dielectric spacer made of SiO_2. rather than a semiconductor layer (GaAs) in the present study. Even though the magnetic resonance wavelength

slightly changes with the ridge width, it turns out that, the short-circuit current J_{sc} becomes 15.4 mA/cm^2 and 14.4 mA/cm^2 respectively with the ridge width of 25 nm and 35 nm, in comparison to the 14.9 mA/cm^2 with w = 30 nm. Therefore, a geometric tolerance of ±16.7% in the ridge width would only lead to a small relative error of ±3.4% in the short-circuit current of the proposed light trapping structure.

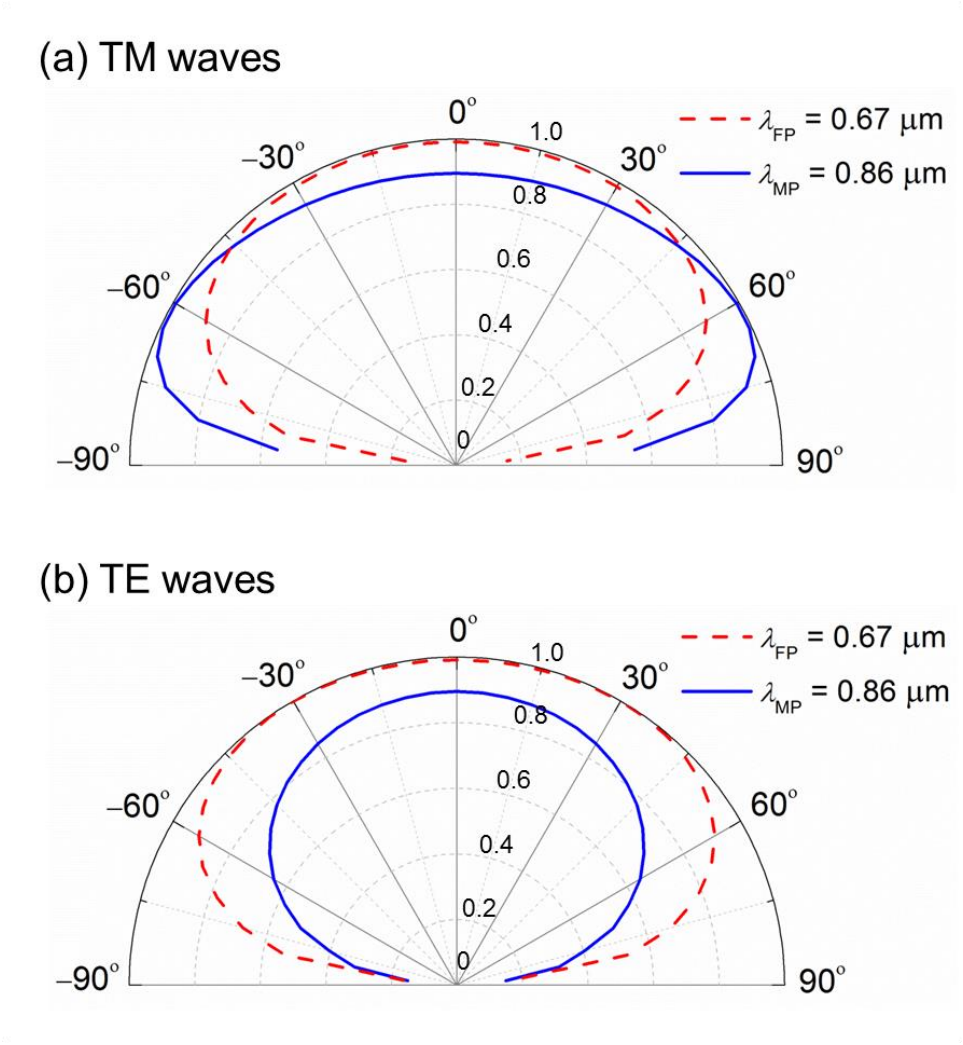

Figure 5.5 Effects of incidence angle on the absorptance of the light trapping structure for (a) TM waves and (b) TE waves.

Finally, the optical absorption at oblique incidence is explored in order to examine the directional-sensitivity for the film-coupled light trapping structure. Figure 5.5 plots the total absorptance with varied incidence angles from 0° to 85° with a resolution of 5° at two selected wavelengths λ_{FP} = 0.67 μm and λ_{MP} = 0.86 μm, at which Fabry-Perot and magnetic resonances occur. Note that TM and TE incidences are no longer identical at oblique incidences, so the behavior at oblique incidences is studied separately at each polarization. Figure 5.5(a) shows the absorptance with TM-polarized incidence, in which it can be observed that at λ_{FP} = 0.67 μm, the absorptance barely changes with incidence angles θ < 30°. When θ is further increased to 60°, the absorptance still remains as high as 0.9 or so. The unusual directional-insensitive absorption associated with Fabry-Perot cavity resonance is due to the lossy GaAs, which leads to a broad absorption peak in comparison with the sharp and direction-sensitive peaks with lossless dielectric cavies. On the other hand, at λ_{MP} = 0.86 μm, the absorption peak increases up to unity at the incidence angle of 65°. This is because the resonance strength for MP remains strong at TM oblique incidence, for which the incidence H field is always parallel to grating groove regardless of incidence angles.

Figure 5.5(b) illustrates the total absorptance as a function of incidence angle for TE-polarized waves. At λ_{FP} = 0.67 μm, the total absorptance has similar behavior as TM incidence, demonstrating highly insensitive behavior at oblique incidence angles. At λ_{MP} = 0.86 μm, the absorptance remains around 0.85 up to θ = 30° but drops to 0.65 at θ = 60°. Note that the MP resonance strength will decrease at oblique TE incidence, as the H field parallel to grating groove will decrease at large incidence angles with TE

polarization. The angle-resolved absorptance spectra at both polarizations clearly show the directional-insensitive behavior of the proposed light trapping structure, which is highly favorable for converting off-normal sunlight to electricity.

CHAPTER 6

CONCLUSION AND FUTURE WORK

6.1. Conclusion

This dissertation theoretically and experimentally investigates the engineering of metamaterials and metafilms for high efficiency solar energy conversion. Chapter 2 describes the instrumentation for optical and radiative properties characterization. The FTIR spectrometer is presented for specular reflectance measurement, along with a continuum microscope to perform spectroscopic measurements at smaller area down to 20 μm by 20 μm. A tunable light source coupled with an integrating sphere is introduced which can be employed for hemispherical and diffuse reflectance measurement. In terms of characterization of optical properties at high temperatures, an FTIR fiber optics setup is described for high temperature reflectance measurement, while a high temperature emissometry that measures the emittance directly is also discussed.

In this dissertation, the radiative properties of a metamaterial selective absorber made of two-dimensional tungsten gratings on a thin dielectric spacer and an opaque tungsten film are investigated from UV to mid-infrared region. This absorber exhibits absorptance >95% in a broader solar spectrum with double-sized patch arrays on the top, while its IR emittance is less than 4%. Moreover, the metamaterial solar absorber is proved to exhibit quasi-diffuse behaviors as well as polarization independence. On the other hand, the metamaterial selective solar absorber made of nanostructured titanium gratings deposited on an ultrathin MgF_2 spacer and a tungsten ground film is proposed

and experimentally demonstrated. Normal absorptance of the fabricated solar absorber is characterized to be higher than 90% in the UV, visible and, near infrared (IR) regime, while the mid-IR emittance is around 20%. Temperature-dependent spectroscopic characterization indicates that the optical properties barely change at elevated temperatures up to 350°C. The solar-to-heat conversion efficiency with the fabricated metamaterial solar absorber is predicted to be 78% at 100°C without optical concentration or 80% at 400°C with 25 suns. The strong spectral selectivity, favorable diffuse-like behavior, and excellent thermal stability make the metamaterial selective absorber promising for significantly enhancing solar thermal energy harvesting in various systems at mid to high temperatures.

Besides the metamaterial selective absorber, a multilayer selective solar absorber with SiO_2-Si_3N_4-W-SiO_2-W configuration is theoretically designed, experimentally fabricated and optically characterized. FTIR measurements indicate excellent spectral selectivity for this multilayer absorber with absorptance larger than 95% in the visible and near IR, as well as emittance less than 10% in the IR spectral regime. Oblique reflectance is also characterized by the FTIR for both TE and TM polarizations, demonstrating its insensitive performance to incidence angles. On the other hand, the high temperature stability is investigated by the temperature dependent reflectance measurement with the FTIR fiber optics, proving its excellent thermal stability up to 600°C in ambient. In addition, the diffuse reflectance is measured in the integrating sphere coupled with a tunable light source, indicating the highly specular optical behavior of this multilayer absorber both before and after being heated at 600°C. In order to investigate the cause for the thermal instability at temperature above 600°C, the sample

heated at 700^{o}C is characterized by both the SEM and RBS techniques, revealing the surface blistering as the reason for the change of optical properties at higher temperatures. The surface blistering is possibly due to the CTE mismatch or outgassing from the structure, which could be further avoided by better material selection and fabrication procedure.

Moreover, an STPV system employing film-coupled metamaterial as the solar absorber and TPV emitter is theoretically discussed, whose conversion efficiency ranges from 8% to 10% with concentration factor varying between 20 and 200. Due to the spectral selectivity of metamaterials, the conversion efficiency of the STPV system with metamaterial absorber/emitter is remarkably enhanced when compared with the efficiency of the STPV system with black absorber and emitter (< 2.5%). Furthermore, the effects of sidewall emission loss and non-ideal view factor between the TPV emitter and cell are also investigated, and the diminished performance of the STPV system due to these two non-ideal factors is quantitatively discussed. Moreover, the STPV system with emitter-absorber area ratio larger than 1 is also studied, and it is demonstrated that the total conversion efficiency can be further enhanced with larger emitter-absorber area ratios. It is found that the STPV system with an emitter-absorber area ratio of 4 can further reach to a total conversion efficiency of 12.6% under 200 suns.

The experimental work for TPV system is further discussed in this dissertation. A multilayer TPV emitter is experimentally fabricated and characterized, demonstrating its spectral selectivity. The future work will include the system testing and efficiency characterization for the TPV system.

Furthermore, we have numerically demonstrated that thermal radiative properties can be tailored with film-coupled concave grating metamaterials by excitation of multiple MP and SPP resonance modes, which result in selective absorption at the visible and near-infrared frequencies.

One step further, we have numerically demonstrated the plasmonic light trapping inside an ultrathin photovoltaic layer in this concave grating film-coupled metamaterial structure, which could not only readily serve as electrical contacts for charge harvesting but also effectively trap light with the help of interference and magnetic resonance effects above the bandgap, potentially leading to improved solar-to-electricity conversion efficiency. The short-circuit current density with the film-coupled metamaterial solar cell is enhanced by three times of that from a free-standing GaAs layer. The small variation on the grating ridge width due to fabrication tolerance has little effect on the performance of the proposed light trapping solar cell structure, whose optical absorption is also shown to be insensitive with the oblique incidences. The fundamental understanding gained in this work will facilitate the development of next-generation, ultrathin, low-cost, highly-efficient solar cells.

6.2 Future Work.

For the solar thermal selective absorber, the future work will focus on two directions: 1. To further increase the thermal stability; 2. To reduce the cost and make the fabrication process more efficient. As indicated by Fig. 3.22, the surface blistering will be a main reason for the instability of the metafilm absorber at high temperatures. In order to avoid this phenomenon, substrates with better CTE match to tungsten could be selected to

reduce the thermal stress. On the other hand, to reduce the cost and facilitate large-area fabrication, other structures such as film-coupled nanoparticle structures could also be considered. In terms of the STPV and TPV projects, the experimental work of the TPV system is still ongoing, and the system efficiency and generated electric power will be characterized. For the light trapping structures, the light trapping in organic or perovskite solar cells will be further looked into. This is because reducing the PV layer thickness for organic and perovskite solar cells will be more critical as their charge recombination is much stronger compared with crystalline solar cells.

The publications during my PhD research are listed below:

[1]. H. Wang, H. Su, L.P. Wang, Large-area Lithography-free Omnidirectional metafilm selective solar coatings with excellent high-temperature stability, *Advanced Materials*, to be submitted (2016).

[2]. H. Alshehri, X.Y. Ying, H. Wang, L.P. Wang, Plasmonic local heating beyond diffraction limit by the excitation of magnetic polariton, *Journal of Applied Physics*, to be submitted (2016).

[3]. J.-Y. Chang, H. Wang, L.P. Wang, Tungsten nanowire metamaterials as selective solar thermal absorbers by exciting magnetic polariton, *ASME Journal of Heat Transfer*, submitted (2016).

[4]. H. Wang, J.-Y. Chang, Y. Yang, L.P. Wang, Performance Analysis of Solar Thermophotovoltaic conversion enhanced by selective metamaterial absorbers and emitters, *International Journal of Heat and Mass Transfer*, accepted (2016).

[5]. H. Wang, V.P. Sivan, A. Mitchell, G. Rosengarten, P. Phelan, L.P. Wang, Highly efficient selective metamaterial absorber for high-temperature solar thermal energy harvesting, *Solar Energy Materials and Solar Cells*, 137 (2015) 235-242.

[6]. H. Wang,# Y. Yang,# L.P Wang, Infrared frequency-tunable coherent thermal sources, *Journal of Optics*, 17 (2015) 045104. (# Equal Contribution)

[7]. H. Wang, L.P. Wang, Plasmonic light Trapping in an ultrathin photovoltaic layer with film-coupled metamaterial structures, *AIP Advances*, 4 (2015) 0527104.

[8]. H. Wang, L.P. Wang, Tailoring thermal radiative properties with film-coupled concave grating metamaterials, *Journal of Quantitative Spectroscopy and Radiative Transfer*, 158 (2015) 127-135.

[9]. H. Wang, K. O'Dea, L.P. Wang, Selective absorption of visible light in film-coupled nanoparticles by exciting magnetic resonance, *Optics Letters*, 39 (2014) 1457-1460.

[10]. H. Wang, Y. Yang, L.P. Wang, Wavelength-tunable infrared metamaterial by exciting magnetic polariton with phase transition VO_2, *Journal of Applied Physics*, 116 (2014) 123503.

[11]. H. Wang, Y. Yang, L.P. Wang, Switchable Wavelength-selective and diffuse metamaterial absorber/emitter with a phase transition spacer layer, *Applied Physics Letters*, 105 (2014) 071907.

[12]. H. Wang, L.P. Wang, Perfect selective metamaterial solar thermal absorbers, *Optics Express*, 21 (2013) A1078-A1093.

REFERENCES

[1] I.E. Khodasevych, L. P. Wang, A. Mitchell, G. Rosengarten, Micro-and nanostructured surfaces for selective solar absorption, *Advanced Optical Materials*, (2015).

[2] R. Pettit, R. Sowell, I. Hall, Black chrome solar selective coatings optimized for high temperature applications, *Solar Energy Materials*, 7 (1982) 153-170.

[3] G.E. McDonald, Spectral reflectance properties of black chrome for use as a solar selective coating, *Solar Energy*, 17 (1975) 119-122.

[4] J. Sweet, R. Pettit, M. Chamberlain, Optical modeling and aging characteristics of thermally stable black chrome solar selective coatings, *Solar Energy Materials*, 10 (1984) 251-286.

[5] C.K. Ho, A.R. Mahoney, A. Ambrosini, M. Bencomo, A. Hall, T.N. Lambert, Characterization of Pyromark 2500 paint for high-temperature solar receivers, *Journal of Solar Energy Engineering*, 136 (2014) 014502.

[6] D. Ding, W. Cai, Self-assembled nanostructured composites for solar absorber, *Materials Letters*, 93 (2013) 269-271.

[7] L. Gaouyat, Z. He, J.-F. Colomer, P. Lambin, F. Mirabella, D. Schryvers, O. Deparis, Revealing the innermost nanostructure of sputtered $NiCrO_x$ solar absorber cermets, *Solar Energy Materials and Solar Cells*, 122 (2014) 303-308.

[8] E. Wäckelgård, A. Mattsson, R. Bartali, R. Gerosa, G. Gottardi, F. Gustavsson, N. Laidani, V. Micheli, D. Primetzhofer, B. Rivolta, Development of W–SiO_2 and Nb–TiO_2 solar absorber coatings for combined heat and power systems at intermediate operation temperatures, *Solar Energy Materials and Solar Cells*, 133 (2015) 180-193.

[9] J. Cheng, C. Wang, W. Wang, X. Du, Y. Liu, Y. Xue, T. Wang, B. Chen, Improvement of thermal stability in the solar selective absorbing Mo–Al_2O_3 coating, *Solar Energy Materials and Solar Cells*, 109 (2013) 204-208.

[10] Q.-C. Zhang, Stainless-steel–AlN cermet selective surfaces deposited by direct current magnetron sputtering technology, *Solar Energy Materials and Solar Cells*, 52 (1998) 95-106.

[11] Y. Liu, X. Zhang, Metamaterials: a new frontier of science and technology, *Chemical Society Reviews*, 40 (2011) 2494-2507.

[12] H. Wang, L.P. Wang, Perfect selective metamaterial solar absorbers, *Optics Express*, 21 (2013) A1078-A1093.

[13] L.P. Wang, Z.M. Zhang, Wavelength-selective and diffuse emitter enhanced by magnetic polaritons for thermophotovoltaics, *Applied Physics Letters*, 100 (2012) 063902.

[14] H. Wang, V.P. Sivan, A. Mitchell, G. Rosengarten, P. Phelan, L.P. Wang, Highly efficient selective metamaterial absorber for high-temperature solar thermal energy harvesting, *Solar Energy Materials and Solar Cells*, 137 (2015) 235-242.

[15] B.J. Lee, Y.-B. Chen, S. Han, F.-C. Chiu, H.J. Lee, Wavelength-selective solar thermal absorber with two-dimensional nickel gratings, *Journal of Heat Transfer*, 136 (2014) 072702.

[16] J. Dai, F. Ye, Y. Chen, M. Muhammed, M. Qiu, M. Yan, Light absorber based on nano-spheres on a substrate reflector, *Optics Express*, 21 (2013) 6697-6706.

[17] M. Yan, J. Dai, M. Qiu, Lithography-free broadband visible light absorber based on a mono-layer of gold nanoparticles, *Journal of Optics*, 16 (2014) 025002.

[18] H. Wang, K. O'Dea, L.P. Wang, Selective absorption of visible light in film-coupled nanoparticles by exciting magnetic resonance, *Optics Letters*, 39 (2014) 1457-1460.

[19] V. Stelmakh, V. Rinnerbauer, R. Geil, P. Aimone, J. Senkevich, J. Joannopoulos, M. Soljačić, I. Celanovic, High-temperature tantalum tungsten alloy photonic crystals: Stability, optical properties, and fabrication, *Applied Physics Letters*, 103 (2013) 123903.

[20] I. Celanovic, N. Jovanovic, J. Kassakian, Two-dimensional tungsten photonic crystals as selective thermal emitters, *Applied Physics Letters*, 92 (2008) 193101.

[21] V. Rinnerbauer, S. Ndao, Y.X. Yeng, J.J. Senkevich, K.F. Jensen, J.D. Joannopoulos, M. Soljačić, I. Celanovic, R.D. Geil, Large-area fabrication of high aspect ratio tantalum photonic crystals for high-temperature selective emitters, *Journal of Vacuum Science & Technology B*, 31 (2013) 011802.

[22] M.G. Nielsen, A. Pors, O. Albrektsen, S.I. Bozhevolnyi, Efficient absorption of visible radiation by gap plasmon resonators, Optics Express, 20 (2012) 13311-13319.

[23] K. Chen, R. Adato, H. Altug, Dual-band perfect absorber for multispectral plasmon-enhanced infrared spectroscopy, *Acs Nano*, 6 (2012) 7998-8006.

[24] N. Landy, S. Sajuyigbe, J. Mock, D. Smith, W. Padilla, Perfect metamaterial absorber, *Physical Review Letters*, 100 (2008) 207402.

[25] H. Tao, C. Bingham, A. Strikwerda, D. Pilon, D. Shrekenhamer, N. Landy, K. Fan, X. Zhang, W. Padilla, R. Averitt, Highly flexible wide angle of incidence terahertz metamaterial absorber: Design, fabrication, and characterization, *Physical Review B*, 78 (2008) 241103.

[26] B. Wang, T. Koschny, C.M. Soukoulis, Wide-angle and polarization-independent chiral metamaterial absorber, *Physical Review B*, 80 (2009) 033108.

[27] D.Y. Shchegolkov, A. Azad, J. O'Hara, E. Simakov, Perfect subwavelength fishnetlike metamaterial-based film terahertz absorbers, *Physical Review B*, 82 (2010) 205117.

[28] Y.Q. Ye, Y. Jin, S. He, Omnidirectional, polarization-insensitive and broadband thin absorber in the terahertz regime, *JOSA B*, 27 (2010) 498-504.

[29] X. Liu, T. Starr, A.F. Starr, W.J. Padilla, Infrared spatial and frequency selective metamaterial with near-unity absorbance, *Physical Review Letters*, 104 (2010) 207403.

[30] J. Hao, J. Wang, X. Liu, W.J. Padilla, L. Zhou, M. Qiu, High performance optical absorber based on a plasmonic metamaterial, *Applied Physics Letters*, 96 (2010) 251104.

[31] K. Aydin, V.E. Ferry, R.M. Briggs, H.A. Atwater, Broadband polarization-independent resonant light absorption using ultrathin plasmonic super absorbers, *Nature Communications*, 2 (2011) 517.

[32] A. Moreau, C. Ciracì, J.J. Mock, R.T. Hill, Q. Wang, B.J. Wiley, A. Chilkoti, D.R. Smith, Controlled-reflectance surfaces with film-coupled colloidal nanoantennas, *Nature*, 492 (2012) 86-89.

[33] M.K. Hedayati, M. Javaherirahim, B. Mozooni, R. Abdelaziz, A. Tavassolizadeh, V.S.K. Chakravadhanula, V. Zaporojtchenko, T. Strunkus, F. Faupel, M. Elbahri, Design of a perfect black absorber at visible frequencies using plasmonic metamaterials, *Advanced Materials*, 23 (2011) 5410-5414.

[34] C. Hägglund, G. Zeltzer, R. Ruiz, I. Thomann, H.-B.-R. Lee, M.L. Brongersma, S.F. Bent, Self-assembly based plasmonic arrays tuned by atomic layer deposition for extreme visible light absorption, *Nano Letters*, 13 (2013) 3352-3357.

[35] Z.M. Zhang, Nano/microscale heat transfer, McGraw-Hill New York, 2007.

[36] X. Liu, T. Tyler, T. Starr, A.F. Starr, N.M. Jokerst, W.J. Padilla, Taming the blackbody with infrared metamaterials as selective thermal emitters, *Physical Review Letters*, 107 (2011) 045901.

[37] I. Puscasu, W.L. Schaich, Narrow-band, tunable infrared emission from arrays of microstrip patches, *Applied Physics Letters*, 92 (2008) 233102.

[38] B. Lee, L. Wang, Z. Zhang, Coherent thermal emission by excitation of magnetic polaritons between periodic strips and a metallic film, *Optics Express*, 16 (2008) 11328-11336.

[39] B. Zhao, L. Wang, Y. Shuai, Z.M. Zhang, Thermophotovoltaic emitters based on a two-dimensional grating/thin-film nanostructure, *International Journal of Heat and Mass Transfer*, 67 (2013) 637-645.

[40] C. Wu, I. Burton Neuner, G. Shvets, J. John, A. Milder, B. Zollars, S. Savoy, Large-area wide-angle spectrally selective plasmonic absorber, *Physical Review B*, 84 (2011) 075102.

[41] J. Wang, Y. Chen, J. Hao, M. Yan, M. Qiu, Shape-dependent absorption characteristics of three-layered metamaterial absorbers at near-infrared, *Journal of Applied Physics*, 109 (2011) 074510.

[42] Y. Cui, J. Xu, K.H. Fung, Y. Jin, A. Kumar, S. He, N.X. Fang, A thin film broadband absorber based on multi-sized nanoantennas, *Applied Physics Letters*, 99 (2011) 253101.

[43] C. Wu, G. Shvets, Design of metamaterial surfaces with broadband absorbance, *Optics Letters*, 37 (2012) 308-310.

[44] C.-W. Cheng, M.N. Abbas, C.-W. Chiu, K.-T. Lai, M.-H. Shih, Y.-C. Chang, Wide-angle polarization independent infrared broadband absorbers based on metallic multi-sized disk arrays, *Optics Express*, 20 (2012) 10376-10381.

[45] P. Bouchon, C. Koechlin, F. Pardo, R. Haïdar, J.-L. Pelouard, Wideband omnidirectional infrared absorber with a patchwork of plasmonic nanoantennas, *Optics Letters*, 37 (2012) 1038-1040.

[46] H. Cheng, S. Chen, H. Yang, J. Li, X. An, C. Gu, J. Tian, A polarization insensitive and wide-angle dual-band nearly perfect absorber in the infrared regime, *Journal of Optics*, 14 (2012) 085102.

[47] N. Zhang, P. Zhou, D. Cheng, X. Weng, J. Xie, L. Deng, Dual-band absorption of mid-infrared metamaterial absorber based on distinct dielectric spacing layers, *Optics Letters*, 38 (2013) 1125-1127.

[48] G. Dayal, S.A. Ramakrishna, Design of multi-band metamaterial perfect absorbers with stacked metal–dielectric disks, *Journal of Optics*, 15 (2013) 055106.

[49] Y. Cui, K.H. Fung, J. Xu, H. Ma, Y. Jin, S. He, N.X. Fang, Ultrabroadband light absorption by a sawtooth anisotropic metamaterial slab, *Nano Letters*, 12 (2012) 1443-1447.

[50] M. Langlais, H. Bru, P. Ben-Abdallah, High temperature layered absorber for thermo-solar systems, *Journal of Quantitative Spectroscopy and Radiative Transfer*, 149 (2014) 8-15.

[51] Z. Nuru, M. Msimanga, C. Arendse, M. Maaza, Heavy ion elastic recoil detection analysis of $Al_xO_y/Pt/Al_xO_y$ multilayer selective solar absorber, *Applied Surface Science*, 298 (2014) 176-181.

[52] W. Shockley, H.J. Queisser, Detailed balance limit of efficiency of p-n junction solar cells, *Journal of Applied Physics*, 32 (1961) 510-519.

[53] S. Fan, An alternative 'Sun'for solar cells, (2014).

[54] N.-P. Harder, P. Würfel, Theoretical limits of thermophotovoltaic solar energy conversion, *Semiconductor Science and Technology*, 18 (2003) S151.

[55] Y. Nam, Y.X. Yeng, A. Lenert, P. Bermel, I. Celanovic, M. Soljačić, E.N. Wang, Solar thermophotovoltaic energy conversion systems with two-dimensional tantalum photonic crystal absorbers and emitters, *Solar Energy Materials and Solar Cells*, 122 (2014) 287-296.

[56] A. Lenert, D.M. Bierman, Y. Nam, W.R. Chan, I. Celanović, M. Soljačić, E.N. Wang, A nanophotonic solar thermophotovoltaic device, *Nature Nanotechnology*, 9 (2014) 126-130.

[57] A. Lenert, V. Rinnerbauer, D.M. Bierman, Y. Nam, I. Celanovic, M. Soljacic, E.N. Wang, 2D Photonic-crystals for high spectral conversion efficiency in solar thermophotovoltaics, in: Micro Electro Mechanical Systems (MEMS), *2014 IEEE 27th International Conference* on, *IEEE*, (2014) 576-579.

[58] V. Rinnerbauer, Y. Yeng, J. Senkevich, J. Joannopoulos, M. Soljačić, I. Celanovic, Large area selective emitters/absorbers based on 2D tantalum photonic crystals for high-temperature energy applications, in: *SPIE OPTO, International Society for Optics and Photonics*, (2013) 863207.

[59] V. Stelmakh, V. Rinnerbauer, W.R. Chan, J.J. Senkevich, J.D. Joannopoulos, M. Soljačić, I. Celanovic, Performance of tantalum-tungsten alloy selective emitters in thermophotovoltaic systems, in: *SPIE Sensing Technology+ Applications, International Society for Optics and Photonics*, (2014) 911504.

[60] Y.X. Yeng, W.R. Chan, V. Rinnerbauer, J.D. Joannopoulos, M. Soljačić, I. Celanovic, Performance analysis of experimentally viable photonic crystal enhanced thermophotovoltaic systems, *Optics Express*, 21 (2013) A1035-A1051.

[61] S.G. Babiker, Y. Shuai, M.O. Sid-Ahmed, M. Xie, One-dimensional multilayer microstructure emitter for thermophotovoltaic applications, *International Journal of Energy, Information & Communications*, 5 (2014).

[62] L. Wang, S. Basu, Z. Zhang, Direct measurement of thermal emission from a Fabry–Perot Cavity resonator, *Journal of Heat Transfer*, 134 (2012) 072701.

[63] M. Langlais, P. Prod, H. Bru, P. Ben-Abdallah, High temperature layered absorber for thermo-solar systems, *Journal of Quantitative Spectroscopy and Radiative Transfer*, 149 (2014) 8-15.

[64] P. Hu, Y. Liu, Q. Zhang, Z. Chen, Thermodynamic analysis on medium-high temperature solar thermal systems with selective coatings, *Science China Technological Sciences*, 56 (2013) 3137-3143.

[65] H. Deng, T. Wang, J. Gao, X. Yang, Metamaterial thermal emitters based on nanowire cavities for high-efficiency thermophotovoltaics, *Journal of Optics*, 16 (2014) 035102.

[66] S. Wu, X. Li, Y. Zhan, K. Li, Absorption enhancement of single silicon nanowire by tailoring rear metallic film for photovoltaic applications, *Optics Letters*, 39 (2014) 817-820.

[67] Y. He, H. Deng, X. Jiao, S. He, J. Gao, X. Yang, Infrared perfect absorber based on nanowire metamaterial cavities, *Optics Letters*, 38 (2013) 1179-1181.

[68] H. Wang, L. Wang, Tailoring thermal radiative properties with film-coupled concave grating metamaterials, *Journal of Quantitative Spectroscopy and Radiative Transfer*, (2014).

[69] W. Gu, G. Tang, W. Tao, High efficiency thermophotovoltaic emitter by metamaterial-based nano-pyramid array, *Optics Express*, 23 (2015) 30681-30694.

[70] N. Liu, M. Mesch, T. Weiss, M. Hentschel, H. Giessen, Infrared perfect absorber and its application as plasmonic sensor, *Nano Letters*, 10 (2010) 2342-2348.

[71] J. Wang, C. Fan, P. Ding, J. He, Y. Cheng, W. Hu, G. Cai, E. Liang, Q. Xue, Tunable broad-band perfect absorber by exciting of multiple plasmon resonances at optical frequency, *Optics Express*, 20 (2012) 14871-14878.

[72] T.W. Ebbesen, H. Lezec, H. Ghaemi, T. Thio, P. Wolff, Extraordinary optical transmission through sub-wavelength hole arrays, *Nature*, 391 (1998) 667-669.

[73] S. Wedge, I.R. Hooper, I. Sage, W.L. Barnes, Light emission through a corrugated metal film: The role of cross-coupled surfaceplasmon polaritons, *Physical Review B*, 69 (2004) 245418.

[74] L. Wang, Z.M. Zhang, Effect of magnetic polaritons on the radiative properties of double-layer nanoslit arrays, *JOSA B*, 27 (2010) 2595-2604.

[75] S.A. Maier, Plasmonics: fundamentals and applications, Springer Science & Business Media, 2007.

[76] P. Campbell, M.A. Green, Light trapping properties of pyramidally textured surfaces, *Journal of Applied Physics*, 62 (1987) 243-249.

[77] Y.-J. Lee, D.S. Ruby, D.W. Peters, B.B. McKenzie, J.W. Hsu, ZnO nanostructures as efficient antireflection layers in solar cells, *Nano Letters*, 8 (2008) 1501-1505.

[78] S. Fahr, T. Kirchartz, C. Rockstuhl, F. Lederer, Approaching the Lambertian limit in randomly textured thin-film solar cells, *Optics Express*, 19 (2011) A865-A874.

[79] L. Zeng, Y. Yi, C. Hong, J. Liu, N. Feng, X. Duan, L. Kimerling, B. Alamariu, Efficiency enhancement in Si solar cells by textured photonic crystal back reflector, *Applied Physics Letters*, 89 (2006) 111111.

[80] Z. Yu, A. Raman, S. Fan, Fundamental limit of nanophotonic light trapping in solar cells, *Proceedings of the National Academy of Sciences*, 107 (2010) 17491-17496.

[81] D.M. Callahan, J.N. Munday, H.A. Atwater, Solar cell light trapping beyond the ray optic limit, *Nano Letters*, 12 (2012) 214-218.

[82] J.N. Munday, D.M. Callahan, H.A. Atwater, Light trapping beyond the $4n_2$ limit in thin waveguides, *Applied Physics Letters*, 100 (2012) 121121.

[83] W. Wang, S. Wu, K. Reinhardt, Y. Lu, S. Chen, Broadband light absorption enhancement in thin-film silicon solar cells, *Nano Letters*, 10 (2010) 2012-2018.

[84] R.A. Pala, J. White, E. Barnard, J. Liu, M.L. Brongersma, Design of plasmonic thin-film solar cells with broadband absorption enhancements, *Advanced Materials*, 21 (2009) 3504-3509.

[85] I. Massiot, C. Colin, C. Sauvan, P. Lalanne, P.R.I. Cabarrocas, J.-L. Pelouard, S. Collin, Multi-resonant absorption in ultra-thin silicon solar cells with metallic nanowires, *Optics Express*, 21 (2013).

[86] K. Liu, H. Hu, H. Song, X. Zeng, D. Ji, S. Jiang, Q. Gan, Wide-Angle and Polarization-Insensitive Perfect Absorber for Organic Photovoltaic Layers, *IEEE Photonics Technology Letters*, 25 (2013).

[87] L.-H. Zhu, M.-R. Shao, R.-W. Peng, R.-H. Fan, X.-R. Huang, M. Wang, Broadband absorption and efficiency enhancement of an ultra-thin silicon solar cell with a plasmonic fractal, *Optics Express*, 21 (2013) A313-A323.

[88] S.Y. Chou, W. Ding, Ultrathin, high-efficiency, broad-band, omni-acceptance, organic solar cells enhanced by plasmonic cavity with subwavelength hole array, *Optics Express*, 21 (2013) A60-A76.

[89] X. Chen, B. Jia, J.K. Saha, B. Cai, N. Stokes, Q. Qiao, Y. Wang, Z. Shi, M. Gu, Broadband enhancement in thin-film amorphous silicon solar cells enabled by nucleated silver nanoparticles, *Nano Letters*, 12 (2012) 2187-2192.

[90] C.-H. Poh, L. Rosa, S. Juodkazis, P. Dastoor, FDTD modeling to enhance the performance of an organic solar cell embedded with gold nanoparticles, *Optical Materials Express*, 1 (2011) 1326-1331.

[91] D. Derkacs, W. Chen, P. Matheu, S. Lim, P. Yu, E. Yu, Nanoparticle-induced light scattering for improved performance of quantum-well solar cells, *Applied Physics Letters*, 93 (2008) 091107.

[92] Y. Zhang, N. Stokes, B. Jia, S. Fan, M. Gu, Towards ultra-thin plasmonic silicon wafer solar cells with minimized efficiency loss, *Scientific Reports*, 4 (2014).
[93] L. Lu, Z. Luo, T. Xu, L. Yu, Cooperative plasmonic effect of Ag and Au nanoparticles on enhancing performance of polymer solar cells, *Nano Letters*, 13 (2012) 59-64.

[94] H. Gao, X. Zhang, Z. Yin, H. Tan, S. Zhang, J. Meng, X. Liu, Plasmon enhanced polymer solar cells by spin-coating Au nanoparticles on indium-tin-oxide substrate, *Applied Physics Letters*, 101 (2012) 133903.

[95] F. Wooten, Optical properties of solids, Academic press, 2013.

[96] Air Mass 1.5 Spectra, American Society for Testing and Materials (ASTM), Available from: http://rredc.nrel.gov/solar/spectra/am1.5/.

[97] E.D. Palik, Handbook of optical constants of solids, Academic press, 1998.

[98] J. Robinson, Y. Rahmat-Samii, Particle swarm optimization in electromagnetics, *Antennas and Propagation, IEEE Transactions* on, 52 (2004) 397-407.

[99] N. Jin, Y. Rahmat-Samii, Advances in particle swarm optimization for antenna designs: Real-number, binary, single-objective and multiobjective implementations, *Antennas and Propagation, IEEE Transactions* on, 55 (2007) 556-567.

[100] H. Wang, L. Wang, High-temperature selective solar thermal absorber based on Fabry-Perot resonance cavity, in: *SPIE Optics+ Photonics for Sustainable Energy, International Society for Optics and Photonics*, (2015) 955907.

[101] S. Vassant, J.-P. Hugonin, F. Marquier, J.-J. Greffet, Berreman mode and epsilon near zero mode, *Optics Express*, 20 (2012) 23971-23977.

[102] Y.-B. Chen, F.-C. Chiu, Trapping mid-infrared rays in a lossy film with the Berreman mode, epsilon near zero mode, and magnetic polaritons, *Optics Express*, 21 (2013) 20771-20785.

[103] M.F. Modest, Radiative heat transfer, Academic press, 2013.

[104] W. Chan, R. Huang, C. Wang, J. Kassakian, J. Joannopoulos, I. Celanovic, Modeling low-bandgap thermophotovoltaic diodes for high-efficiency portable power generators, *Solar Energy Materials and Solar Cells*, 94 (2010) 509-514.